OPTIMIZATION OF SEPTA SHADOWING IN PET SCANNERS WITH RETRACTABLE SEPTA USING MONTE CARLO TECHNIQUES

by:

Nekmohamed Manji, B.Eng.

A Thesis

Submitted to the School of Graduate studies

in Partial Fulfillment of the Requirements

for the Degree

Master of Science

McMaster University

MASTER OF SCIENCE (1995) McMaster University
(Physics) Hamilton, Ontario

TITLE: Optimization of Septa Shadowing in PET Scanners With Retractable Septa Using Monte Carlo Techniques

AUTHOR: Nekmohamed Manji, B.Eng. (McMaster University)

SUPERVISOR: Dr. C. Nahmias

NUMBER OF PAGES: ix, 130

ABSTRACT

Scatter and random coincidences are of significant concern in Positron Tomography because they lead to the misrepresentation of the activity distribution in the final image. In this regard, interplane septa have long been used in ring positron tomographs to supress the acquisition of photons oblique to the scan planes. The septa extend from the face of the detector array to the edge of the field of view. Not only do the septa block photons scattered oblique to the scan planes and singles originating in different planes, but they also result in a decreased count rate sensitivity of the tomograph to true coincidence photons.

In this work, the Monte Carlo technique has been employed to study the effect of "septa shadowing" with respect to septa length in order to determine an optimal septa length. Sensitivity parameters have been derived by the use of Noise Equivalent Count (NEC) Rate Analysis, as well as count rate sensitivity analysis in order to balance the counting and imaging performance of the system. In addition, energy spectra, sinogram profiles and scatter fraction results are presented to quantify the effects of septa length on the trues, scatter and randoms contributions of the data collected by the scanner.

It is concluded that the highest NEC rate is achieved with positron tomographs with no septa and operating in 3D mode.

ACKNOWLEDGMENTS

First and foremost, I would like to express my appreciation to my supervisor, Dr. Claude Nahmias for his support and encouragement during the duration of this work. In particular, his patience and insight has been deeply appreciated. In addition, as a scientist, supervisor and researcher, Dr. Nahmias has set an excellent example to follow.

I would also like to thank my family and in particular, my parents, for all their support and guidance over the years. They have always insisted that only the best was acceptable and have instilled in me an appreciation for the value of education.

I would also like to express my gratitude to the members of the MIND Lab and The Department of Nuclear Medicine for their encouragement. They have made this experience very rewarding and memorable.

Finally, I would like to acknowledge my girlfriend, Zahara, for her patience, love and support over this past year. She has made this endeavor most worthwhile.

TABLE OF CONTENTS

LIST OF TABLES

Table **Page**

LIST OF ILLUSTRATIONS

INTRODUCTION

Diagnostic Imaging and Nuclear Medicine

The application of physics in medicine has gained considerable momentum over the past 100 years. In particular, since the discovery of X-rays in 1895 new modalities in treatment and in diagnosis have carried over from the world of physics to that of medicine. Within the scope of applied physics the area of tomographic imaging has gained considerable attention and importance in the past twenty years.

In general, the use of electromagnetic radiation in imaging is considered non-invasive. The obvious advantage to such *in vivo* techniques has allowed a growth in imaging technology as a diagnostic tool with the development of several imaging modalities specifically designed to meet various clinical needs. These modalities allow clinicians to examine and study internal anatomy and physiology in sufficient detail that may allow them to make an adequate diagnosis of a condition or pathology. They can subsequently implement a course of treatment before any acute effects appear and hence, provide the best medical care.

There are two fundamental classes of techniques used in Diagnostic Imaging. *Nuclear Medicine* techniques give an indication of the state of metabolism and physiology of a system by the measurement of the cumulative activity in a volume of

interest. This activity is proportional to the physiological parameter of concern. *X-ray* techniques are used to construct images of anatomy by the measurement of a physical property of the tissues in the volume of interest. In addition to X-ray techniques, Magnetic Resonance Imaging (MRI) and Diagnostic Ultrasound (DU) are also used for tomographic imaging. Radiographic images differ from those in Nuclear Medicine since they can only represent morphology.

Positron Tomography

As its name implies, Positron Emission Tomography (PET) is an *in vivo* Nuclear Medicine technique that measures the spatial and temporal distribution of positron emitting isotopes that have been administered into the body. The use of positron emitting isotopes in diagnostic imaging dates back to 1951, when it was first proposed by W.H. Sweet. It is also interesting to note that the first positron camera was constructed in 1953 by Brownell and Sweet and it pre-dates, by a number of years, the development of X-ray Computed Tomography (CT) in the 1970's by Cormack (1980) and Hounsfield (1973). However, PET in its present form would not exist without the development of image reconstruction techniques that were originally implemented for CT scanning as well as advances in computer hardware. In addition, advances in detector technology, electronics and image processing have allowed PET to be recognized as the method of choice for *in vivo* measurements of metabolic rates.

PET relies on the coincidence detection of the annihilation photons produced by the annihilation of positrons and electrons. Specifically, pharmaceuticals of particular biological and medical interest are labelled with isotopes that decay by positron emission and then administered to the subject. The most prevalently used positron emitters in clinical practice include ^{11}C, ^{15}O, ^{13}N and ^{18}F. As the radiopharmaceuticals distribute throughout the body, the isotopes decay by positron emission and the positrons subsequently annihilate with surrounding electrons. Data for a volume of interest are acquired simultaneously with several rings of detectors and, hence, the spatial and temporal distribution of the isotope can be measured.

Scatter coincidences (a coincidence in which one or both of the annihilation photons have been scattered before reaching the detectors) and random coincidences (a coincidence event resulting from two separate annihilations) are of significant concern in PET imaging since they lead to the misrepresentation of the activity distribution in the final image. To this regard, various approaches have been taken to minimize or suppress the contribution of scatter coincidences to the data set. These include energy discrimination, and the use of interplane septa that act as collimators, eliminating photons travelling oblique to the scan planes. The use of septa also have a significant effect on the randoms contribution since they will block "singles" photons.

Some important metabolic processes of interest in the brain include blood perfusion, as well as dopamine or glucose metabolism. Activation studies are used to study the response of the brain to specific physical or mental tasks by quantifying

regional cerebral blood flow by measurement of ^{15}O labelled water. Fluoro-deoxy-glucose (FDG), labelled with ^{18}F, is used to study cerebral energy metabolism in health and disease. For example, decreased glucose metabolism in the striatum, a part of the brain that controls mood and locomotion, is characteristic of Huntington's Chorea. In studies of Parkinson's disease a decreased striatal retention of ^{18}F labelled fluoro-L-dopa, a precursor to the neurotransmitter dopamine, is observed. In addition to these studies, investigation of Alzheimer's disease and schizophrenia have been done with PET (Leenders *et al* 1984). The scope of PET studies has expanded to include cardiology and the evaluation of ischemic heart tissue after myocardial infarction, as well as oncology and the localization of primary and secondary tumors in the whole body.

Quantitative Accuracy

Accurate quantitation is necessary if one wishes to determine the kinetics of physiological processes and establish normal and abnormal bounds for a number of important metabolic events. Hence, it has been necessary to investigate the determinates of error and misquantification and then apply adequate corrections.

These corrections include normalization (uniformity correction) to compensate for sensitivity differences between detectors; attenuation correction to compensate for the absorption of annihilation photons within the object; scatter and randoms

corrections to remove events that contribute false position information; and finally dead time and isotope decay corrections to recover true activity.

The current generation of scanners employ Bismuth Germanate (BGO) detectors in a block configuration allowing the simultaneous acquisition of multiple tomographic image planes through the volume of interest. Spatial resolution is typically 5 mm both axially and transaxially and PET images can be quantitated to approximately 5% after all corrections are made.

A limit in spatial resolution is imposed by the physical size of the detector (approximately 6 x 6 mm), the positron range (0 - 3 mm), the slight non-collinearity ($\pm 0.5^{o}$) of the annihilation photons and patient motion.

Sensitivity parameters derived from signal to noise (SNR) considerations should be made with respect to reconstructed image SNR. In this regard, sensitivity parameters can be derived from Noise Equivalent Count (NEC) Rate analysis which has been shown to be a useful parameter for the characterization of PET systems.

Project Scope

Attenuation and scatter corrections have been, and continue to be active fields of research in PET. To date, no preferred scatter correction technique has been developed. The problem of out-of-plane scatter has been addressed by collimation using interplane tungsten septa. The septa are placed between the detectors and extend

to the edge of the field of view of the tomograph. These septa suppress annihilation photons travelling oblique to the scan planes. In addition, the septa reduce the detection of "singles" and, hence, random coincidences. Unfortunately, the septa will also suppress those true coincidences in which the photons are travelling oblique to the planes of interest. As a result, there is a decrease in sensitivity of the tomograph accompanying the reduction of the scatter and random components. In an effort to regain sensitivity, the septa can be removed to allow for the acquisition of data in planes oblique to that of the tomograph's axis. In this work, Monte Carlo simulations are used to study the effect of septa length on scatter contribution and sensitivity of the scanner. Noise Equivalent Count Rate Analysis in used to optimize the septa length for tomographic acquisition.

CHAPTER I

Physical Principles of Positron Tomography

There are many physical principles involved with positron emission, the annihilation process, the interactions of photons with matter, and the detection of these annihilation photons. During or after data collection, appropriate corrections must be applied to ensure that the reconstructed images are an accurate representation of the activity distribution in the object. This chapter will briefly examine the physical principles of modern PET systems and the principles of image reconstruction in PET.

Physics of Positron Emission and Annihilation

The emission and annihilation of positrons is fundamental to PET. When molecules tagged with positron emitters are administered, the spatial and temporal distribution of these molecules can be measured using a PET scanner.

Positron emission is characteristic of unstable, proton rich isotopes which balance their proton/neutron ratio through this process. Positron emission is one form of β-decay. The governing nuclear and atomic equations are given in equations 1.1 and 1.2, respectively.

$$p^{+} \rightarrow n + \beta^{+} + \nu \tag{1.1}$$

$$^{A}_{Z}X \rightarrow {}^{A}_{Z-1}Y + \beta^{+} + \nu + Q + e^{-} \tag{1.2}$$

In positron emission, a proton is converted to a neutron and the (excess) charge is emitted as a positive electron (positron) along with a neutrino (Sorenson and Phelps 1980). The mass of the positron is created from the energy available in the nuclear reaction and any excess energy is shared as kinetic energy between the positron (β^{+}) and the neutrino (ν). An orbital electron has to be ejected from the daughter atom to

preserve charge neutrality. There is a distribution of positron kinetic energies, resulting in a continuous beta spectrum with an endpoint energy of:

$$E_{\beta^+} = (M_X - M_Y - 2m_e)c^2 \tag{1.3}$$

From equation 1.3, it can be seen that positron emission has a threshold energy of $2m_ec^2$ = 1.022 MeV. As mentioned, positron emission is characteristic of unstable, proton rich isotopes. However, these isotopes can also balance their proton/neutron ratio by capturing an orbital electron. The nuclear equation for the electron capture process is given by:

$$p^+ + e^- \rightarrow n + \nu \tag{1.4}$$

The daughter nucleus will typically de-excite to a ground state by 1) emission of X-rays resulting from the capture of an orbital electron and 2) gamma ray emission. Positron emission is always in competition with electron capture. However, since electron capture requires no energy threshold, it is the only mode of decay for proton rich isotopes with less than 1.022 MeV mass difference, such as ^{51}Cr. In general, heavier isotopes with large nuclear charges exhibit a higher probability of decay through electron capture.

Table 1 (deKemp 1992) lists some clinically relevant positron emitters along with some of their physical properties. The stable forms of these isotopes are the building blocks of most biological molecules. Hence, the use of the unstable species in the production of the relevant radiopharmaceuticals does not alter much the biological activity of the molecules of interest.

TABLE 1

PROPERTIES OF SOME COMMON POSITRON EMITTING ISOTOPES

Isotope	Percent β^+ Decay	Half-life	Max Energy [MeV]	Mean Energy [MeV]	Mean Range in Tissue [mm]
^{11}C	99.8	20.3 min	0.97	0.394	1.24
^{13}N	100	10.0 min	1.2	0.488	1.67
^{15}O	100	124 sec	1.74	0.721	2.62
^{18}F	97	109 min	0.635	0.250	0.623
^{64}Cu	19	12.8 hrs	0.656	0.258	0.656
^{68}Ga	88	68 min	1.90	0.787	2.86

Once emitted, the energetic positrons will interact with their surroundings through three fundamental processes: ionization, excitation and bremsstrahlung production. Collisional losses are the predominant mode of energy loss in which

ionization and excitation of the surrounding atoms occurs. Bremsstrahlung or radiative interactions account only for a small fraction of the total energy loss (Knoll 1989). When thermal energies of less than 10 eV are reached positron-electron annihilation becomes energetically favourable. In general, this results in two photon annihilation (without positronium formation).

However, positronium, a state in which an electron and positron orbit each other in a hydrogen like structure can be formed by inelastic collisions when the ionization energy of the surrounding atoms exceeds that of the positron energy. This region is described as the ore gap (Stewart and Roellig 1967). In the ore gap, positronium can exist in two states: triplet ortho-positronium or singlet para-positronium. These states are short lived ($\tau = 1.25 \times 10^{-10}$s for para-positronium and $\tau = 1.4 \times 10^{-7}$s for ortho-positronium). Para-positronium decays by two photon self annihilation, whereas ortho-positronium decays by three photon annihilation, but will also be likely to form para-positronium through atomic collisions.

The overall result is that two photon annihilation is the dominant process. The laws of conservation of energy and momentum dictate that two quanta, totalling $2m_ec^2 = 2 \times 511$ keV be produced, travelling in opposite directions (back to back). Since the positrons will not have zero kinetic energy before annihilation, a slight non-collinearity will result in a deviation of $\pm 0.5^o$ about a mean of 180° (Stewart and Roellig 1967).

The large number of collisions and the varying amounts of energy lost per interaction before annihilation results in many directional changes, and consequently positrons follow a tortuous path through the medium before reaching thermal energies. Hence, the actual range of the positrons is much less than the path length. The range will depend on the number of collisions and therefore on the electron density of the medium:

$$\text{Range} \propto \rho N_A (Z/A) \tag{1.5}$$

where N_A is Avogadro's Number and ρ the medium density (Knoll 1989). Since the ratio of Z/A is nearly constant for all elements, the range is primarily dependent on the medium's density and ranges measured in one medium can be estimated for other mediums by the ratio of the densities. In tissue (or water), positron ranges are typically on the order of 2 mm or less.

Gamma Ray Interactions

The end result of positron decay is the emission of two annihilation photons, each having an energy of 511 keV and travelling at approximately 180° to each other. These photons will also interact with the medium in which they travel, before reaching a detector. The dominant processes are determined by the energy of the photons and

the material in which they travel; they are photoelectric absorption and Compton scattering. In addition, Rayleigh scattering may also occur.

Rayleigh scattering is an elastic scattering process, in which the incident photon "scatters" off an orbital electron resulting in only a change of direction with no loss in energy of the incident photon.

Photoelectric absorption is the process by which an incident photon interacts with a tightly bound orbital electron. The result is the absorption of the photon energy, followed by the ejection of an orbital electron. The photoelectron will have a kinetic energy equal to the incident photon energy minus the electron binding energy (Krane 1988). The minimum energy for photoelectric absorption is the binding energy (the energy required to free an orbital electron) of the electron. It is typically less than 1 keV for mediums of interest like water and soft tissues. K-shell electrons are the most likely orbital electrons to participate in photoelectric absorption and the excited atom will lose its excess energy by the emission of characteristic X-radiation or, alternatively, by the emission of Auger electrons (Knoll 1989).

If photons interact with quasi-free electrons, the process of Compton scattering results. In this case, the incident photon "scatters" off an orbital electron, transferring part of its energy to the electron. The amount of energy transferred to the Compton electron, and hence the energy of the scattered photon depends on the scattering angle. This was first calculated by Compton and is given by the Compton scattering formula (Krane 1988):

$$E_\gamma^{'} = \frac{E_\gamma}{1+(E_\gamma / m_e c^2)(1-\cos\theta)} \tag{1.6}$$

where E_γ and $E_\gamma^{'}$ are the incident and scattered photon energies and θ is the scattering angle. Notice that the scattered photon energies belong to a continuum extending from zero up to a maximum for a scattering angle of 180°, the Compton edge. The probability of scattering through some angle, θ, can be calculated from the *Klein-Nishina* formula (Krane 1988):

$$\frac{d\sigma_C}{d\Omega} = \frac{1}{2}[1+\cos^2\theta)r_o^{\,2}[\frac{1}{1+\alpha(1-\cos\theta)}]^2[\frac{1+\cos\theta}{2}][1+\frac{\alpha^2(1-\cos\theta)^2}{(1+\cos^2\theta)[1+\alpha(1-\cos\theta)]}] \tag{1.7}$$

where Z is the nuclear charge of the medium, r_o=2.818 fm is the classical electron radius and $\alpha = E_\gamma/m_e c^2$. The scattering cross-section is dependent on electron density and increases linearly with Z. Figure 1.1 shows that Compton scattering is the pre-dominant process for photon energies around 511 keV and for low Z materials (tissues). Figure 1.2 shows the contribution of each of the photon interactions discussed to the mass attenuation coefficient of water (tissue). Figure 1.3 shows a

polar plot of the intensity of Compton scattered photons as a function of the scattering angle. Note that for 511 keV photons, $\alpha=1$, and they exhibit forward scattering ($\alpha > 0$), so that there will be little energy loss for relatively large scattering angles.

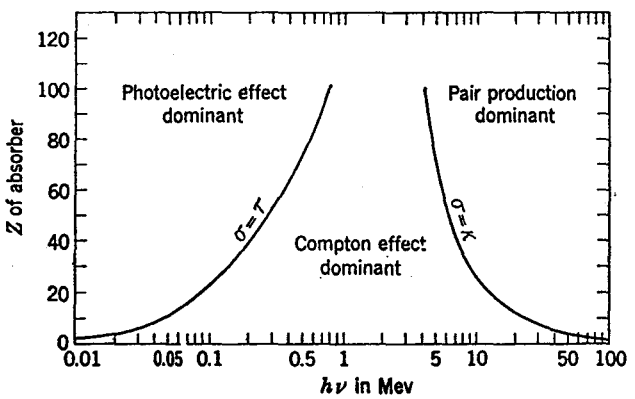

Figure 1.1 Dominant photon interactions as a function of photon energy and atomic number of absorber. For 511 keV photons, Compton interactions are dominant. (Evans 1985, p712).

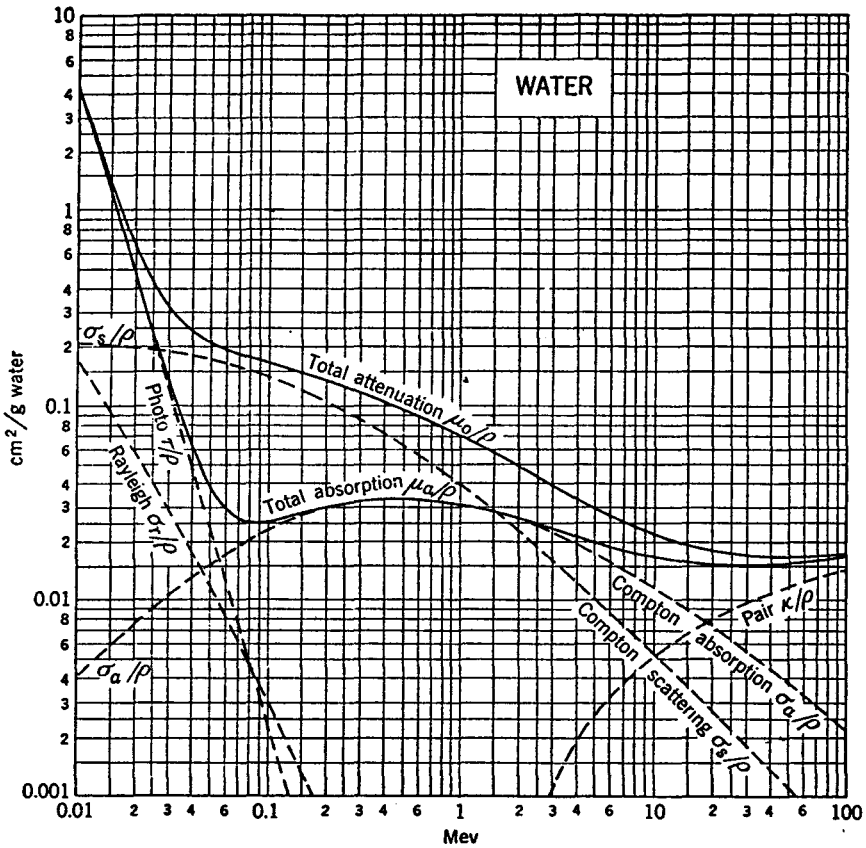

Figure 1.2 Mass attenuation coefficient of water for various photon interactions, as a function of photon energy. For 511 keV photons, the mass attenuation coefficient is dominated by the coefficient for Compton interactions. (Evans 1985, p714)

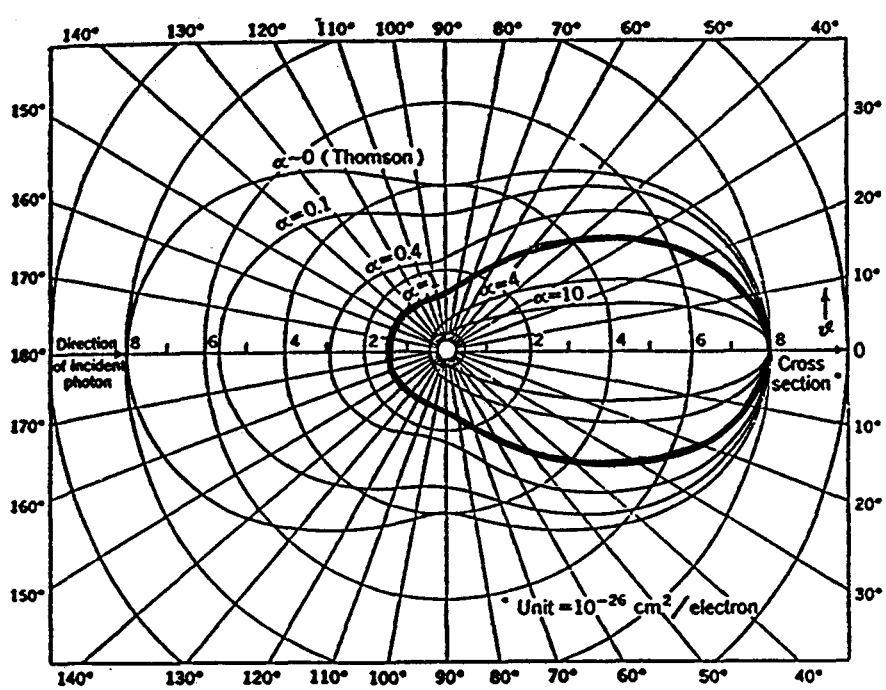

Figure 1.3 Polar plot of intensity of Compton scattered photons as a function of the scattering angle. For 511 keV photons α=1. (Evans 1985, p683)

Data Acquisition and Image Formation

The formation of images in PET relies upon the coincidence detection of the collinear 511 keV annihilation photons resulting from the decay of a positron emitting isotope. The line joining the activated detectors when such a coincidence event is detected is called a line of response (LOR) and indicates that the annihilation event must have occurred somewhere along that line (figure 1.4). When a sufficient number of LOR's have been collected, standard image reconstruction algorithms can be used to reconstruct the positron isotope distribution. In order to appreciate the limitations in performance of a PET system, we must familiarize ourselves with the detection of gamma rays, as well as the principles of image reconstruction from projections.

Detection of Gamma Rays

The current generation of PET systems employ bismuth germanate (BGO) detectors as the detector of choice. BGO is an inorganic scintillation crystal, as is Sodium Iodide (NaI(Tl)) or Barium Fluoride (BaF). In the scintillation process, the incident gamma ray interacts with the atoms forming the crystal lattice, depositing some or all of its energy in the detector. The crystal gives back this energy by emitting scintillation photons of a longer wavelength (505 nm for BGO). Hence, the detector behaves as a wavelength shifter. The light emitted can be converted to an electrical

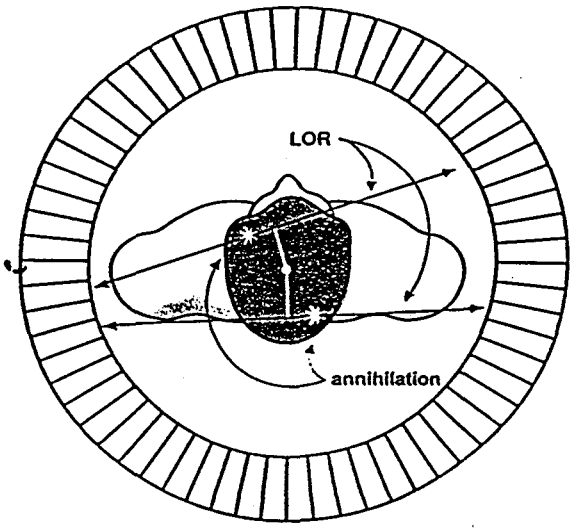

Figure 1.4 Definition of Line of Response (LOR).

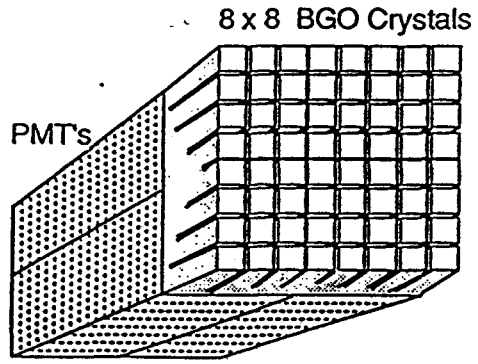

Figure 1.5 Configuration of a BGO block detector.

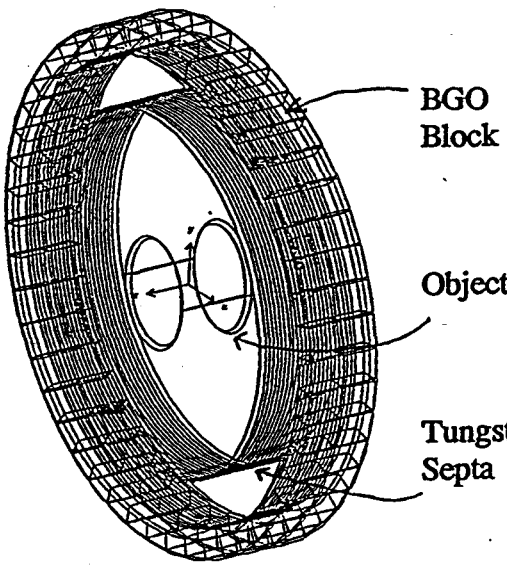

Figure 1.6 Typical set up for a ring tomograph.

signal by coupling the crystal to a photomultiplier tube (PMT). The magnitude of the electrical pulse will be proportional to the total number of scintillation photons emitted and this, in turn, is proportional to the amount of energy deposited by the incident gamma ray in the crystal. Each of these processes are statistical in nature, thereby introducing an uncertainty at each step and this will result in the blurring of the energy response of the detector. Energy resolution is defined as:

$$R = \frac{FWHM}{H_O} \tag{1.8}$$

where H_O is the mean pulse height for a given photon energy and FWHM is the full width of the pulse height distribution at half its maximum.

The energy resolution of BGO is approximately 17 - 20% at 500 keV. This is relatively poor compared to NaI(Tl) which has an energy resolution on the order of 7%. However, bismuth (Z=83) has a high photoelectric absorption probability and results in BGO having the highest stopping power of most available scintillation materials.

Currently, BGO detectors are configured into blocks: a large single crystal is slotted with grooves of varying depth to produce a crystal array, usually 8x8 elements. A set of four PMT's are coupled to the back of the crystal to collect the scintillation light (figure 1.5). The grooves act as light pipes, and, by comparing the relative pulse

height from each of the PMT's, position encoding is possible since each activated crystal element will produce a characteristic light pattern. The blocks are assembled into a ring (figure 1.6).

Ideally, the annihilation photons would interact with the detectors by photoelectric absorption since the photoelectrons produced will have a small range resulting in nearly all the energy being deposited locally. However, Compton interactions are also possible. In BGO, 56% of all events are Compton interactions (Thompson 1993). The Compton edge occurs at approximately 340 keV. The photopeak is centered around 511 keV and given the crystal energy resolution, will extend from approximately 350 to 650 keV. The events recorded between the Compton edge and the photopeak result from multiple Compton interactions of the incident photon in the detector (Knoll 1989). The Compton scattered photons may be long ranged, due to forward scattering and can distribute the original photon energy in a number of crystal elements in the block, and can even escape the detector entirely. Thus, Compton interactions diminish the accuracy of position encoding. This effect has been studied by Thompson (1993) and is most noticeable in crystals near the edge of the block.

Coincidence Counting

The detection of the two photons resulting from an annihilation event is the primary process in PET imaging since it is this coincidence detection that determines the valid LORs.

A time of arrival of a photon in a detector can be determined by the time at which the electronic pulse rises above a threshold voltage, or trigger. The most accurate timing information is produced by pulses with fast and consistent rise times. There are three major uncertainties that degrade timing. Statistical noise in the signal will result in an uncertainty called time jitter; inconsistent rise time for a given signal amplitude will cause rise time walk; and variability in signal amplitude for the same pulse shape will result in amplitude walk of the timing signal. The result of these uncertainties is a distribution of possible arrival times for the photon. In practice, a timing coincidence window, τ_c, is used to account for these effects since signals arriving at the same instant in time will show a distribution of arrival times. Because each scintillator material has a characteristic glow curve, the timing resolution of a system is dominated by the properties of the scintillator and not by those of the PMT's or the associated electronics.

The width of τ_c is largely determined by 1) time of flight difference between photons from the extreme edge of the field of view and 2) τ, the timing resolution of the detectors.

In PET, the field of view (FOV) is given by a specific fan angle (figure 1.7), that is, by the detectors in a ring that are in coincidence with each other.

There are four possible types of coincidences in PET: trues (prompt), scattered, randoms and multiples (figure 1.8). True coincidences, those in which the annihilation photons that form the LOR originated from the same annihilation event and neither photon was scattered, are the only ones from which the true isotope distribution can be deduced. If one or both of the gamma rays are scattered, a scattered coincidence may result. This forms a LOR displaced with respect to the position of the annihilation event and contaminates the data set by contributing false position information. Random coincidences are those in which annihilation photons originating from separate annihilation events strike detectors within the coincidence timing window, again, contributing false position information to the data set. Multiple coincidences are those in which more than two photons were detected within τ_c.

There are some inherent problems introduced by the use of a finite timing coincidence window. In order not to reject any true coincidences, τ_c must be made large enough to account for all statistical uncertainty in the timing of the coincidence circuits (a minimum of 2τ based on timing spectroscopy alone) and size of the FOV, however, τ_c must be kept small enough to minimize contributions from randoms and multiples.

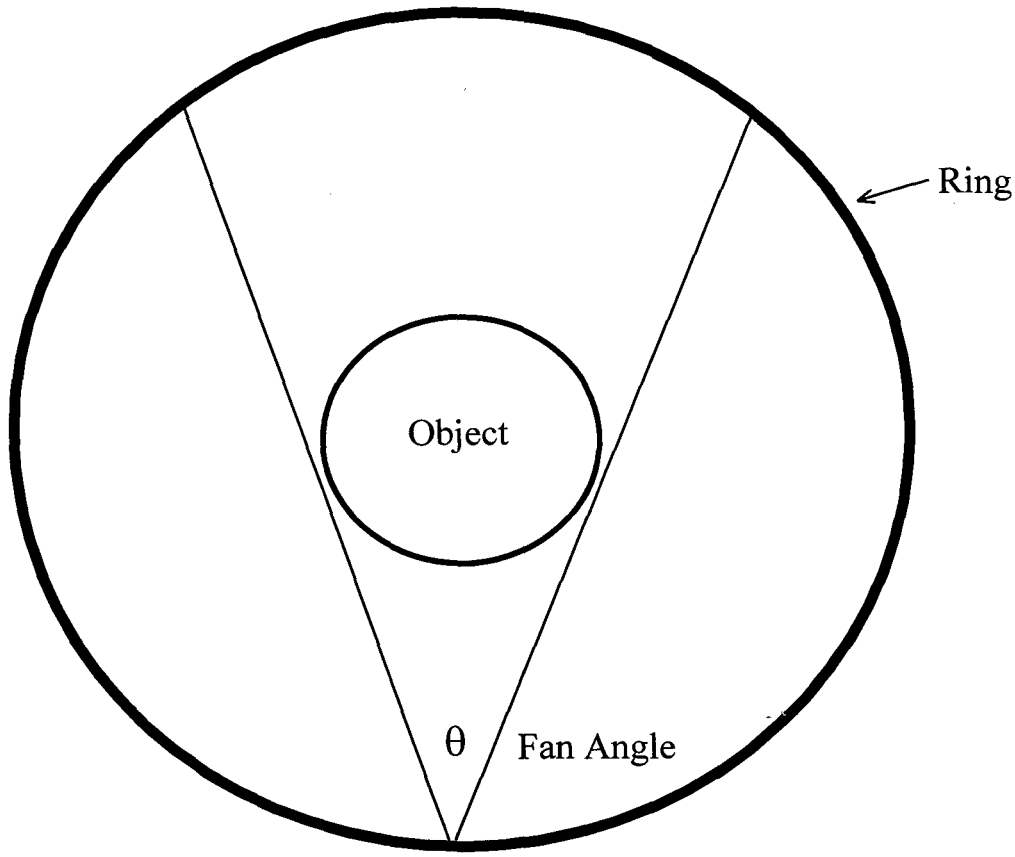

Figure 1.7 Definition of the Field of View (FOV). The fan angle, θ, corresponds to a specific diameter.

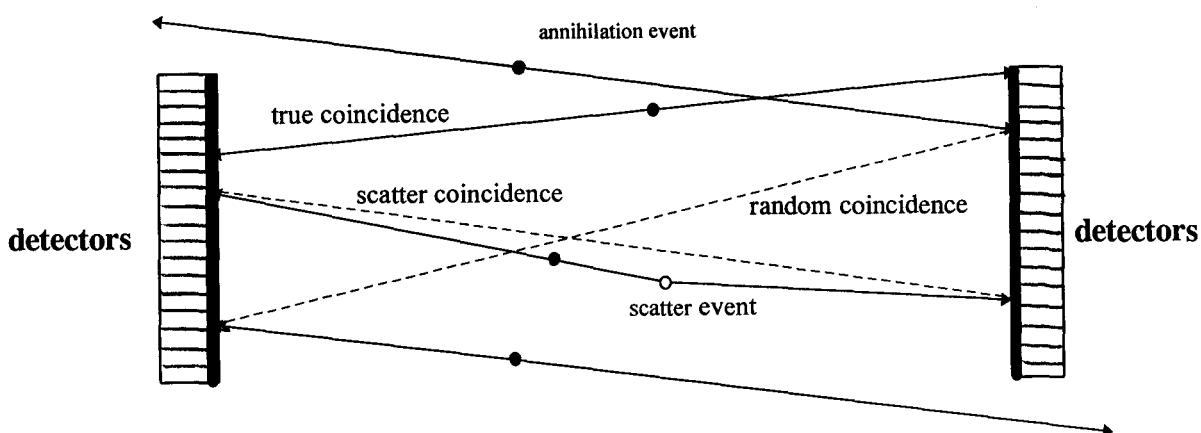

Figure 1.8 Depiction of the four possible types of coincidences that can be detected. True, scatter and random coicidences are shown. A multiple coincidence is formed when more than two detectors are activated.

Sinograms

The LOR's that are collected are sorted into a projection data set, $p(r,\theta)$, by a coincidence processor. Each LOR is assigned a unique (r,θ) pair as shown in Figure 1.9. The $p(r,\theta)$ distribution is called a sinogram since a point source off centre in the FOV will produce a sinusoidal pattern (figure 1.10). The total number of counts recorded for each (r,θ) location is equal to the line integral of radioactivity through the positron isotope distribution, hence, for a given angle, a parallel set of line integrals can be measured, forming one projection through the distribution. The mathematical transform relating image space to projection space is known as the Radon transform. In principle, the distribution can then be recovered by applying the inverse Radon transform if an infinite set of projections at an infinite number of angles is available (Barrett 1984).

PET systems utilize rings of detectors that can collect data for a number of projection angles simultaneously. This configuration is the most efficient. The reconstructed image, however, is still an approximation to the true distribution since only a finite set of projections are collected; for the ECAT 953/31 scanner, 192 distinct projection angles for each of 160 parallel LOR's.

Data can be acquired either in 2D or 3D mode with modern PET scanners. In 2D mode, coincidences are recorded for each ring and between rings, up to a maximum difference of three rings. For 3D acquisition, all crystals within the FOV are

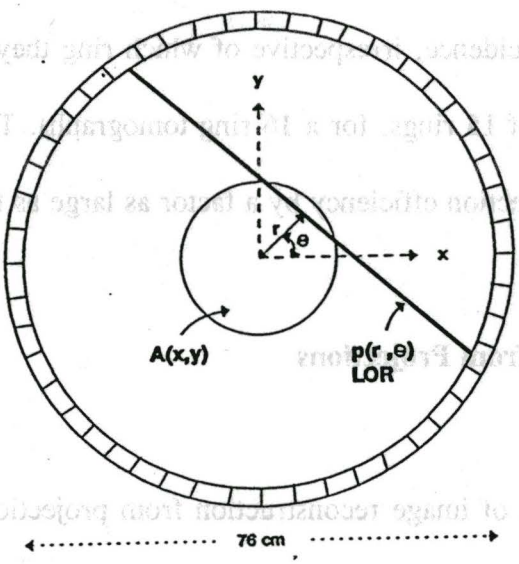

Figure 1.9 Each LOR is assigned a unique (r,θ) pair, which is used to construct the sinogram, p(r,θ).

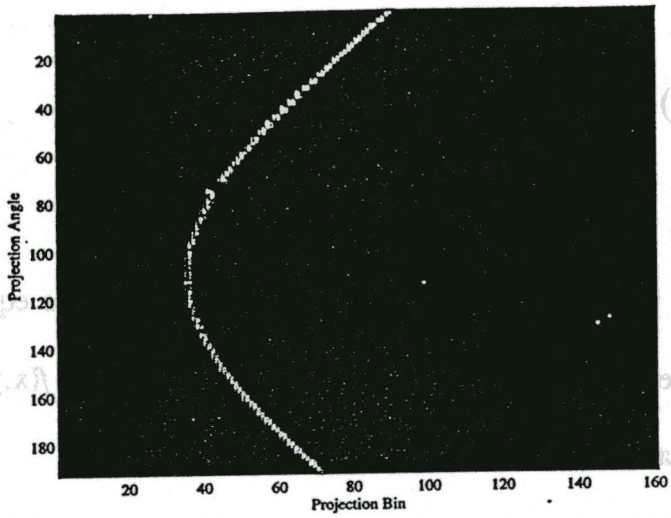

Figure 1.10 A point source off centre produces a sinusoidal pattern in the sinogram matrix.

considered to be in coincidence, irrespective of which ring they belong to (resulting in a maximum difference of 15 rings, for a 16 ring tomograph). This mode of acquisition increases the overall detection efficiency by a factor as large as five.

Image Reconstruction from Projections

The mathematics of image reconstruction from projections has been known for some time and there exist many comprehensive reviews in the literature (Hornich 1986, Herman 1979, Brooks and DiChiro 1976). The projection data are made up of measured line integrals through the distribution given by:

$$p(r,\theta) = \int_l f(x,y)\, ds \quad \text{where } s \perp r \tag{1.9}$$

where $f(x,y)$ is some property of the distribution. In CT, $f(x,y)$ is equivalent to the linear attenuation coefficient, μ, at location (x,y); and in PET $f(x,y)$ is equal to radioactivity concentration, A, at location (x,y).

Given a set of projections at a number of angles, there are two distinct approaches to obtain the activity distribution, A(x,y): analytic methods and iterative methods (Herman 1979).

Simple backprojection consists of adding the counts in a given projection to all the pixels along the path. Mathematically, this is equivalent to:

$$A(x,y) \ \alpha \ \int p(r,\theta)\, d\theta \tag{1.10}$$

and for discrete projections:

$$A(x,y) \ \alpha \ \sum_{\text{LOR's}} p(x\cos\theta + y\sin\theta,\ \theta) \tag{1.11}$$

where $x\cos\theta + y\sin\theta$ is the equation of the path r in the (x,y) coordinate frame. This form of backprojection is inadequate for any quantitative work since simple backprojection is not the inverse operation of projection (Webb 1988). Simple backprojection results in an unwanted background on which the true distribution is imposed. This is because the activity distribution along any LOR is not uniform, as is implied in the simple back projection operation.

The projection data and the image data can easily be related using Fourier Transforms (Herman 1979). Because of the change of variables from polar (projection space) to Cartesian coordinates (image space), a Jacobian is introduced into the reconstruction. The Jacobian has the form of a ramp function, in the Fourier domain. However, since finite spatial sampling is involved, a cutoff frequency is imposed on the

ramp function. The ramp function, bounded by a rectangular window, will yield the best attainable spatial resolution in the reconstructed image, but it will also amplify high frequency components of the distribution, resulting in a noisy image. In practice a window that suppresses the high frequencies is used, trading off spatial resolution for noise suppression. This technique is known as filtered or convolution backprojection and is the most widely used method in practice.

Iterative reconstruction techniques have also been investigated. As in other recursive systems, an initial estimate of the distribution is used as the starting point. The corresponding projection data are calculated by forward projection. A correction factor is introduced to correct for the differences between the measured and calculated projections and another iteration is made. This process continues until some condition is satisfied, i.e. the calculated and measured projections are within some tolerance limit. The choice of iterative and stopping rules are associated with significant problems since they will not only affect the rate of convergence (computation time) but also the quality of the reconstructed image (Brooks and DiChiro 1976).

Reconstructions of 2D and 3D data sets are possible, in principle. However, only recently has the development of algorithms and computer resources been sufficient to make fully 3D reconstruction feasible. 3D reconstruction is attractive since it allows all possible data to be used thereby increasing the signal and consequently reducing the noise in the reconstruction (Townsend and Defrise 1993).

Data Correction

The performance characteristics of PET scanners are limited by many electronic and physical factors (Thompson at al 1992). With consideration to imaging, count rate sensitivity, spatial resolution and contrast resolution of the system are of primary concern. In particular, factors limiting the count rate sensitivity include physical and electronic dead time (Thompson and Meyer 1987), crystal conversion efficiency (Thompson 1992), FOV restrictions and timing coincidence window size (Lupton and Keller 1983). In addition, image quality is degraded by contributions from scattered and random coincidences. Those not only add false position information to the projection data set (Lecomte 1992), but also increase system dead time (as does the contribution from multiples). A recent, comprehensive analysis of counting losses in PET has been made by Casey (1992).

The corrections required to produce adequate quantitation include normalization (uniformity correction) to compensate for sensitivity and efficiency differences between detectors; attenuation correction to compensate for the absorption of annihilation photons within the object; scatter and randoms correction to remove mispositioned events and dead time and isotope decay corrections to recover true activity. The timing uncertainties in the coincidence circuits and pulse rise time impose restrictions on accurate coincidence detection. Statistical limitations are also imposed by the radiation dose (activity) that can be administered safely to a subject. Even with these

corrections, a limit in spatial resolution is imposed by the physical size of the detector, the positron range before annihilation and the slight non-collinearity of the annihilation photons.

Isotope Decay

The activity of any source over a period of time is governed by the decay equation (Knoll 1989):

$$A(t) = A_o\, e^{-\lambda t} \quad where\ \lambda = \frac{\ln 2}{\tau_{1/2}} \tag{1.12}$$

where A_O is the activity at t=0, λ is the decay constant and $\tau_{1/2}$ is the half-life. It is necessary to correct the recorded counts back to zero time. This will allow the time course of physiological measurements to be observed independent of the isotope decay. If the accumulation time for a frame (Δt_{scan}) is significantly long, then:

$$A_o = A(t) \cdot \frac{e^{\lambda t_o}}{1 - e^{-\lambda \Delta t_{scan}}} \tag{1.13}$$

where the numerator corrects the frame back to zero time, the start of the study and the denominator corrects for decay during the acquisition of the frame.

Dead Time

Dead time is the inability of a system to respond to subsequent inputs after the system or detector has been activated by an event. Dead time effects are more severe at high count rates and result in a loss of data. The dead time in a system is determined by the physical properties of the scintillation detectors, the PMT's and the associated electronics. For scintillator-PMT systems, the decay constant for the scintillation process of the crystal is the critical factor in determining the dead time.

The dead time, δ, is the minimum time that must pass before another event can be processed. In non-paralyzable systems, any events arriving while the system is dead will not be counted and will not prolong or extend the time during which the detector is unable to respond. The equation describing this effect is (Knoll 1989):

$$n = \frac{m}{1 - m\delta} \tag{1.14}$$

where n is the true event rate, and m is the observed event rate.

In paralyzable systems, any event that arrives while the system is dead will extend the dead time by δ, even though the second event is not processed. The governing equation is (Knoll 1989):

$$m = n\,e^{-n\delta} \tag{1.15}$$

again, n and m are the true and observed event rates, respectively.

Figure 1.11 compares the behaviour of the paralyzable and non-paralyzable models. For non-paralyzable systems, there is a limit of 1/δ for the observed event rate at high input rates. For paralyzable systems, if the input rate exceeds 1/δ, the observed event rate will begin to decrease. If a system has small dead time losses, both models respond almost identically.

BGO-PMT systems are dominated by paralyzable effects, primarily as a result of the BGO's 300 ns decay constant for the scintillation process to occur.

Normalization (Uniformity)

Since individual detectors and their associated electronics will respond slightly differently to the same input, a normalization (uniformity) correction is required to compensate for the different sensitivities of each detector pair. The normalization

n	true event rate
m	observed event rate
n1, n2	true event rates at which the observed event rates are equal (paralyzable model)
m1	observed event rate corresponding to true event rates n1 and n2
1/δ	maximum observed event rate for nonparalysable system
1/δe	maximum observed event rate for paralysable system

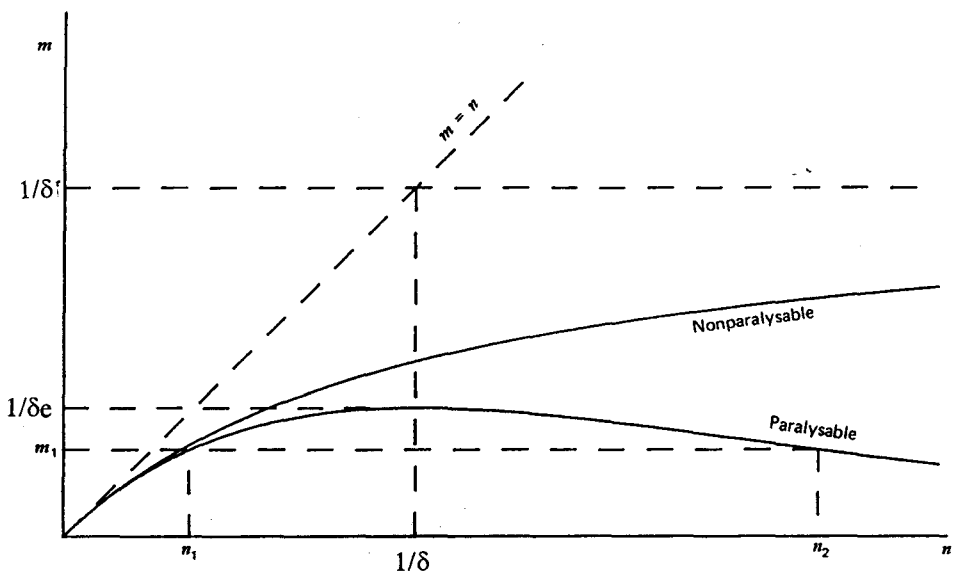

Figure 1.11 Dead time of a system can be modelled as either non-paralyzable or paralyzable. For low count rates, the two behave similarly. (Knoll 1989, p98)

procedure consists of scanning a cylindrical phantom containing a uniform distribution of radioactivity. The tube gains for the PMT's are adjusted until consistent amplification is achieved, followed by plane efficiency scans. Normalization scans measure the sensitivity of individual detectors and are used to compute the normalization factors. These factors are stored and will later be multiplied automatically with the emission and transmission data prior to reconstruction.

Multiples

For completeness, the issue of multiple coincidences is addressed. Multiple coincidences need not be corrected for since they are excluded from entering the projection data set during acquisition. These events are quite distinct from any type of two coincidence event and simple logic circuits in the coincidence processor can identify if more than two detectors were activated within the timing coincidence window, and thus, reject the event. However, these events will add processing time and increase the overall dead time of the system.

Randoms

The use of a finite timing coincidence window to allow for timing uncertainties in the detection system and the size of the FOV results in the recording of coincidences

in which photons originating from separate annihilation events are detected within the timing window. The randoms coincidence rate, for a pair of detectors is:

$$R = N_1 N_2 \tau_c \tag{1.16}$$

where N_1 and N_2 are the single event rates in each detector.

Such coincidences contribute false position information. In practice, a delayed window coincidence subtraction technique is implemented on-line during acquisition to remove the fraction of events attributable to random coincidences from the projection data set. However, these events also require processing time and thus increase the overall system dead time. The method works in the following fashion. During acquisition, all coincidence events that fall within the timing window are accepted. In addition, coincidence events are formed within a time window of the same length, but displaced in time so that the events recorded can only occur by chance. These delayed coincidences are consequently the result of separate annihilation events and are a good estimate of the random coincidence rate. The correction is applied by subtracting the delayed counts from the corresponding LOR's in the emission sinogram.

Attenuation Compensation

The mass attenuation coefficient is defined as μ/ρ, where μ is the linear attenuation coefficient and ρ, the medium density. The attenuation of photon flux through a non-homogenous medium can thus be described by the equation (Webb 1988):

$$I(x) = I_o e^{-\int \mu(x)dx} \tag{1.17}$$

where x is the penetration in the medium and I_0 and I are the incident and transmitted photon flux, respectively.

Projection data are measured in PET by the coincidence counting of the collinear annihilation photons. The annihilation photons will interact within the object with a probability described by the linear attenuation coefficient, μ. The linear attenuation coefficient can be regarded as the probability per unit path length for interaction for both Compton scattering and photoelectric absorption. Hence, more photons travelling along LOR's which have a greater path length through the object will be lost due to photoelectric absorption or scatter of one or both of the annihilation photons. The result is that the activity concentration in the centre regions of the image will appear lower than it should. Figure 1.12 shows the effect of attenuation on .a

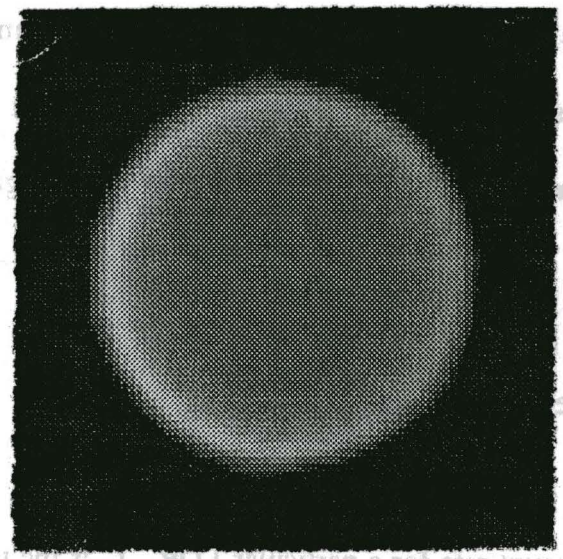

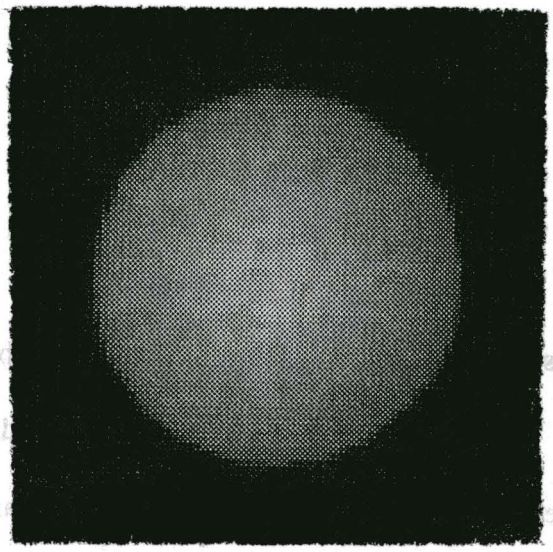

Figure 1.12 The effect of attenuation on a uniform phantom can be seen in the upper image. The centre region appears to have a lower activity. The corrected image (below) shows a uniform activity distribution.

uniform phantom. The image appears more like a dish than a uniform disk. Attenuation correction restores the count along each LOR to their appropriate levels. The total attenuation of the annihilation photons is given by (see figure 1.13):

$$I = I_o \left[e^{-\int_{d1} \mu(x)\, dx} \cdot e^{-\int_{d2} \mu(x)\, dx} \right] = I_o e^{-\int_{D} \mu(x)\, dx} \tag{1.18}$$

where I is the measured count rate for a particular LOR , I_O is the true count rate, $\mu(x)$ is the position dependent linear attenuation coefficient, d1 and d2 are the paths the photons travel in the object and D is the total path. The attenuation correction factor for each LOR is defined as (deKemp 1992):

$$ACF = \frac{I_o}{I} = e^{\int_{D} \mu(x)\, dx} \tag{1.19}$$

Because the ACF depends only on D, the total path through the object, and not on the individual paths of each annihilation photon it can be measured using a procedure similar to CT. An external source rotates around the object and a blank scan to measure I_O, where there is no object in the FOV, and a transmission scan to measure I, with the object in the FOV, are acquired. ACF's are calculated as simply the ratio

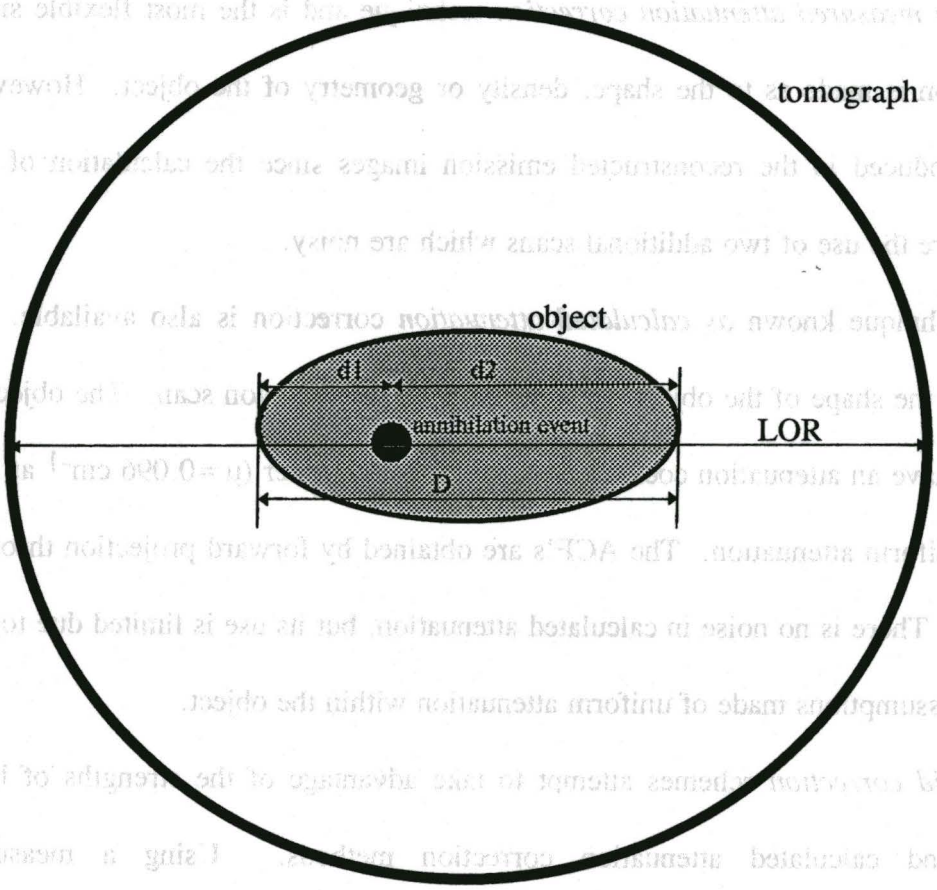

Figure 1.13 The total attenuation of the annihilation photons depends only on the total path length through the object, and not on the individual paths of each photon.

between the two scans. The emission scan is then corrected by multiplying the emission data with the ACF's.

In multi-ring systems, a rod source rotating at the edge of the FOV is used so that the ACF's for all image planes can be measured simultaneously. This technique is known as the *measured attenuation correction* technique and is the most flexible since no assumption is made as to the shape, density or geometry of the object. However, noise is introduced in the reconstructed emission images since the calculation of the ACF's require the use of two additional scans which are noisy.

A technique known *as calculated attenuation* correction is also available. In this method, the shape of the object is estimated from the emission scan. The object is assumed to have an attenuation coefficient equal to that of water (μ=0.096 cm^{-1} at 500 KeV) and uniform attenuation. The ACF's are obtained by forward projection through the data set. There is no noise in calculated attenuation, but its use is limited due to the underlying assumptions made of uniform attenuation within the object.

Hybrid correction schemes attempt to take advantage of the strengths of both measured and calculated attenuation correction methods. Using a measured transmission scan, the boundaries between tissues are identified and the image segmented into different tissue classes. Using a known attenuation coefficient for each class, the image can be forward projected and the ACF's calculated for each LOR (Tomitani, 1987). The technique is sensitive to edge determinations since any

misclassification will result in either an under or overestimation of the attenuation along the LOR's.

Measured attenuation correction has traditionally been implemented in coincidence mode; in this mode a positron emitter is used as the external source and the coincidence circuitry is used to define the LOR's. A recent modification to this technique involved the development of singles transmission measurement (deKemp 1992). In this technique, the coincidence condition is removed and measurements are made based on the singles events rates in the detectors. More recently, the use of other gamma emitters has been investigated for singles acquisition since the coincidence requirement has been removed (Yu and Nahmias, 1995).

Scatter Compensation

Scatter in PET is a major problem, contributing to the degradation of quantitative accuracy. Scattered coincidences arise when either one or both of the 511 keV annihilation photons are Compton scattered in the object. This results in the formation of a LOR, which is displaced with respect to the correct LOR (figure 1.9). This contributes false position information into the projection data set. The mispositioned events decrease image contrast since events from high activity regions are misplaced to regions of low activity. The effect is a blurring or skewing of the activity distribution.

Scatter in tomographic imaging, with the use of septa and energy discrimination, is typically on the order of 10 - 20% (depending on the size of the FOV and source distribution). In 3D imaging, septa have traditionally been removed and studies show that scatter contribution can be as high as 50%.

Compton scattered photons have lower energy than that of the initial photons, and altered paths. These two properties form the basis for scatter suppression and scatter correction technique.

Scatter Suppression

Scatter suppression techniques use energy discrimination to reject photons that do not fall within a specified signal window, typically 350 to 650 keV for BGO. This ensures that some of the scattered coincidences are excluded and do not enter the sinogram data during acquisition. However, due to the relatively poor energy resolution of BGO, this technique is not at all sufficient. The 511 keV annihilation photons exhibit forward scattering (figure 1.3) and therefore, even for relatively large scattering angles there are only small changes in energy. For example, a 511 keV photon scattering through an angle of 45° will still have an energy of almost 400 keV, (equation 1.6). When compared to the energy resolution of BGO, this photon energy still falls within the photopeak window that extends from 350 to 650 keV. Energy

discrimination is only useful for suppressing coincidences resulting from multiple and large angle scattering.

Another approach to scatter suppression is the use of interplane septa to prevent the acquisition of gamma rays scattered oblique to the scan planes (figure 1.14). In this case, it is useful to define what is meant by in-plane and out-of-plane scatter. In-plane scatter results in a false LOR being formed somewhere within the plane that the correct LOR would be formed, hence, the scattering remains in-plane. Out-of-plane scatter produces a LOR in a plane that does not correspond to the plane that the correct LOR would be formed in . Septa are effectively collimators composed of high Z materials, typically tungsten or lead, and that extend from the face of the detectors to the edge of the FOV. Septa collimate photons into planes orthogonal to the tomograph's axis (figure 1.14) so that some proportion of photons scattered out-of-plane, are eliminated. This is due to absorption of the scattered photons in the septa, which are several mean free paths thick (Thompson 1993).

Scatter Correction

Scatter correction techniques used in PET can be classified as either energy based scatter correction or filtered scattered correction.

The dual energy window scatter correction (DEWSC) method is based on the acquisition of data in two non-overlapping energy windows. The *photopeak window*

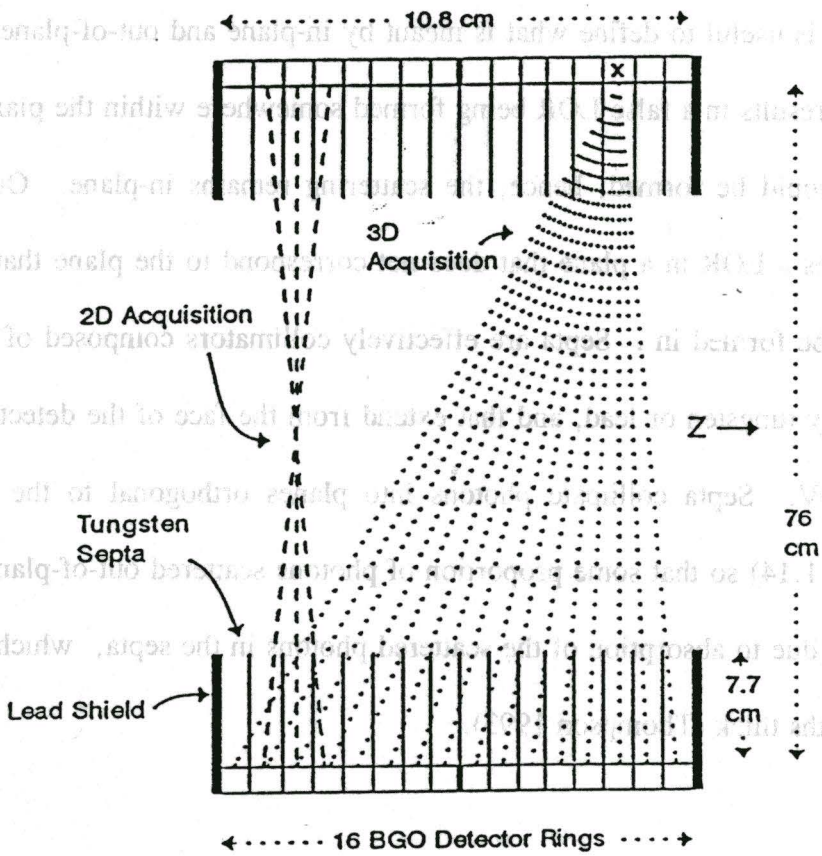

Figure 1.14 Trans-axial view of tomograph showing the collimating effect of septa on photon paths oblique to the image planes.

acquires data around the isotope's emission energy, and the *Compton window* acquires data in a low energy window. The technique was first introduced by Jaszczak for SPECT imaging (Jaszczak 1984) and modified by Grootoonk *et al* for PET. Two assumptions are necessary: the profiles in the Compton and Photopeak windows have similar line spread functions, and an adequate scaling factor, relating the counts in the scatter window to the scatter counts in the photopeak window, can be determined from simple phantom measurements. The equations are:

$$\begin{aligned} P_T &= P_S + P_U \\ C_T &= C_S + C_U \\ R_S &= C_S / P_S \\ R_U &= C_U / P_U \end{aligned} \tag{1.20}$$

where P is the *photopeak window* and C the *Compton window*. The subscripts T, S, U represent the total, scattered and unscattered count rates respectively. The ratios of the scattered and unscattered counts in each window is given by R_S and R_U, respectively (Grootoonk *et al* 1993). The four equations can be solved for the unscattered events in the photopeak, this is given by:

$$P_U = \left(\frac{R_S}{R_S - R_U}\right)P_T - \left(\frac{1}{R_S - R_U}\right)C_T \tag{1.21}$$

With this technique, the ratios R_S and R_U are assumed to be constant for the given energy windows, objects and source distributions. Typical settings for the energy windows are 200-380 keV for the *Compton window* and 380-650 keV for the *photopeak window*. The ratios are measured and calculated for lines sources in water (scattered) and air (unscattered). The technique has met with limited success for use with non-uniform attenuation objects.

Filtered scatter correction techniques use estimates of the point response of the system by measuring the point spread functions for a point source of activity. The real distribution can be regarded as the superposition of many point sources and therefore, deconvolution or convolution subtraction of the acquired projection data allows an estimate of the scatter profile to be calculated. Accuracy of the scatter correction is dependent on the ability to develop point spread functions that vary with the mass distribution within the object and source position. The deconvolution method has been recently applied to PET (McKee *et al* 1992). In this method, the scattered component is modelled as the convolution of the unscattered projection with a position independent point spread function (PSF). Using Fourier transform techniques, deconvolution is quickly and easily accomplished in Fourier space. This is especially desirable since it can be implemented as a modified filter function when using filtered backprojection for image reconstruction. The technique is limited due to the assumption of a position and density independent PSF. Convolution subtraction techniques were proposed in 1983 by Bergstrom *et al*. The method models the scattered component as the convolution of

measured projections with a particular PSF. Unscattered projections are calculated by performing the convolution of the PSF and subtracting the scattered component. The advantage to this method is the use of a flexible PSF since no Fourier Transforms are required, its drawback is considerable computation time in performing the convolution. Iterative techniques have subsequently been proposed to speed up the computation (Shao and Karp 1991). More sophisticated and accurate techniques have been proposed based on previous iterative methods (Barney *et al* 1993) and offer the best compromise between accuracy and computation time and have become the technique of choice.

Hybrid techniques which perform scatter correction based on energy and convolution corrections have also been proposed recently. The extraction of trues method was introduced by Bendriem *et al* (1994) and retractable septa scatter correction was proposed by Cherry *et al* (1993).

Analytical approaches to scatter correction have been prohibited due to the great amount of computing power that must be dedicated to the solution. However, a theoretical framework has been developed by Bowen (1994) upon which practical scatter correction techniques can be developed later.

It should be noted that scattering effects are not just limited to the object since photons reaching the detectors are also likely to be Compton scattered within the detector block resulting in inaccurate position encoding and energy registration.

CHAPTER II

Monte Carlo Techniques in PET

The Monte Carlo method has gained wide spread acceptance and importance in the field of Medical Physics. With the advent of adequate computing resources and the generalization and popularization of a number of Monte Carlo codes, these techniques are used not only to evaluate proposed experimental and analytical techniques in scatter and attenuation correction, but also to investigate the factors governing the PET systems response. This chapter serves to introduce the underlying principles in the application of the Monte Carlo technique and provides a description and verification of the Monte Carlo package used in this study.

Principles of the Monte Carlo Method

The motivation for the use of Monte Carlo techniques is that if the geometry and materials of a system are defined adequately, the Monte Carlo method can be used to study such systems without making any of the simplifying assumptions that are generally required to solve the problem analytically. System parameters can be examined and varied, in order to determine which experiments should be performed and which will yield the most useful results. In addition, the ability to examine each step in detail (from input to output) allows one to gain understanding of the importance of each process, and to optimize the system as a whole. Photon and particulate interactions with matter are stochastic processes i.e. the interaction coefficients can be described as either a probability per unit time or probability per unit path length and, as such, are ideally suited for Monte Carlo studies. By sampling from the probability distributions of possible events, an event history can be created. After a sufficient number of histories (as to be statistically significant) are acquired, they can be examined and analyzed in the study of the system. The use of Monte Carlo methods extends through all areas of Medical Physics including Nuclear Medicine, Diagnostic Radiology, Radiotherapy Physics and Radiation Protection (Andreo 1991).

Random Number Generators

At the heart of every Monte Carlo code is a random number generator (RNG). The RNG is the basis for sampling the probability distribution. The most common RNG's are based on Lehmers's method, also known as the multiplicative-linear-congruential method (Knuth 1969), and result in the sampling of a uniform probability distribution. It is given by the following formula:

$$\xi_i = (A\xi_{i-1} + B) \text{ modulo } M \qquad (2.1)$$

where A and B are constants, ξ_i is the random number and M is chosen to be 2^b, *b* being the number of bits in the integer representation of data in the computer. This type of RNG is a pseudo-RNG since it does have a repetition period, but if A, B and M are chosen carefully, this formula is sufficient for most Monte Carlo simulations. Periods on the order of 10^9 are not uncommon. In addition, the RNG must be "seeded" with an initial value which makes the pseudo-random sequence unique from all other sequences.

Probability Distributions

RNG's generate random numbers from a uniform probability distribution i.e. one in which every possible outcome is equally likely. However, most physics processes are characterized by unique probability distributions. The probability of a random variable X, which lies on the interval $[x_1,x_2]$ is given by (Peebles 1993):

$$\text{prob}(x_1 < X < x_2) = \int_{x_1}^{x_2} p(x)\, dx \tag{2.2}$$

where p(x) is the probability density function of X. Equation 2.2 can be readily generalized to higher dimensions.

For photon and particulate interactions, p(x) can be derived from the cross-sections for various types of interactions (Morin 1988). The transformation from a uniform to the desired probability density function is made by (Peebles 1993):

$$\int p(x)\, dx = \int du \tag{2.3}$$

where *du* is drawn from the uniform distribution on the interval [0,1] implying that p(u)=1, and p(x) is the desired probability density function. The equation can be simplified to:

$$\int p(x)\,\mathrm{dx} = \mathrm{u} \quad \text{for } 0 < \mathrm{u} < 1 \tag{2.4}$$

A particular probability density function, found in many scientific and engineering applications is the Gaussian (Normal) distribution. It is given by:

$$p(x) = \frac{1}{\sqrt{2\pi}} e^{\frac{-x^2}{2}} \tag{2.5}$$

where a mean of zero and standard deviation of one have been assumed. In order to sample from this distribution, the transformation in equation 2.4 is applied. Therefore:

$$\int_{-\infty}^{x_o} e^{\frac{-x^2}{2}}\, dx = \sqrt{2\pi}\, u \tag{2.6}$$

There is no closed form solution to this integral and therefore, for any *u*, the integral must be solved numerically for x_o. In practice, a look-up-table and linear interpolation

is often used, however, an elegant solution was proposed by Box and Muller (Bevington and Robinson 1992):

$$z = \sqrt{-2 \ln r_1} \cos 2\pi r_2 \tag{2.7}$$

where z is the Gaussian random variable and r_1 and r_2 are drawn from uniform distributions. This solution was derived on the basis of a 2D Gaussian function and is beyond the scope of this work (see Bevington and Robinson 1992).

The exponential function is another fundamental function which appears in many natural and physical processes and the probability density function is easily derived:

$$p(x) = \lambda e^{-\lambda x} \tag{2.8}$$

where λ can represent any transition or interaction probability. Therefore, applying equation 2.4, the random deviate, x, from p(x) can be found as:

$$x = \frac{-\ln(u)}{\lambda}, \qquad 0 < u < 1 \tag{2.9}$$

Event Histories

Event histories in radiation physics are not usually comprised of only single events since any single interaction will usually result in a number of photons and particles being generated and those will also have to be followed. Hence, the user of the Monte Carlo code must decide on the necessary and sufficient history to be recorded.

In PET imaging, it is the photon histories that are of primary concern. The particles contribute to the radiation dose to the object, but do not participate in image formation. Hence, it is appropriate to trace the photon history for each annihilation photon from the annihilation event location, through the object to the detector array only. The interaction history, and the energy deposited in the detector are sufficient to perform position encoding and energy discrimination, as with real systems. In addition, the degree of misposition of scattered and random counts can be known exactly, information that is not available from real systems. Profiles of the projection data can also be constructed and analyzed, allowing an analysis of the systems response.

The *Geant* Monte Carlo Code

The *Geant* Monte Carlo code is the culmination of many hundreds of man-years of development, starting in 1974 with a code for the tracking of a few particles through simple detectors and geometries (Geant User's Guide 1992). The program was designed for use in high energy physics at CERN and has evolved into a sophisticated package which is now widely distributed.

The implementation of the base *Geant* Monte Carlo code for use in PET was done by C. Michel at Louvain-la-Neuve and colleagues at CERN in the late 1980's. The validation of the code was reported in 1991 for PET Scanners with and without interplane septa (Michel *et al* 1991). The programs developed by Michel form the basis of the code used in this work. Some modifications have been made to record and extract data of particular interest.

A full simulation is performed in three stages. The first stage consists of defining the geometry and materials of the PET system, as well as the source distribution. The second stage involves tracking and acquiring the photon histories for each annihilation event. The third and final stage requires analyzing the history file by defining the appropriate signal window in addition to simulating the logic of the coincidence circuits. An overview of each stage is provided.

Definition of the Acquisition System

The *Geant* code allows for complex geometry definitions by using a "Russian Doll" approach. This is accomplished by defining "mother" and "daughter" volumes each of a specific shape such as boxes, cones, cylinders, tubes, spheres or other polygonal shapes. Up to 15 levels in the geometry can be defined by the superposition of "mother", "daughter" and "grand-daughter" volumes. The size of each of these volumes is variable. Hence, all physical items of the acquisition system can be defined and positioned mathematically using mother coordinate and local coordinate systems. Materials are defined either as elements or compounds; the local material definition has precedence over the mother material definition.

In the simulation, the tomograph gantry is defined as a large cylinder in a vacuum, and would be considered a "mother" volume. The block detectors would correspond to "daughter" volumes and the individual detectors as "grand-daughter" volumes. Similar definitions are used to specify the septa, side shielding and object phantom. The geometry and scale of the tomograph is carefully defined to be as realistic as possible.

The detector response is the only process which is not simulated completely. Block detectors respond through the scintillation process; however, in the simulation, the process terminates before this step as the energy deposited in the individual crystals is recorded according to photoelectric and Compton interactions in the crystal, ignoring

the scintillation process. The energy deposited in the crystal is then blurred according to the resolution of the detector in order to simulate better the response.

Photon Tracking and History

After a source distribution has been defined, and neglecting the positron range, an annihilation location is selected randomly. The photons resulting from the annihilation are assumed to have an energy of 511 KeV, to be collinear, and emitted in some random direction. A variance reduction or stratification technique is employed to increase the efficiency of the simulation (Michel *et al* 1991). The photons are restricted by a solid angle of release of 30° to eliminate photons that have little probability of ever reaching the detectors. This assumption is reasonable because the axial acceptance angle of the tomograph is approximately 8° from the centre of the FOV. The choice of a 30° stratification angle results in an effective doubling of the efficiency of the simulation since it covers 50% of the 4π solid angle, in which detection is possible.

A single event history requires the tracking of both annihilation photons through the material and the geometry of the scanner. This is accomplished by considering the cross-sections for photoelectric absorption, as well as for Compton and Rayleigh scattering, for the various materials encountered. Compton scattering is governed by the *Klein-Nishina* differential cross section and the scattered photon energy determined

by the Compton equation. The photoelectric and Rayleigh cross-sections are determined using semi-empirical relations that are valid for specific energy ranges. In order to determine most accurately the energy deposition in the detectors the photoelectrons and recoil electrons from the photoelectric and Compton processes are also tracked with respect to the stopping power of the medium.

Tracking is performed using a discretized step size between interactions. The interactions are characterized by the survival fraction:

$$prob_{\text{survival}} = e^{-\mu\Delta x} \tag{2.10}$$

where μ is the linear attenuation coefficient for the interaction and Δx the step size. This method is valid for the three photon interactions being considered. Following the method of equation 2.9, the step size for each interaction is given by:

$$\begin{aligned} \Delta x_{PE} &= -\ln(R_1) / \mu_{PE} \\ \Delta x_{Compton} &= -\ln(R_2) / \mu_C \\ \Delta x_{Rayleigh} &= -\ln(R_3) / \mu_R \end{aligned} \tag{2.11}$$

where R_1, R_2 and R_3 are random numbers drawn from uniform distributions. The interaction with the smallest step size is deemed to have occurred. For each interaction, the position, energy and direction of the photons are updated before the

next interaction occurs. When crossing boundaries the interaction lengths are recalculated and μ's are updated for each energy and material. In the simulation, a cutoff energy of 50 keV is imposed, at which time a terminating photoelectric interaction is assumed to occur. The position, energy and scatter history of the photons are stored in a history file for further analysis. In order to study Compton scattering, a "Compton Number" giving the total number of Compton interactions is recorded using the following convention:

$$CN = \text{septa} * 100 + \text{Object} * 10 + \text{detector} \tag{2.12}$$

where *septa*, *object* and *detector* are the number of Compton interactions in these media. For example a CN of 123 indicates that one scatter occurred in the septa, two in the object and three in the detector. The "Compton Number " is a composite index for both annihilation photons implying that the Compton interactions for both annihilation photons are recorded by a single "Compton Number".

Analysis

The analysis portion of the Monte Carlo simulation is the point at which all relevant data i.e. the true, scattered and singles along with energy and activated detectors can be extracted. Relevant parameters such as scatter fraction and NEC rates

can then be calculated. Sinogram profiles and energy spectra for the detected events can also be constructed which are specific enough to include profiles for unscattered, singly scattered or multiply scattered photons. In the analysis program, the history file is read in and the data organized into sinogram format. True and scattered coincidences can be distinguished through the use of the "Compton Number". In addition, acquisitions with different energy windows can also be simulated

Since the Monte Carlo program is time independent, dead time and random coincidences cannot be simulated and must be estimated by other means.

Modifications to Original Monte Carlo Code

The original routines have been modified somewhat for this work. The analysis routines have been generalized so that data from individual scan planes can be retrieved from the history file and the true, scattered and singles be scored. This is useful for studying the count rate sensitivity and NEC rate of individual image planes, particularly if a varied septa length configuration is being studied. These modifications also take into account the plane to slice mappings (mashing) employed by the scanner operating in tomographic mode as shown in figure 2.1.

In order to simulate the scanners response accurately, the coincidence conditions include whether or not the LOR is within the FOV and if it is within the sinogram, since a restricted FOV is often used in practice. This is accomplished by comparing

each LOR to a look-up-table of all valid LOR's. The program has been modified to recognize a general coincident event given the x, y, z position of the annihilation along with the initial polar and azimuthal angles of the annihilation photons. Hence, it is now possible to determine coincidences within a 3D grid and create a 3D data set or employ single or multi-slice rebinning. With these modifications, Positron Volume Imaging (PVI) systems can be more accurately modelled. Knowing the exact position of the annihilation event allows us to determine which detectors should have been activated, and hence, Compton scattering in the object can be studied more carefully, specifically, separating small and large angle scattering or the components of in-plane and out-of-plane scatter to the total

scatter fraction. In addition, the degree of scattering within the detector block can be determined and the amount of mispositioning be calculated.

A functional description of the codes and modifications can be found in Appendix A.

Verification of Monte Carlo Simulation

The original validation of the Monte Carlo code was done by C. Michel *et al* (Michel *et al* 1991). Spatial resolution (axial and transaxial) from line sources in various positions in the FOV, sensitivity and scatter fraction for various geometries and energy windows, were obtained, and the results were compared to experimental

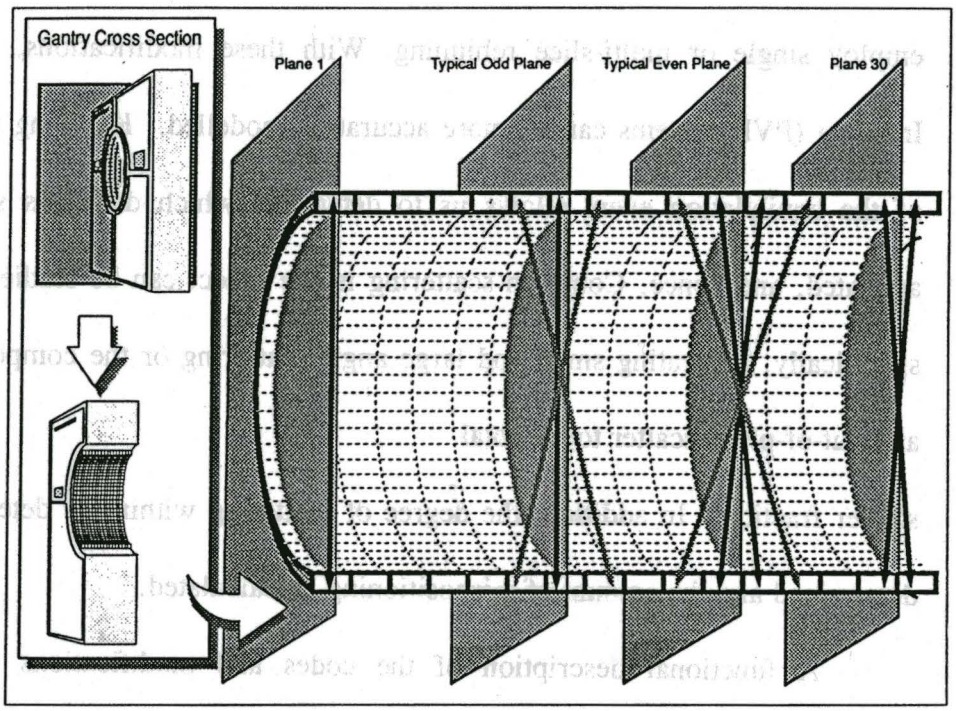

Figure 2.1 Cross section through the tomograph gantry showing the slice to plane mappings (mashing) used when operating in 2D mode.

measurements on scanners with and without interplane septa. Overall, the simulation showed excellent agreement with experimental results, typically within 10%.

More recently, the underlying assumptions of perfect collinearity, negligible positron range, the 25% energy resolution of the detectors and the use of a stratification angle have been tested by C. Bowen (1994). Experiments included the measurement of profiles of line and point sources in water cylinders with acquisition windows of 250 - 850 keV and 380 - 850 keV. Figures 2.2 and 2.3 (from Bowen 1994) show normalized Monte Carlo generated and PET profiles of line and point sources in a water filled phantom. Agreement is excellent throughout the entire profiles. There are two distinct regions in these figures: the broad scatter tail and the resolution peak. The scatter tail results from scattering of the annihilation photons within the phantom. The PET resolution peak appears slightly broader due to the small mispositioning of the line source in the phantom which causes it to precess around the centre bin since the source is off centre. Figures 2.4 - 2.6 (from Bowen) serve to illustrate further the validity of the assumptions. Results for the tests of the effect of positron range and non-collinearity are shown in figure 2.4; these effects are indeed negligible. Figure 2.5 shows the distribution of initial axial angles that result in the detected coincidences. From this figure, the use of a 30° stratification angle is justified. The final assumption of being able to blur the recorded energy with a 25% FWHM Gaussian for BGO detectors is tested in figure 2.6. The PET energy spectrum

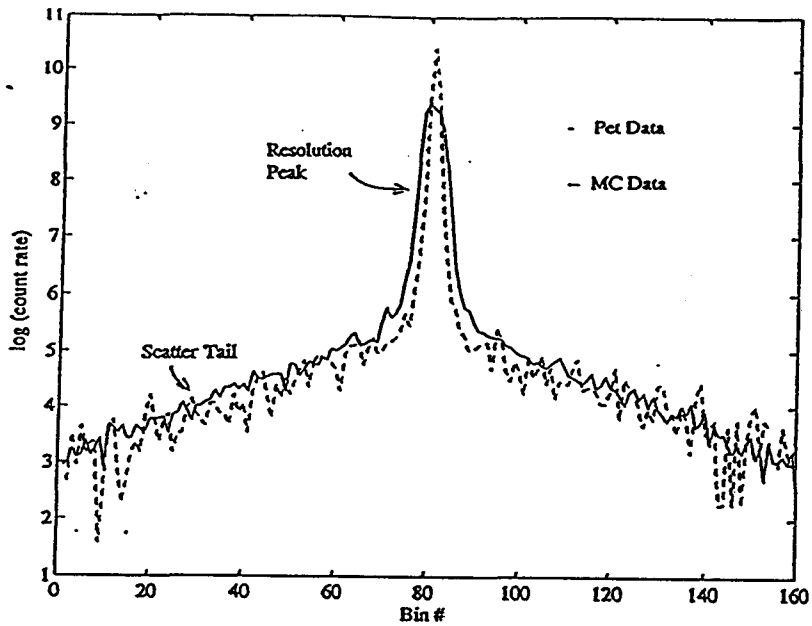

Figure 2.2 . PET and MC profiles of a 5 mm diameter line source of ^{18}F centered in a 20 cm diameter water-filled cylinder. 2D acquisition from 250 - 850 keV using septa with summation over all 192 projection angles and all 31 axial slices. (Bowen 1994, p97)

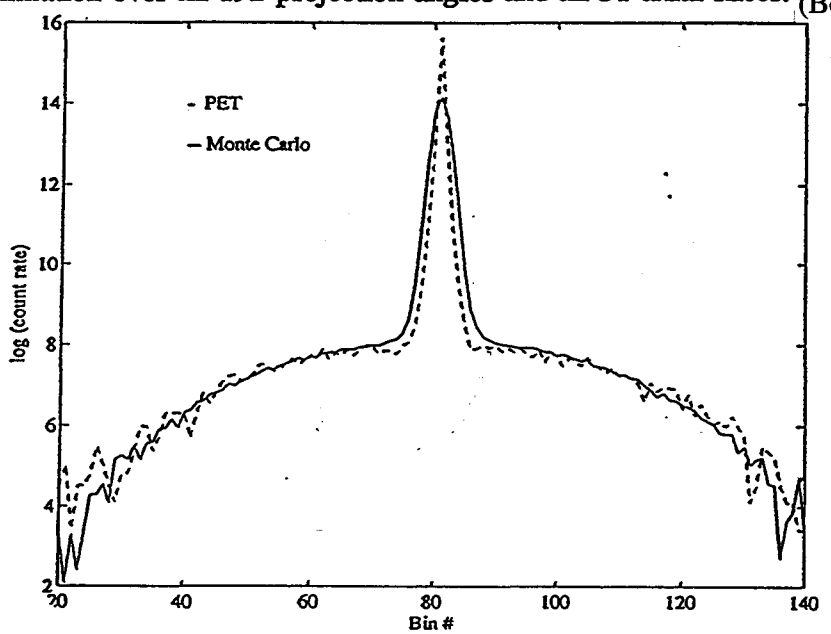

Figure 2.3 PET and MC profiles of a point source of ^{18}F centered in a 20 cm diameter water-filled cylinder. Source plane shown with summation over all 192 projection angles. Acquisition from 380 - 850 keV without septa. (Bowen 1994, p97)

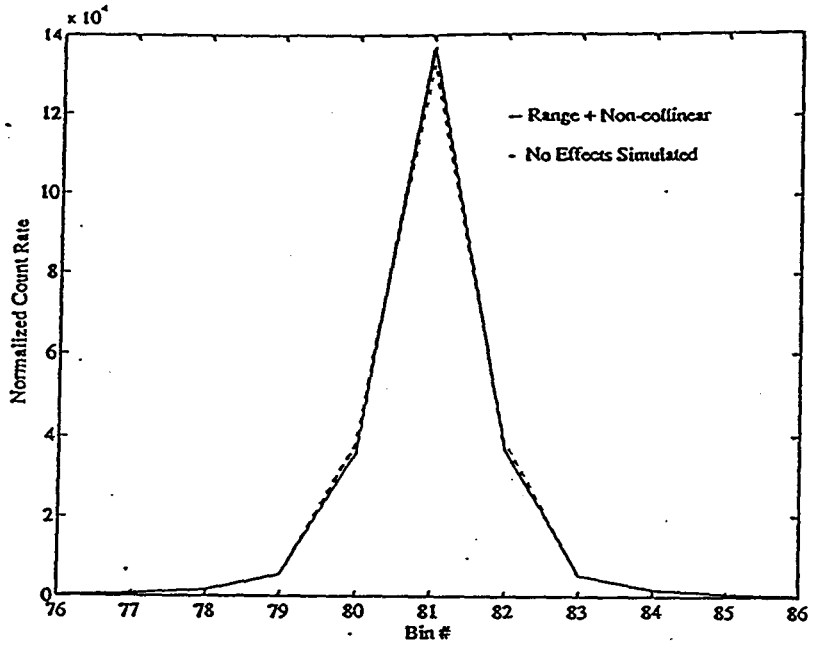

Figure 2.4 Resolution peak profiles for MC simulations of a line source of ^{18}F in air positioned at the center of the field of view. Simulations are with and without positron range and γ-ray non-collinearity effects included. (Bowen 1994, p101)

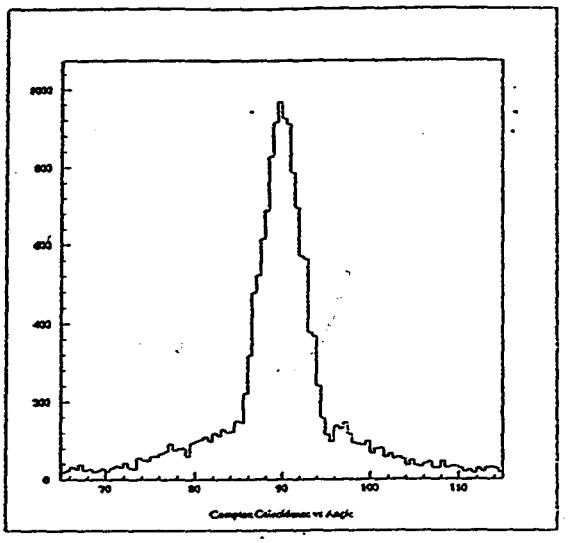

Figure 2.5 Distribution of initial axial angles of annihilation photon pairs which produce scatter coincidence lines of response. Plot is for a line source of positrons centered in a 20 cm water-filled cylinder. (Bowen 1994, p101)

is fitted well by a 25% FWHM Gaussian function and justifies the use of this technique.

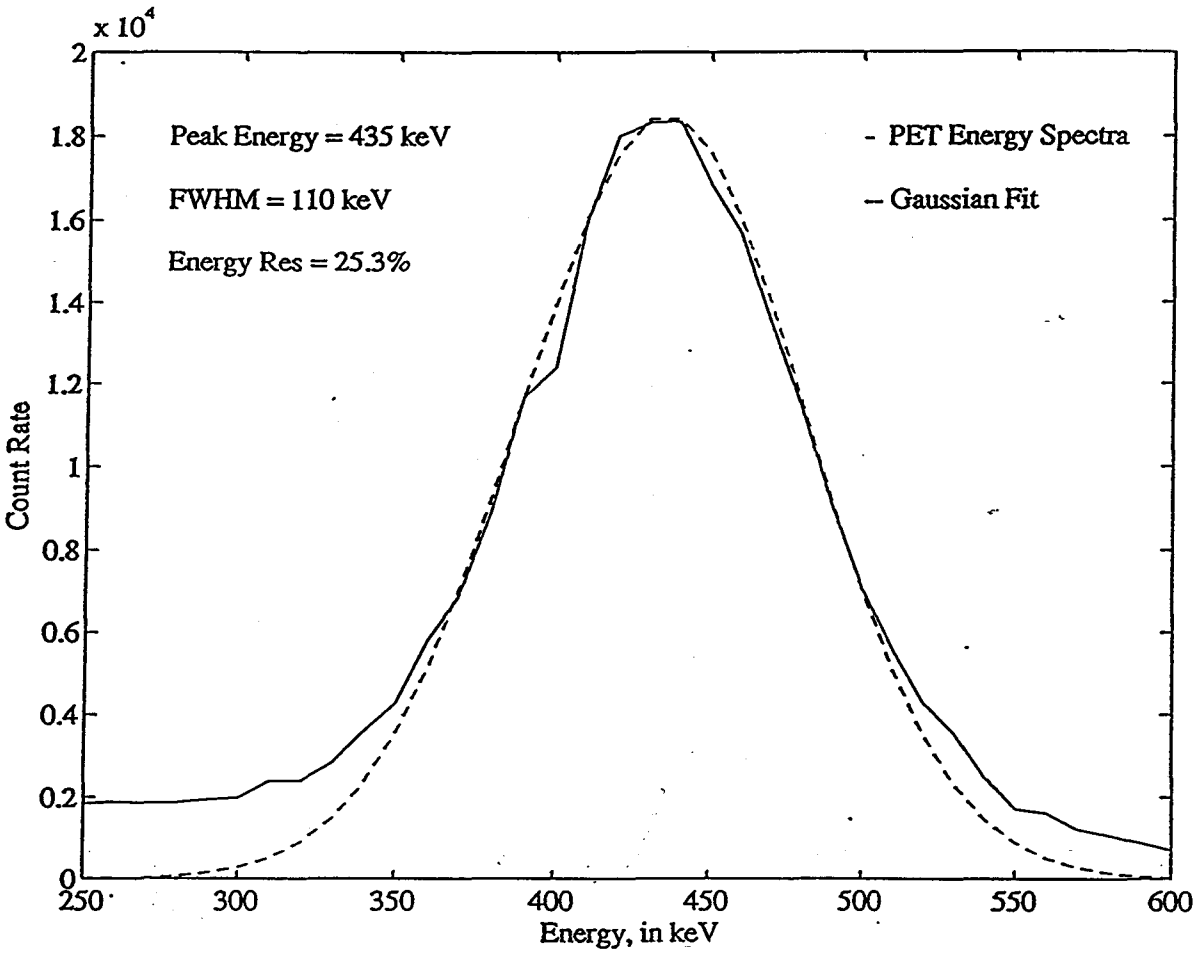

Figure 2.6 PET block energy spectra measured for a ^{18}F point source with no object in the scanner. Gaussian fit with listed parameters included. (Bowen 1994, p103)

Monte Carlo Simulations

In order to predict the response of the tomograph under various conditions a number of simulations must be performed. In this work, line and uniform phantoms that are of dimensions similar to those used experimentally have been studied.

Figure 2.7 shows a transaxial view of the tomograph simulated in this work, the ECAT 953/31 (CTI/Siemens). The axial length of the FOV is 108 mm, and the detector ring has a diameter of 760 mm. The scanner is comprised of two adjacent rings of BGO block detectors, giving a total of 16 rings that span the FOV. Each ring consists of 48 blocks (each 50 x 54 mm and 30 mm deep). The elements of the block form an 8 x 8 matrix of crystals with each element 6.22 x 6.75 mm. Septa are also shown; they are 1 mm thick and 77 mm in length when fully extended. In this work, five septa lengths are investigated for tomographic (2D) and volume (3D) acquisition: For each phantom, a simulation was performed with each of the five septa lengths chosen for this study. Simulations include fully extended (7.7 cm) and retracted (0 cm) septa, as well as septa at one-quarter (1.925 cm), half (3.85 cm) and three-quarters (5.775 cm) of the full length.

In traditional 2D acquisition, coincidence events are mapped into 31 transaxial planes. A total of 31 image planes (16 direct and 15 cross planes) are formed for a 16 detector ring tomograph. "Direct" planes are comprised from coincidences registered in the same detector ring (slice offset 0) or two crystal rings apart (slice offset 2).

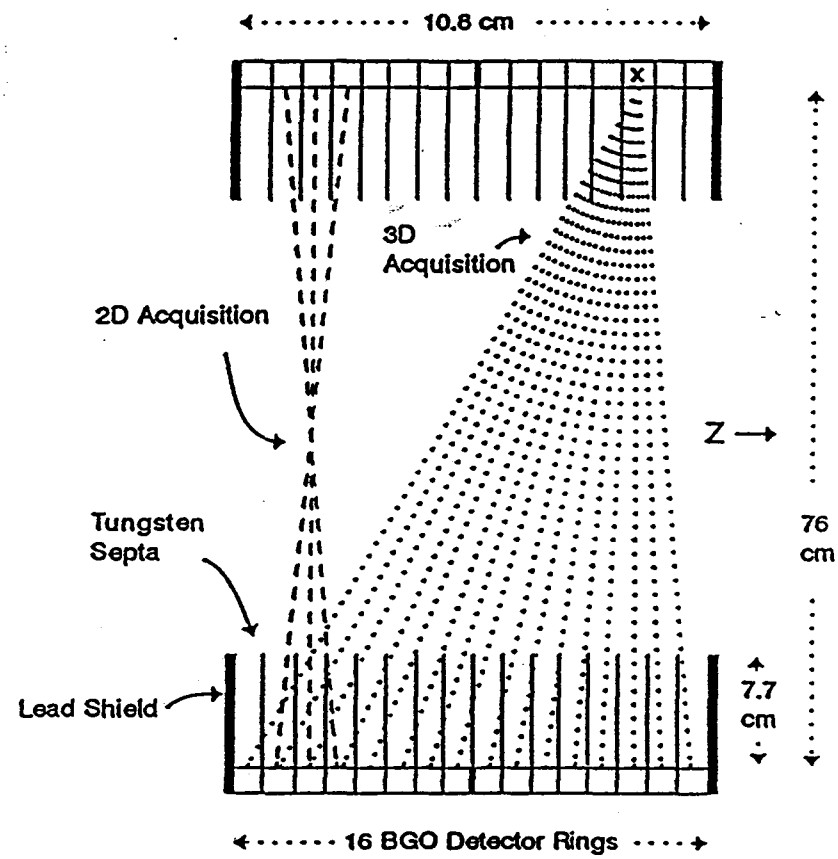

Figure 2.7 Trans-axial view of tomograph showing dimensions and the difference between 2D and 3D acquisition. Septa are also shown.

"Cross" planes have slice offsets of 1 and 3. The cross planes do not correspond to a physical ring, but are intercalated between direct planes. For this type of 2D acquisition, the mashing is of order 3. Figure 2.8 shows a cross sectional view of the tomograph gantry and the mashing used for 2D acquisition. In addition to the traditional 2D acquisition with a mashing of less than or equal to three (m=3), the effect of different mashing orders was also studied. The mashing orders included in this work are for m=1, 3, 5 and 7. The effect of septa on 3D acquisition is also presented.

In traditional 3D acquisition, the septa are removed and coincidences are accepted between any ring pair, resulting in total of 256 sinograms for a 16 ring tomograph.

As previously mentioned, there are 31 and 256 sinograms formed in 2D and 3D, respectively. The simulation results are presented as a sum of either 31 sinograms (2D) or 256 sinograms (3D). This will enable a comparison of overall sensitivity changes to be made.

A *uniform phantom* consists of a cylindrical water filled plexi-glass container. The uniform phantom simulated is 20 cm in diameter and length. A *line phantom* is one in which a line source of activity is placed in a cylindrical, water filled plexi-glass container. The line source may either be centered, or off centre. Two centered line phantoms are simulated. One has an axial length of 20 cm and the other an axial length

of 58 cm. The diameter of the container is 20 cm. Figure 2.9 shows a typical simulation setup.

The procedure for running a simulation is given in Appendix A.

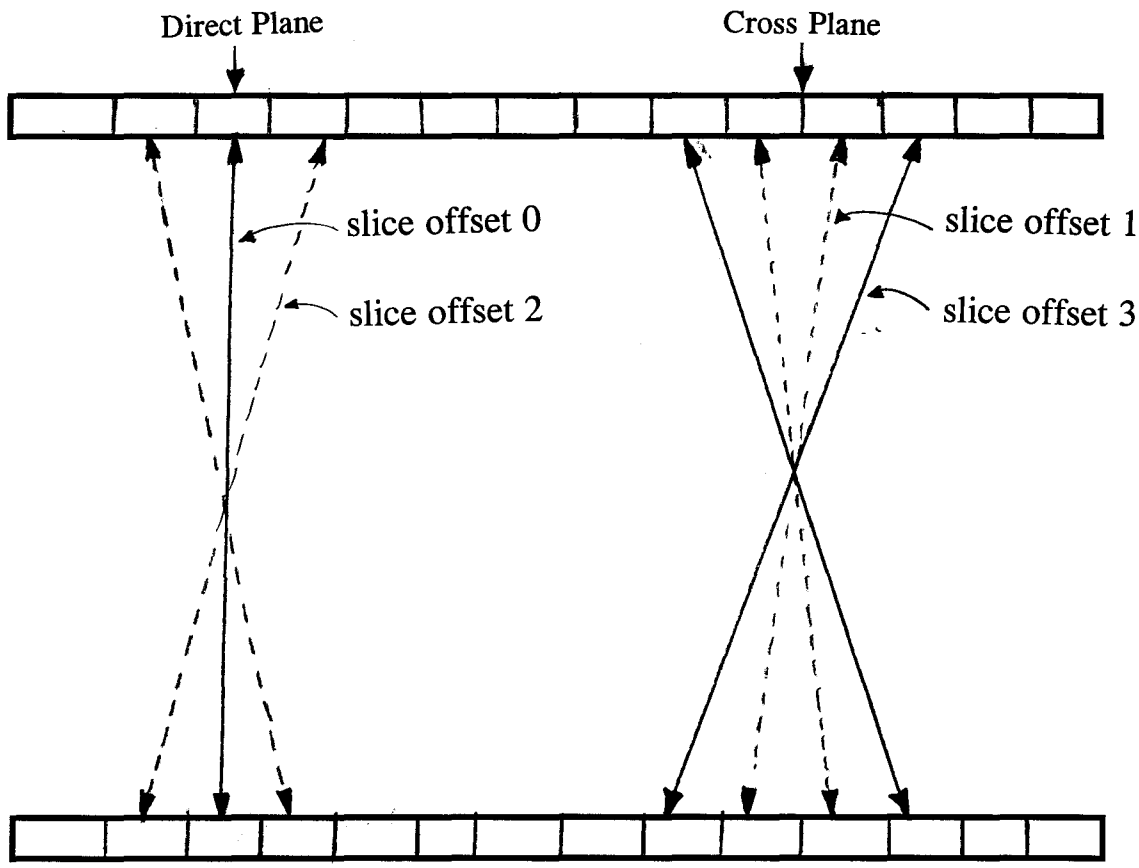

Figure 2.8 Cross section through the tomograph gantry showing the slice to plane mappings (mashing) used when operating in 2D mode. Direct planes (slice offset 0 and 2) and Cross planes (slice offset 1 and 3) are shown. The mashing order is 3.

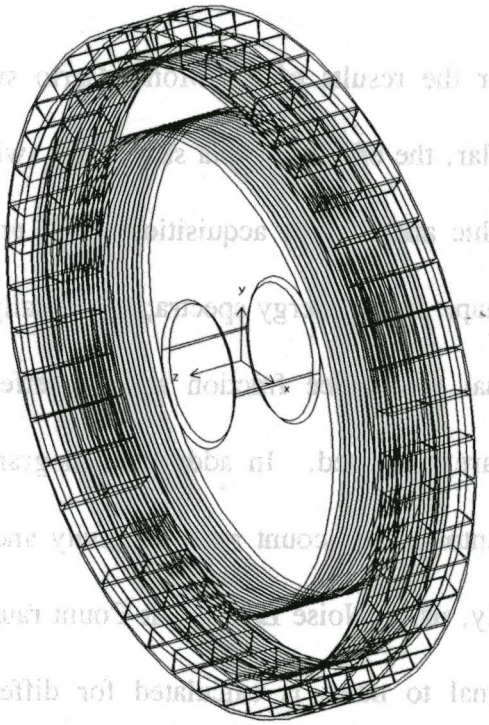

Figure 2.9 Geometry used to define the acquisition system. A detector ring is assembled from 48 BGO blocks. Septa are placed between the crystal rings and the phantom geometry and distribution are defined.

CHAPTER III

Monte Carlo Results and Discussion

In this chapter the results of the Monte Carlo simulations are provided and discussed. In particular, the effect of septa shadowing (with respect to septa length) is studied for tomographic and volume acquisition. The analysis includes the effect of septa length on the shape of the energy spectra; specifically the true and scatter counts, scatter fraction, signal acceptance fraction and the effect of septa on dual energy window acquisition are discussed. In addition, sinogram profiles are presented for uniform and line phantoms, and count rate sensitivity and resolution peak broadening are measured. Finally, using Noise Equivalent Count rate analysis, the effect of septa length on image signal to noise is calculated for different activity concentrations.

Coincidence Energy Spectra

For each valid coincidence, the energy of the photon in the pair that has lost the most energy is used in constructing the energy spectrum. Spectra for individual crystals, as well as for the entire detector block have been constructed. In each spectrum the events are classified as either true coincidences (neither photon has interacted in the medium of the phantom) or scatter coincidences (one or both of the photons have interacted with the medium of the phantom); the total spectrum is given by the sum of the "trues" spectrum and the single and multiple scattered spectrum.

Figures 3.1a and 3.1b shows typical spectra obtained for a uniform phantom with septa fully extended. The block energy spectrum (figure 3.1b) is well centered around 511 keV, as would be expected. However, the crystal energy spectrum (figure 3.1a) shows a second peak at approximately 250 keV. This energy does not correspond to the Compton edge (340 keV), but is demonstrative of the limits of position and energy encoding with finite size detectors. A significant portion of photons, approximately 20%, deposit 250 keV in a single crystal element and then either scatter within the detector block to another crystal or out of the block entirely. This effect has been previously studied by Thompson (1993). In practice, the energy of all the crystals in the block must be integrated before applying any energy discrimination or a significant portion of true events will be lost, decreasing the detection efficiency of the tomograph.

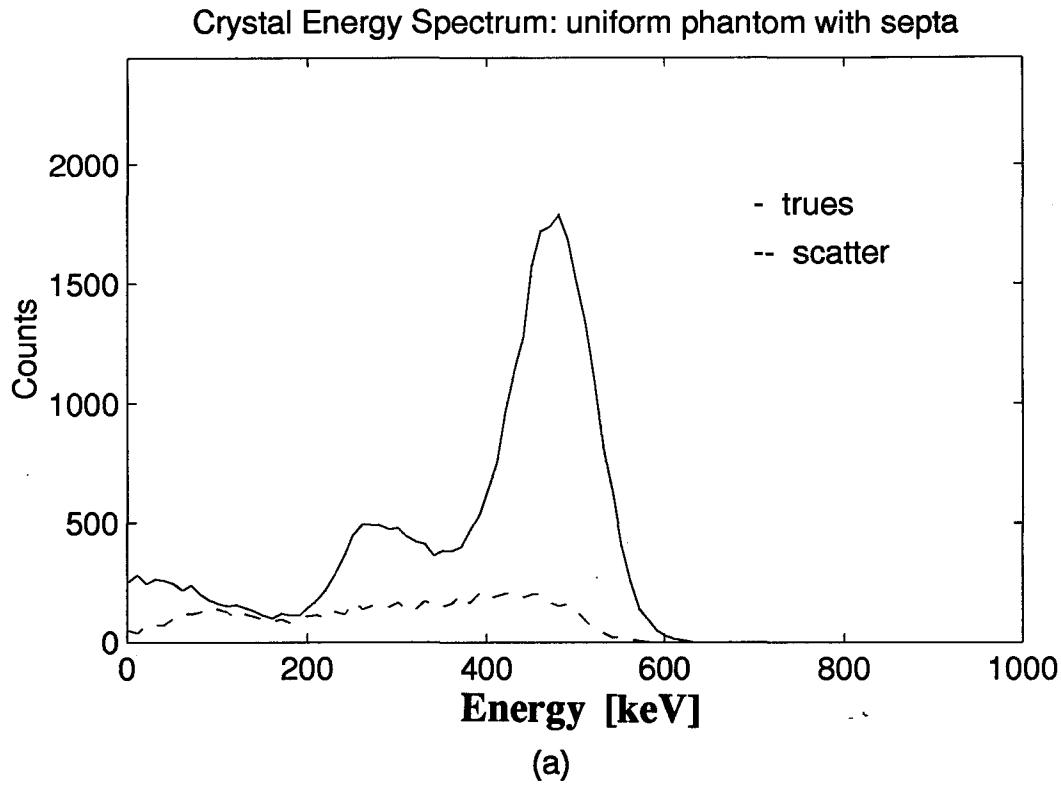

(a)

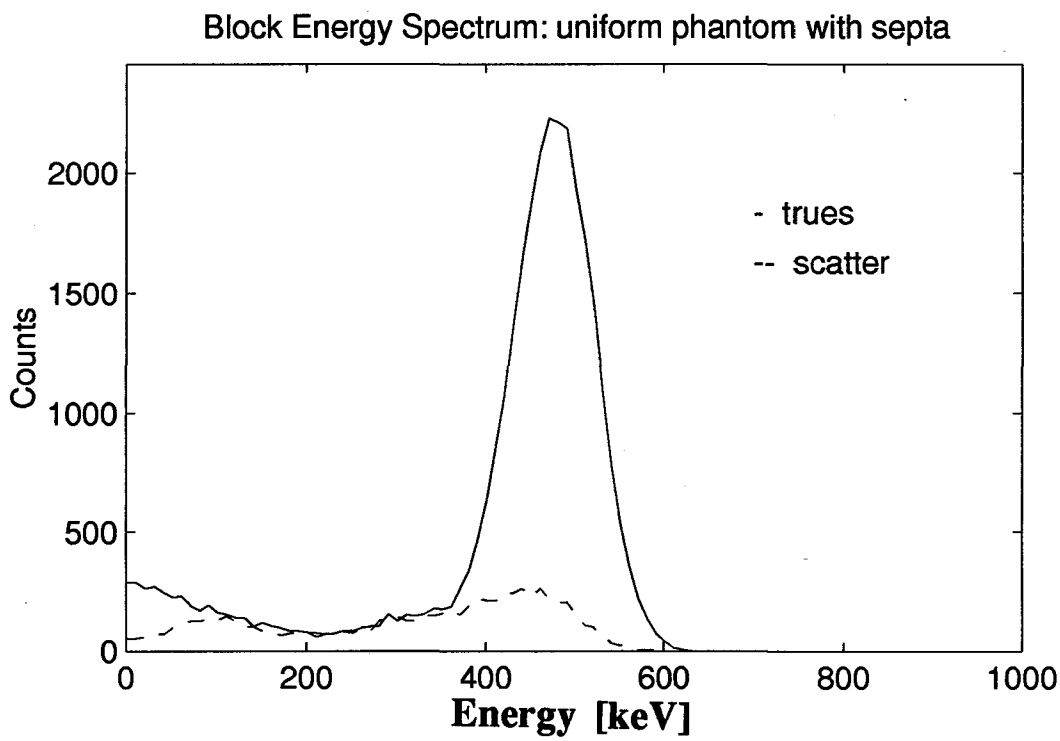

(b)

Figure 3.1 Energy spectra for true and scatter (object) coincidences for a uniform phantom acquired with septa (a) Crystal Energy Spectrum (b) Block Energy Spectrum.

The difference between any single crystal element and the entire detector block is dimensions. Hence, the individual crystal behaves like a small detector in comparison to the block and, therefore, will be less efficient at stopping photons (Knoll 1989). The peak at 250 keV is characteristic of the size of the individual crystals. This effect is analogous to the formation of single and double escape peaks in energy spectra when small, medium or large size detectors are used in gamma ray spectroscopy (Knoll 1989). In the limit, as the crystal becomes larger, the event in the peak at 250 keV shift into the photopeak: however, the increased efficiency of the crystals is accompanied by a loss of spatial resolution as a result of the larger crystal.

Figures 3.1c and 3.1d show the spectra obtained when the septa are fully removed. Note that there is a marked increase in sensitivity. If the counts in each spectrum are integrated, an increase of approximately 600% is observed, when comparing no septa with septa. However, this increase results mainly from a significantly greater number of scattered events in the spectrum. By integrating the scatter profile in each block spectrum and comparing the number of scattered events to the total number detected, the scatter component rises from 19% with septa, to 60% without septa.

Figures 3.2a through 3.2e shows the block energy spectra and Table 2 summarizes the changes in count rate sensitivity of the tomograph for the trues, scattered and total counts, without any energy thresholding for a uniform phantom with different septa lengths.

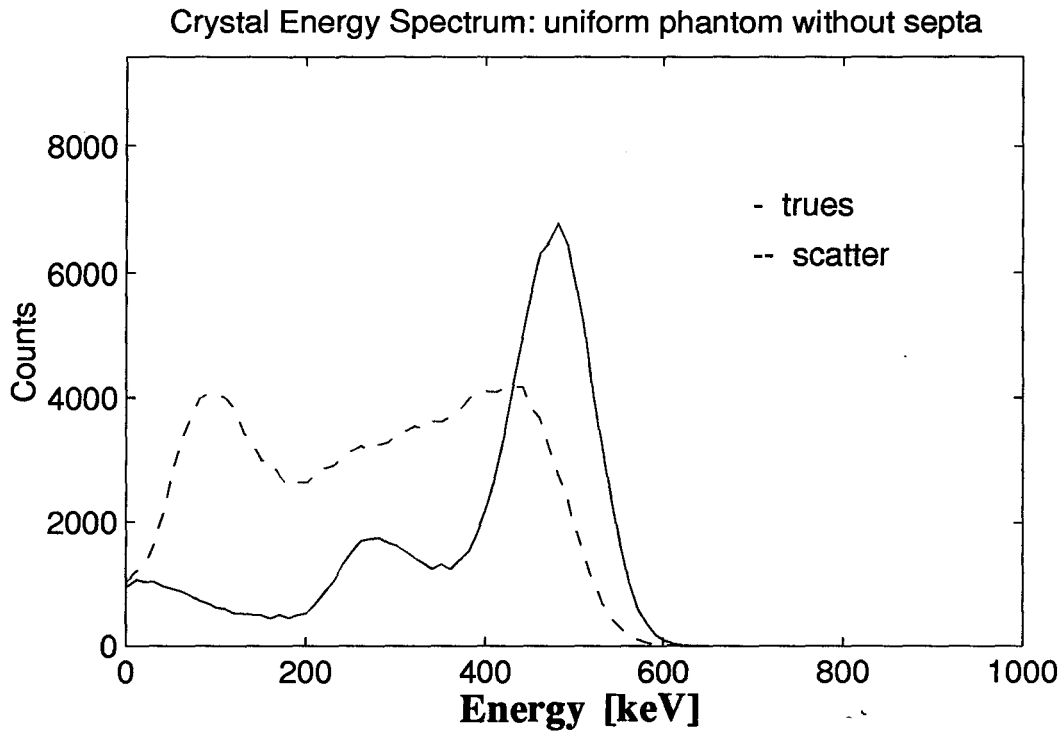

(c)

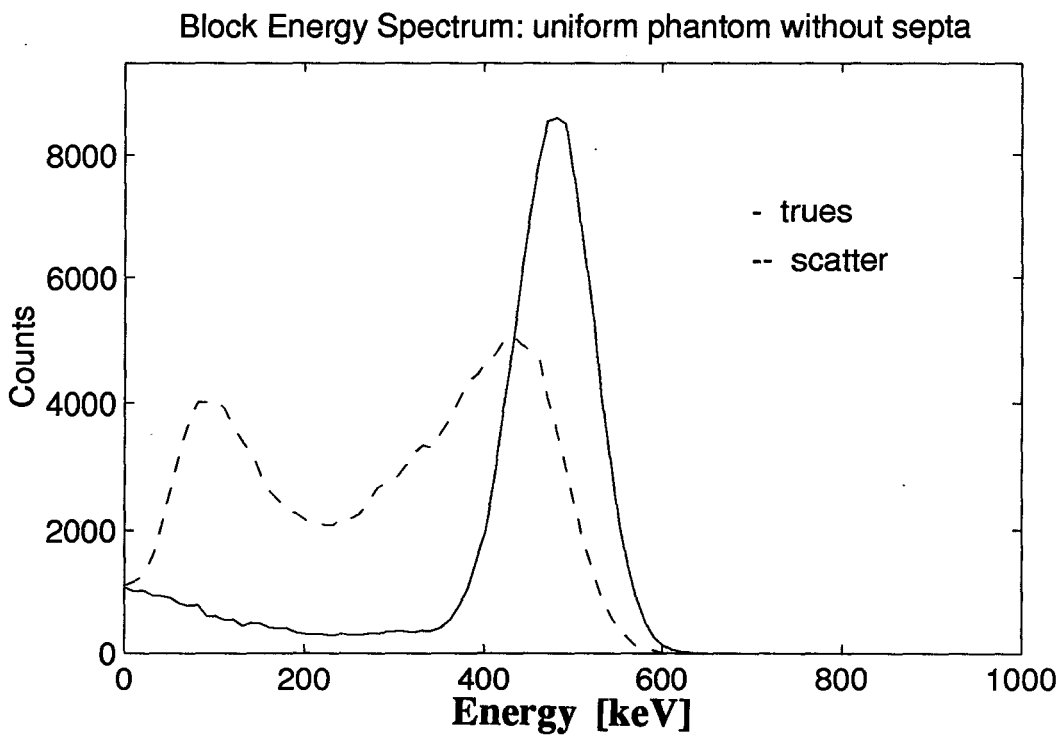

(d)

Figure 3.1 Energy spectra for true and scatter (object) coincidences for a uniform phantom acquired without septa (c) Crystal Energy Spectrum (d) Block Energy Spectrum.

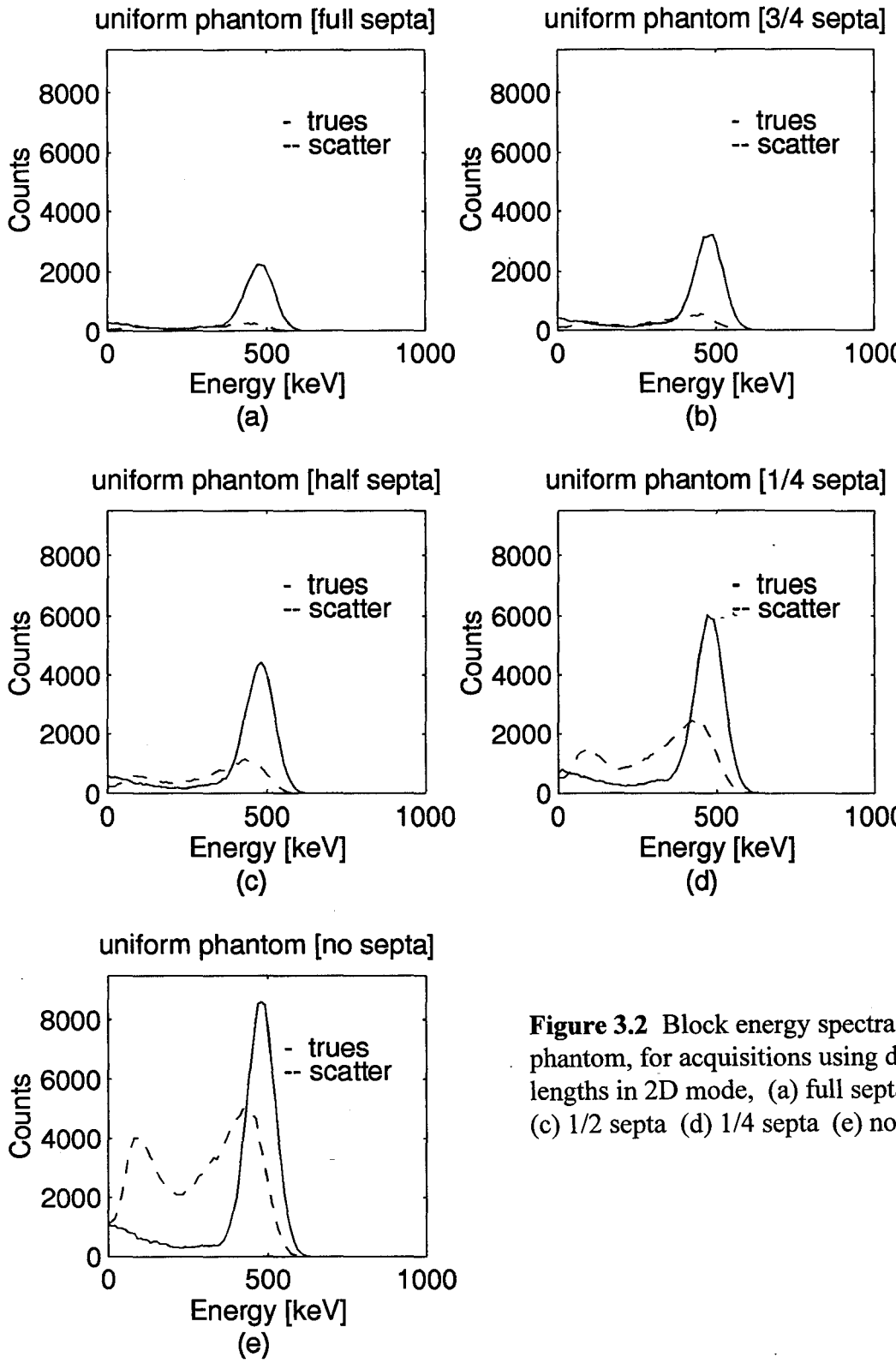

Figure 3.2 Block energy spectra for a uniform phantom, for acquisitions using different septa lengths in 2D mode, (a) full septa (b) 3/4 septa (c) 1/2 septa (d) 1/4 septa (e) no septa

The sensitivity is defined as the number of events (either true, scatter or total) detected (counts) for each septa length, normalized to the respective counts in the full septa position.

In general, the sensitivity of the tomograph to both scatter and true coincidences increases with decreasing septa length. However, there is a significant increase of sensitivity to scatter events. While the true events sensitivity increase by 269%, the scatter events increase by more than 2000%, when the septa are fully removed

TABLE 2

SENSITIVITY INCREASE WITH DECREASING SEPTA LENGTH

FOR UNIFORM PHANTOM (0 to 1000 keV ENERGY WINDOW)

septa position	**true**	**scatter**	**overall**	**scatter fraction**
full septa	1.00	1.00	1.00	0.19
3/4 septa	1.30	1.82	1.40	0.25
half septa	1.77	3.85	2.16	0.34
1/4 septa	3.44	9.05	3.69	0.47
no septa	3.69	22.78	7.32	0.60

Signal Acceptance Fraction and Signal Window

In practice, a number of coincidence events are rejected by energy thresholding to reduce the scatter component. This technique relies on the fact that Compton scattered photons have lost a portion of their energy and can be discriminated against during acquisition by applying an energy window. However, annihilation photons are forward scattered (figure 1.3), so that relatively large scattering angles result in relatively small energy losses. In addition, given that the energy resolution of BGO is approximately 20%, this technique cannot reject many of the scattered events.

In order to determine an optimum energy window, the fraction of true and scattered events accepted in any energy window must be considered. Using the energy spectra, a signal acceptance fraction has been calculated by scoring the number of true and scatter counts accepted above a specified energy threshold and dividing this by the total number of counts (true+scatter). Note that the signal (true acceptance) fraction and scatter acceptance fraction sum to 1.0 only for an energy threshold of 0 keV.

Figures 3.3a - 3.3e shows the acceptance fractions for a uniform phantom at different septa lengths. Note the marked increase of the scatter component in the total acceptance fraction as septa length decreases. This correlates with the sensitivity changes observed in the energy spectra (Table 2). Figures 3.3f - 3.3h show results from the simulation of the line phantom at three different septa lengths.

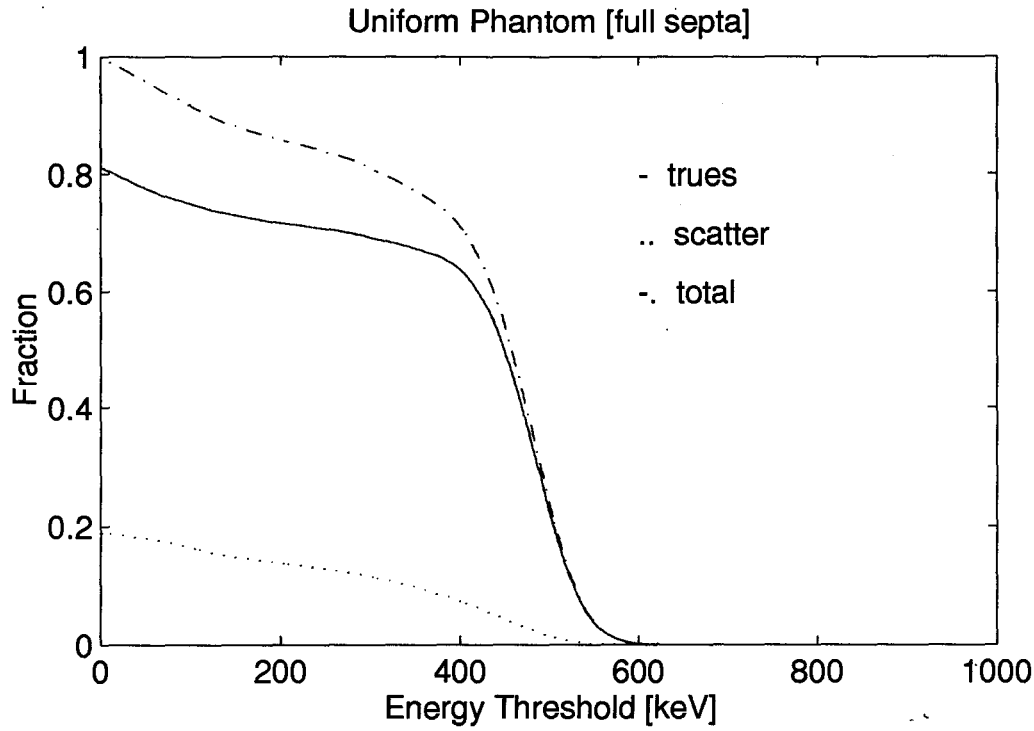

(a)

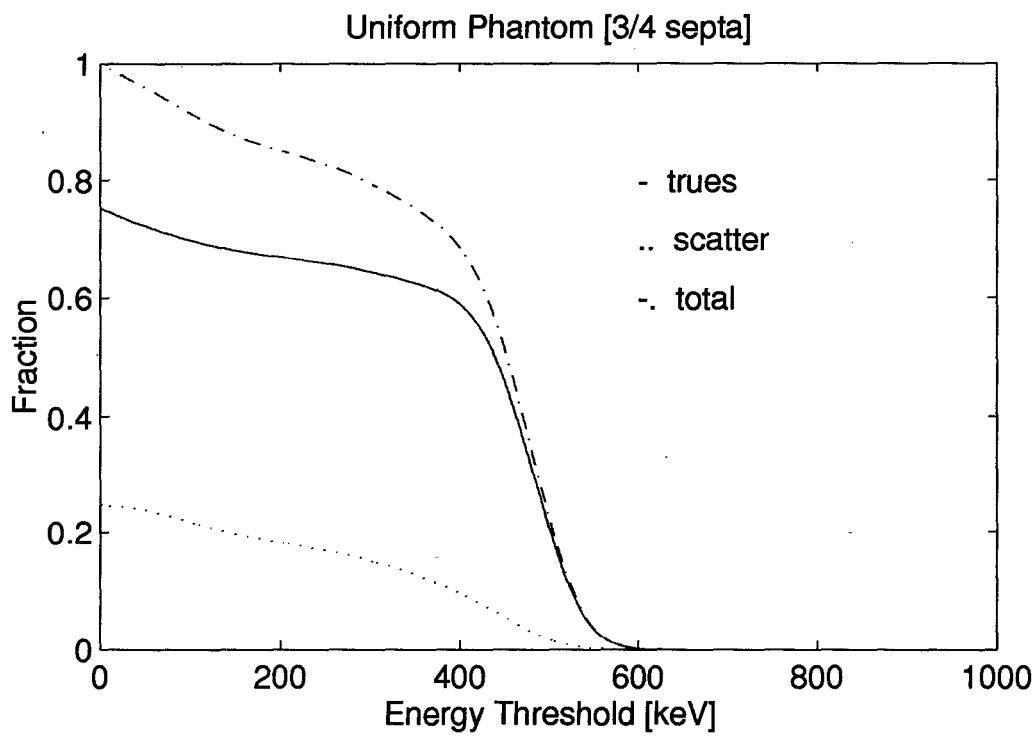

(b)

Figure 3.3 Signal Acceptance Fractions for acquisitions using different septa lengths in 2D mode, for a uniform phantom (a) full septa (b) 3/4 septa (c) 1/2 septa (d) 1/4 septa (e) no septa. Signal Acceptance Fractions for line phantom (f) full septa (g) 1/2 septa (h) no septa.

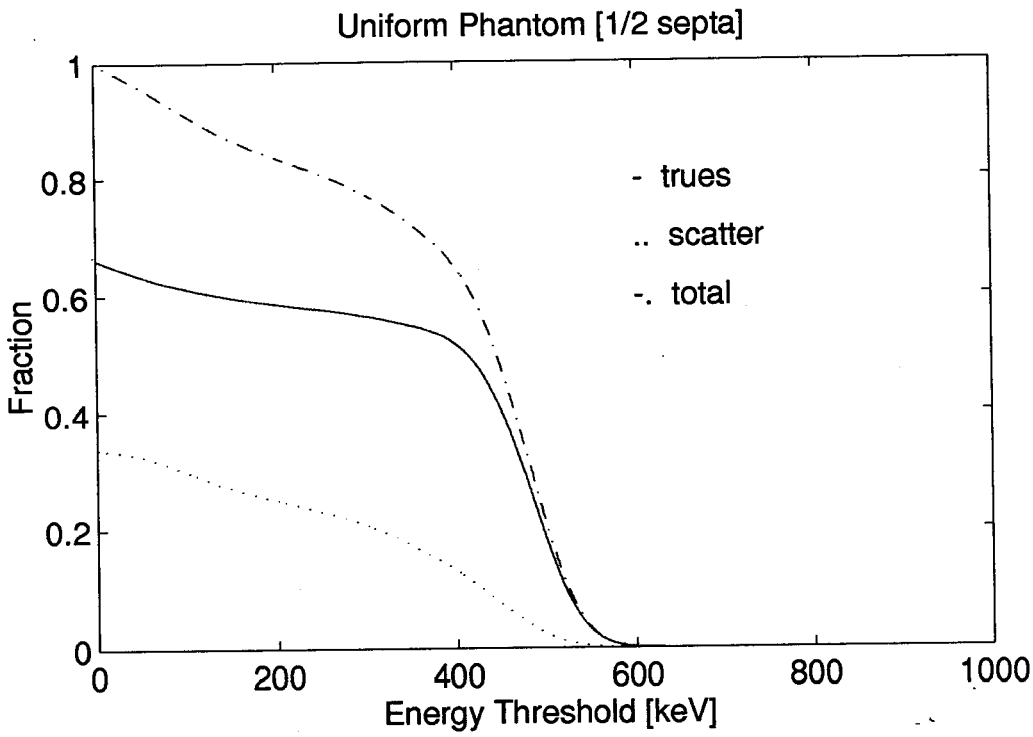
Uniform Phantom [1/2 septa]
- trues
.. scatter
-. total
Fraction
Energy Threshold [keV]
0
0.2
0.4
0.6
0.8
1
0
200
400
600
800
1000

(c)

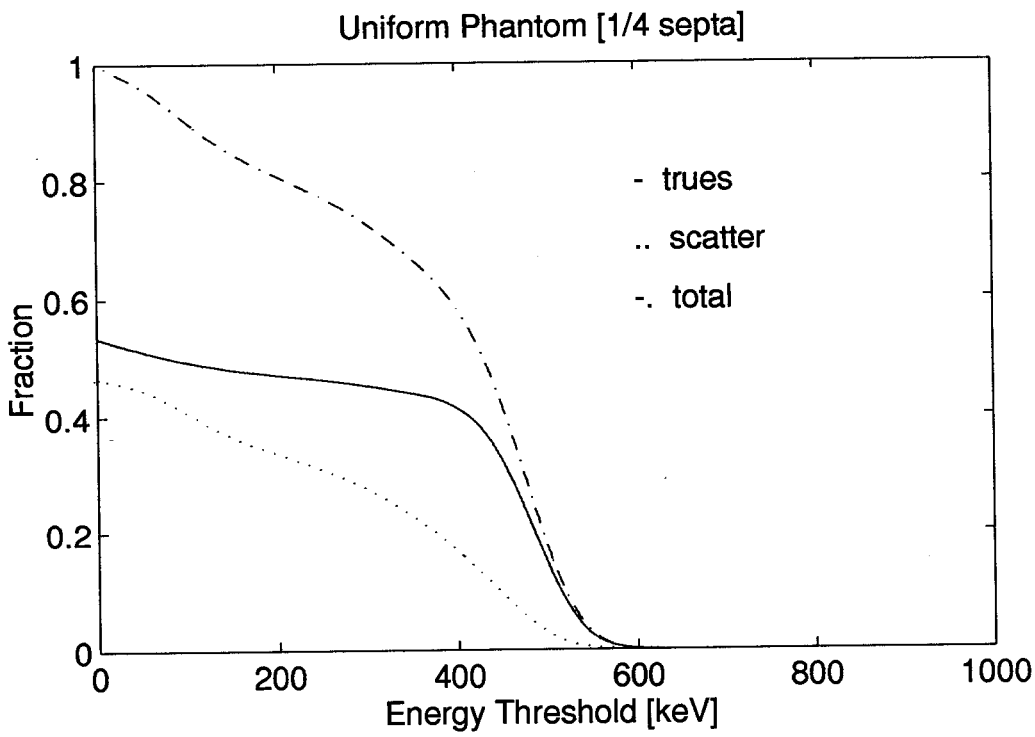
Uniform Phantom [1/4 septa]
- trues
.. scatter
-. total
Fraction
Energy Threshold [keV]
0
0.2
0.4
0.6
0.8
1
0
200
400
600
800
1000

(d)

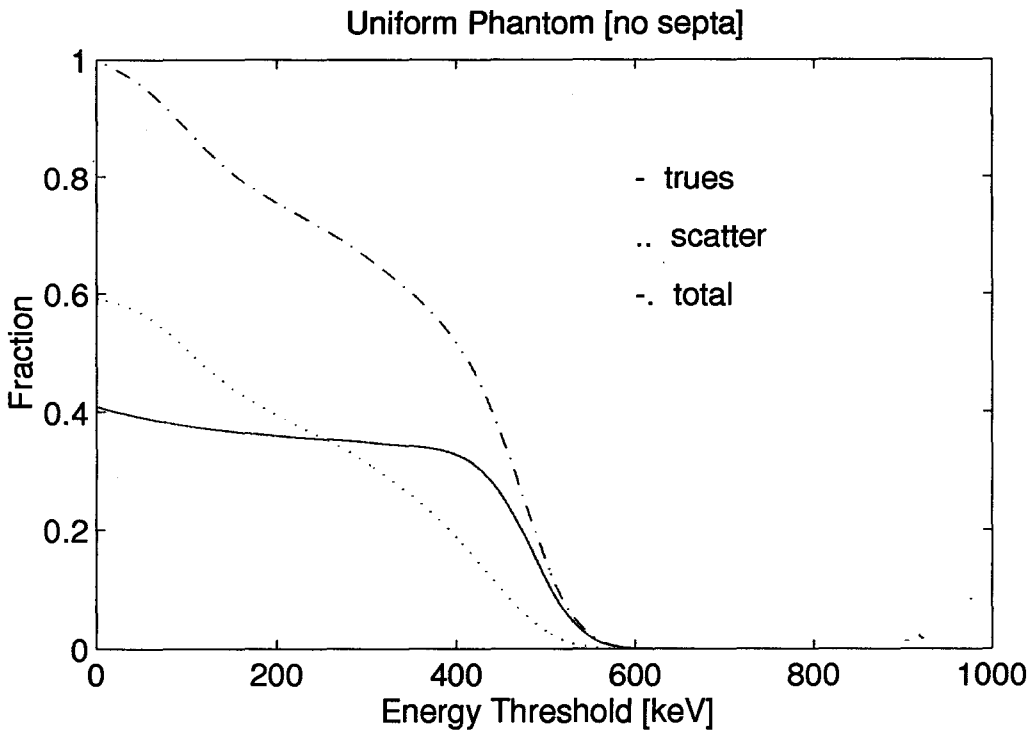
Uniform Phantom [no septa]
Fraction
Energy Threshold [keV]
- trues
.. scatter
-. total
0
0.2
0.4
0.6
0.8
1
0
200
400
600
800
1000

(e)

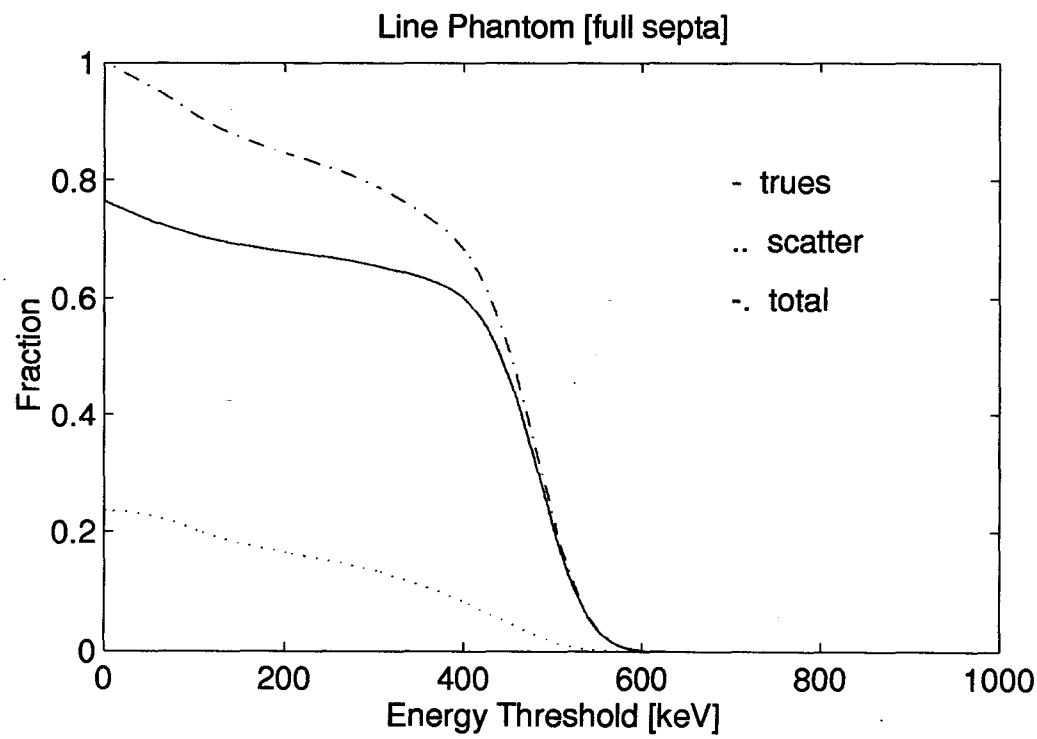
Line Phantom [full septa]
Fraction
Energy Threshold [keV]
- trues
.. scatter
-. total
0
0.2
0.4
0.6
0.8
1
0
200
400
600
800
1000

(f)

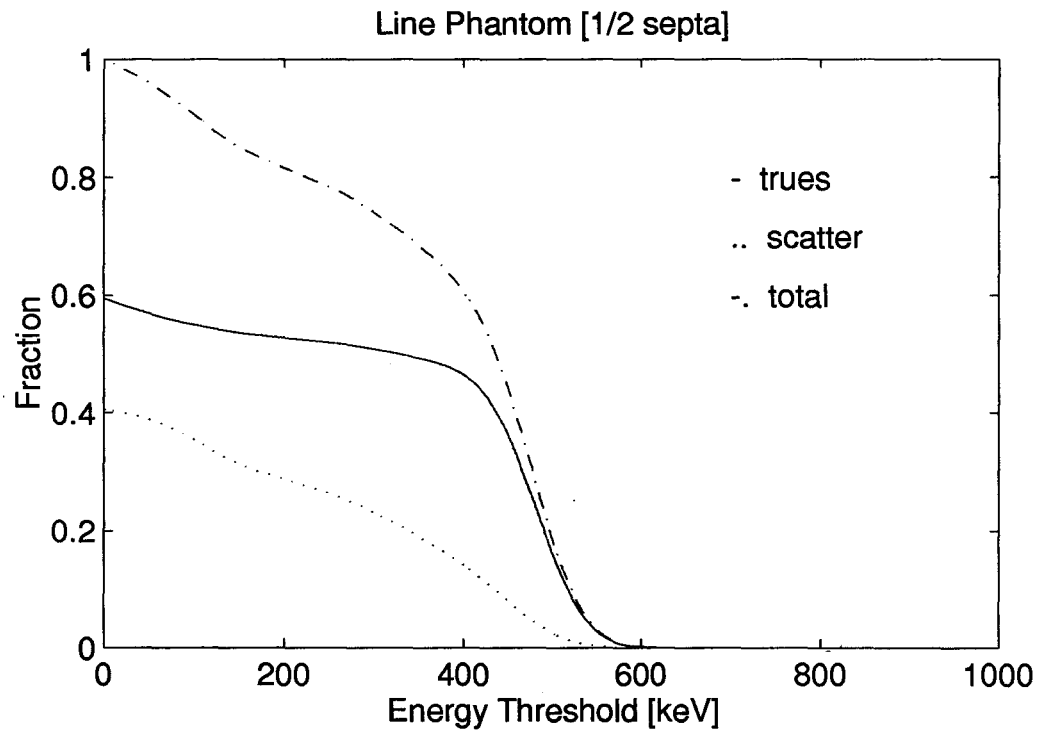
Line Phantom [1/2 septa]
Fraction
Energy Threshold [keV]
- trues
.. scatter
-. total
0
0.2
0.4
0.6
0.8
1
0
200
400
600
800
1000

(g)

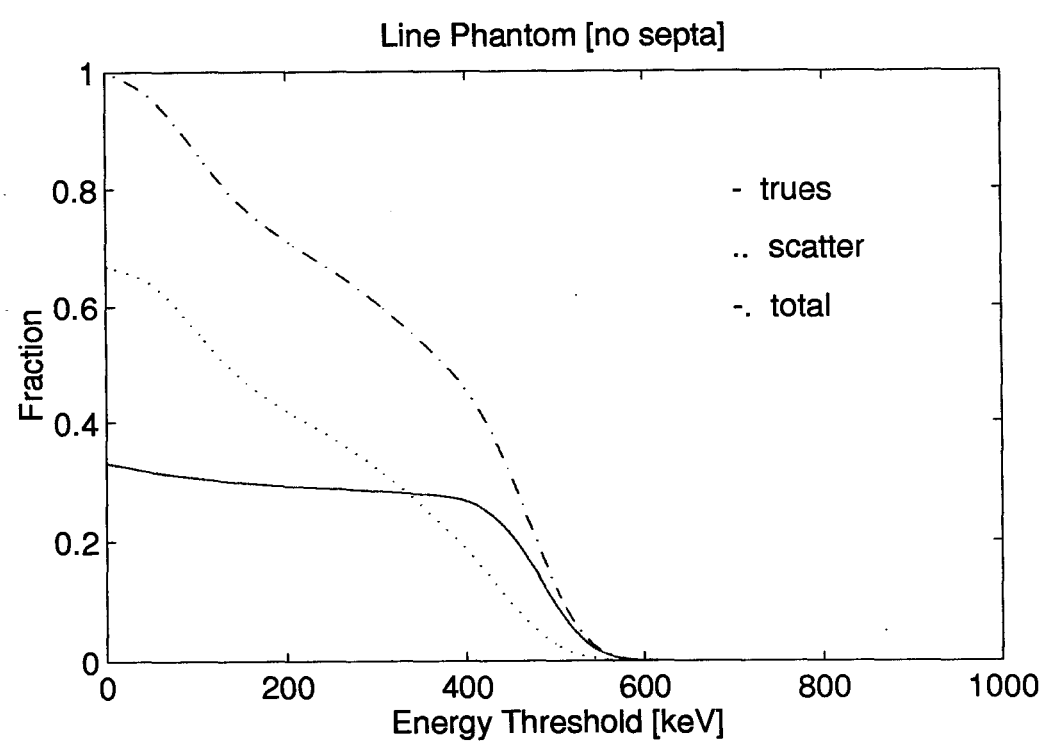
Line Phantom [no septa]
Fraction
Energy Threshold [keV]
- trues
.. scatter
-. total
0
0.2
0.4
0.6
0.8
1
0
200
400
600
800
1000

(h)

All the curves shown in figures 3.3 (both for uniform and line phantom) show a steep drop of the true and total signal acceptance fractions above a threshold energy of 380 keV, so that a signal window of 380 - 650 keV for all septa configurations is appropriate.

Scatter Fraction

Of particular concern in PET are scatter coincidences since, to date, no method has been developed that can adequately compensate for scattered radiation.

The scatter fraction is defined as:

$$SF = \frac{scatter}{true + scatter} \tag{3.1}$$

It varies with energy threshold and therefore must be considered, in addition to the signal acceptance fraction, in determining an appropriate signal window. Figures 3.4a and 3.4b show the scatter fraction plotted against energy threshold for both the uniform and line phantom. Configurations with fully extended septa limit the SF to less than 20%. However, when the septa are fully removed, the scatter fraction can be higher than 50%. Based on figure 3.4, a lower threshold of 380 keV will limit the SF

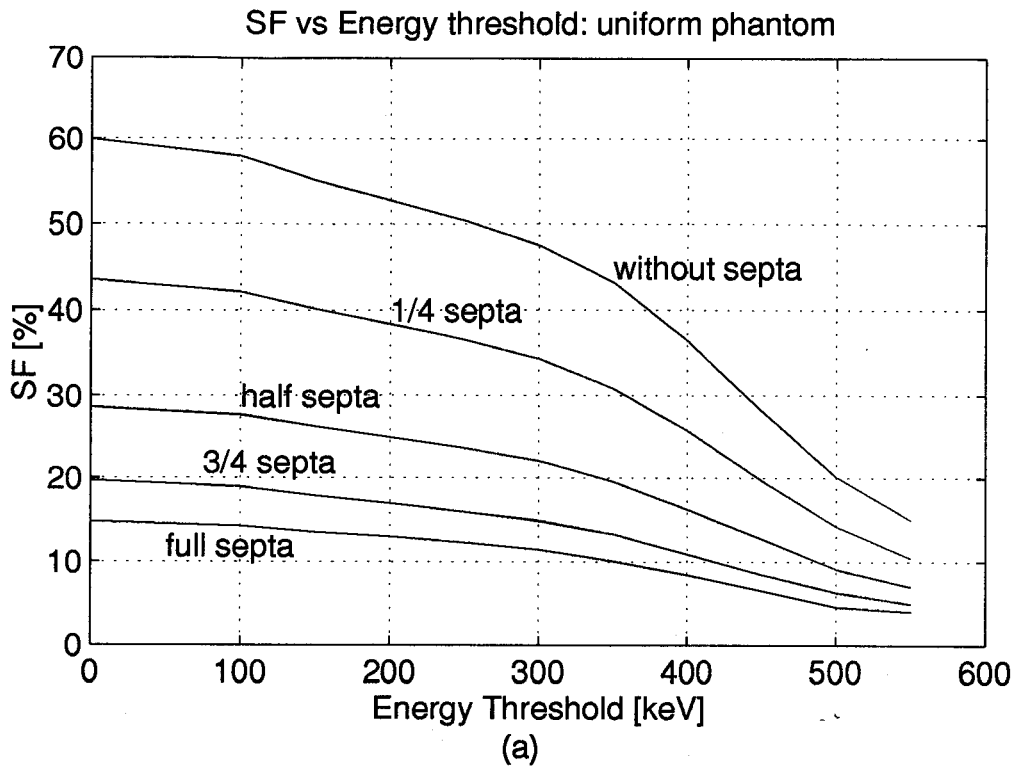

(a)

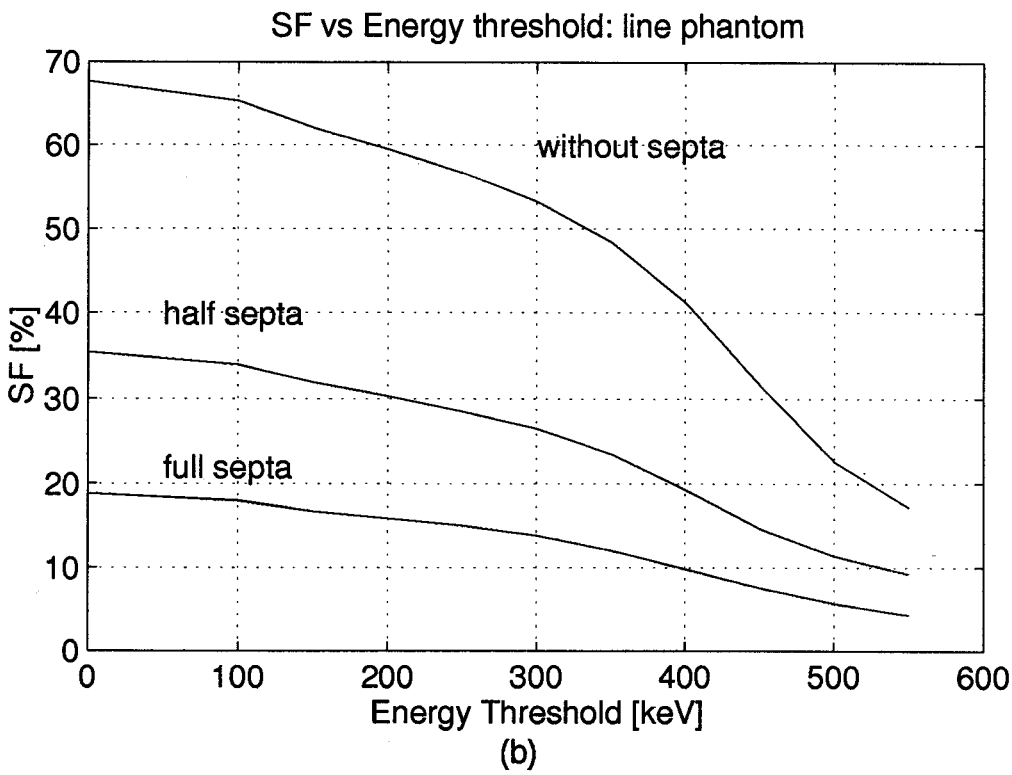

(b)

Figure 3.4 Scatter Fraction vs. Energy threshold for (a) uniform phantom (b) line phantom with different septa lengths (c) the ratio of the SF with respect to full septa remains relatively constant as a function of energy.

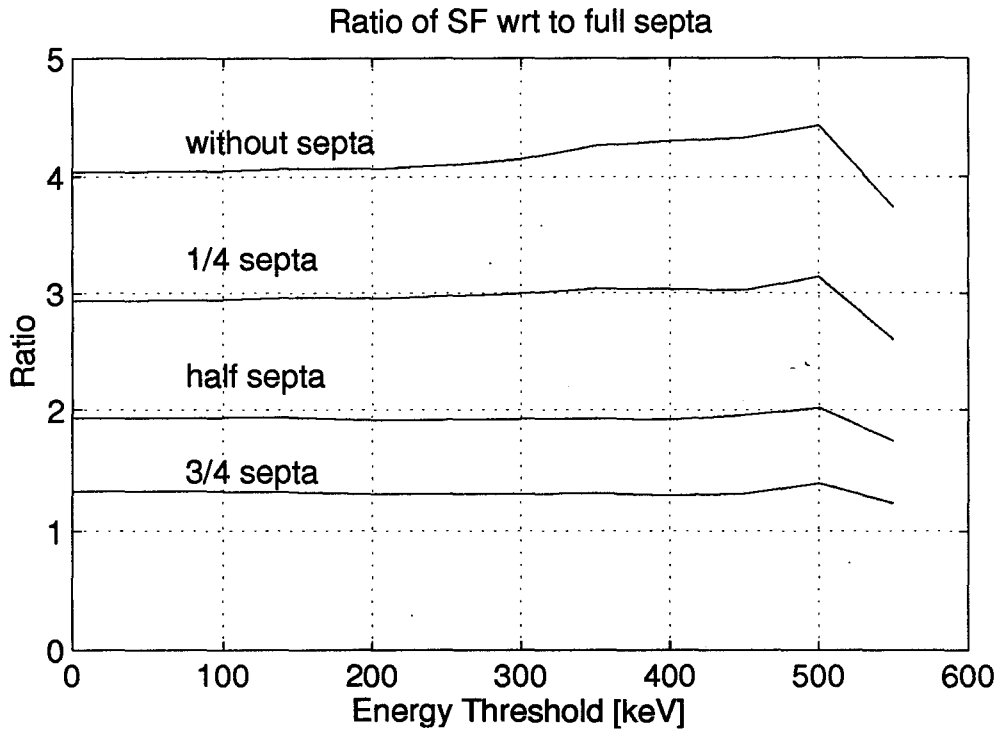

Figure 3.4 (c) the ratio of the SF with respect to full septa remains relatively constant as a function of energy.

to less than 50% for configurations without septa. A 380 keV threshold is also consistent with the energy threshold determined from the signal acceptance fraction.

Using data from figure 3.4a, the ratio of the scatter fraction for each septa length, with respect to full septa, was calculated at each threshold energy. The result is shown in figure 3.4c. The individual ratios remain relatively constant over the entire energy range of interest. There is some fluctuation at high energies, beyond 400 keV. This is indicative that the shape of the scatter profile does not change with septa length i.e. the septa affect equally photons that have scattered through a small or large angle. Hence, septa do not preferentially remove large angle scatter.

A Note on Dual Energy Window Scatter Correction

A common scatter compensation technique used in PET is the Dual Energy Window Scatter Correction (DEWSC) technique developed by Grootoonk *et al* (1993) described in Chapter I. Using the energy spectra generated from the Monte Carlo simulations, the DEWSC technique was evaluated. It was found to correct accurately the simulated data for all the septa configurations. Results for the uniform phantom are presented in Table 3. The ratio of the scatter to true events in each acquisition window was determined from the Monte Carlo data and therefore are the "ideal" or optimum values. The DEWSC method was determined to be valid for any septa length configuration. In general, the technique is sensitive to the accuracy to which the scatter

and true contributions can be determined in each acquisition window and therefore, the accuracy of the experimentally determined ratios will vary with septa length.

TABLE 3

EVALUATION OF DEWSC FOR UNIFORM PHANTOM

total number of events

septa length	Compton window	photopeak window	Rs	Ru	calculated trues	Monte Carlo trues
full	17569	25412	2.44	0.51	23031	23031
3/4	30940	29262	3.26	0.76	25755	25755
1/2	58163	34968	4.06	1.14	28741	28741
1/4	114261	44684	4.91	1.64	32165	32165
none	245577	69281	5.82	2.06	41972	41967

Comparison of True and Scattered Counts with Respect to Septa Length

Figures 3.5a and 3.5b summarize the changes in sensitivity, scatter fraction and the variation with mashing for the simulations of the uniform phantom, using both 2D and 3D acquisition and a signal window of 380 - 650 keV.

Figure 3.5a shows a plot of the scatter versus true sensitivity. Curves A through D represent mashings of 1, 3, 5 and 7, respectively, used in the 2D acquisition. Curve E shows the results for 3D acquisition. The points (open circles) on each curve are used to indicate the septa length simulated in the acquisition. The sensitivity scale is normalized to the leftmost point on curve B, i.e. traditional 2D acquisition with full septa (mash=3). This figure shows that the trues sensitivity will increase by a factor of approximately 4.5, when going from traditional 2D to 3D acquisition. It is worth mentioning that the scatter sensitivity will also increase, by a factor 30.

In general, the flattest curve is the most desirable since this will indicate an increase in trues sensitivity with the least gain in scatter. As the mashing order increases beyond 3 (curves C and D), the curves tend to flatten slightly and better approximate the shape of curve E (3D). This is consistent with the notion that 3D acquisition is the limiting case of 2D with a mashing order of 15 (for a 16 ring tomograph), as far as the total number of counts is concerned. In terms of sensitivity, 3D acquisition with quarter length septa or greater, out performs all possible 2D acquisitions. All the curves have a similar shape, so that a change in mashing will predominately only effect the tomographs sensitivity, this is better illustrated in figure 3.5b.

Figure 3.5b is similar to 3.5a, however, the raw number of true and scatter counts are plotted for each mashing order, with respect to septa length. In addition,

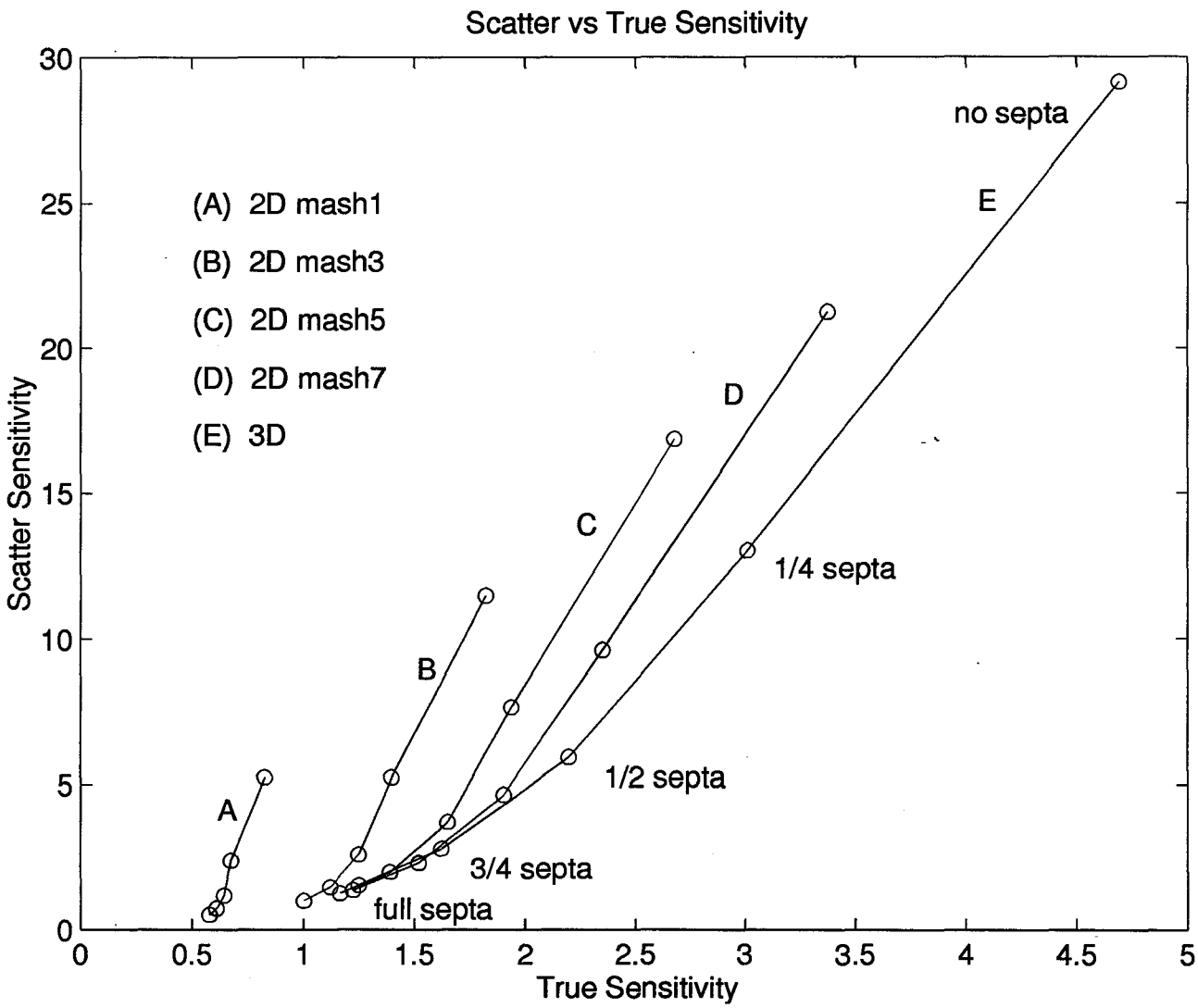

Figure 3.5a Summary of changes in sensitivity, and variation with mashing for 2D and 3D acquisition, for a simulated uniform phantom and an acquisition window of 380 - 650 keV.

scatter fraction (SF) lines are plotted for 10, 20, 30, 40 and 50% SF. Hence, any points lying on these lines have the same scatter fraction (but a different number of total counts). Isosensitivity lines for overall sensitivity (true+scatter) are also shown. The isosensitivity lines are normalized to the total count of the leftmost point in curve B, i.e. traditional 2D acquisition with full septa. The implications from this figure are quite interesting.

As with figure 3.5a, a flatter curve indicates better performance with respect to true and scatter counts. Comparing traditional 2D and 3D acquisition, we observe that there is an increase of overall sensitivity by a factor of 7.0 with a corresponding increase in scatter fraction from 10% to 40%. However, 3.5b shows that the trues sensitivity has increased only by a factor of 4.5. In addition, 3D acquisition with a septa length of a quarter or more outperforms any 2D acquisition at the same septa length (as was seen in figure 3.5a). It is important to observe that the corresponding septa length points (open circles), for each acquisition, lie along the same SF line, indicating that with respect to mashing, septa only effect the sensitivity of the tomograph.

As mentioned previously, with respect to the number of counts, 3D acquisition is a limiting case of 2D acquisition with a mashing of order of 15. However, there is a fundamental difference with respect to image reconstruction since 3D acquisition implies a reconstruction of a 3D projection data set. Hence, operating in 3D mode with full septa will not allow accurate reconstruction since the counts will be

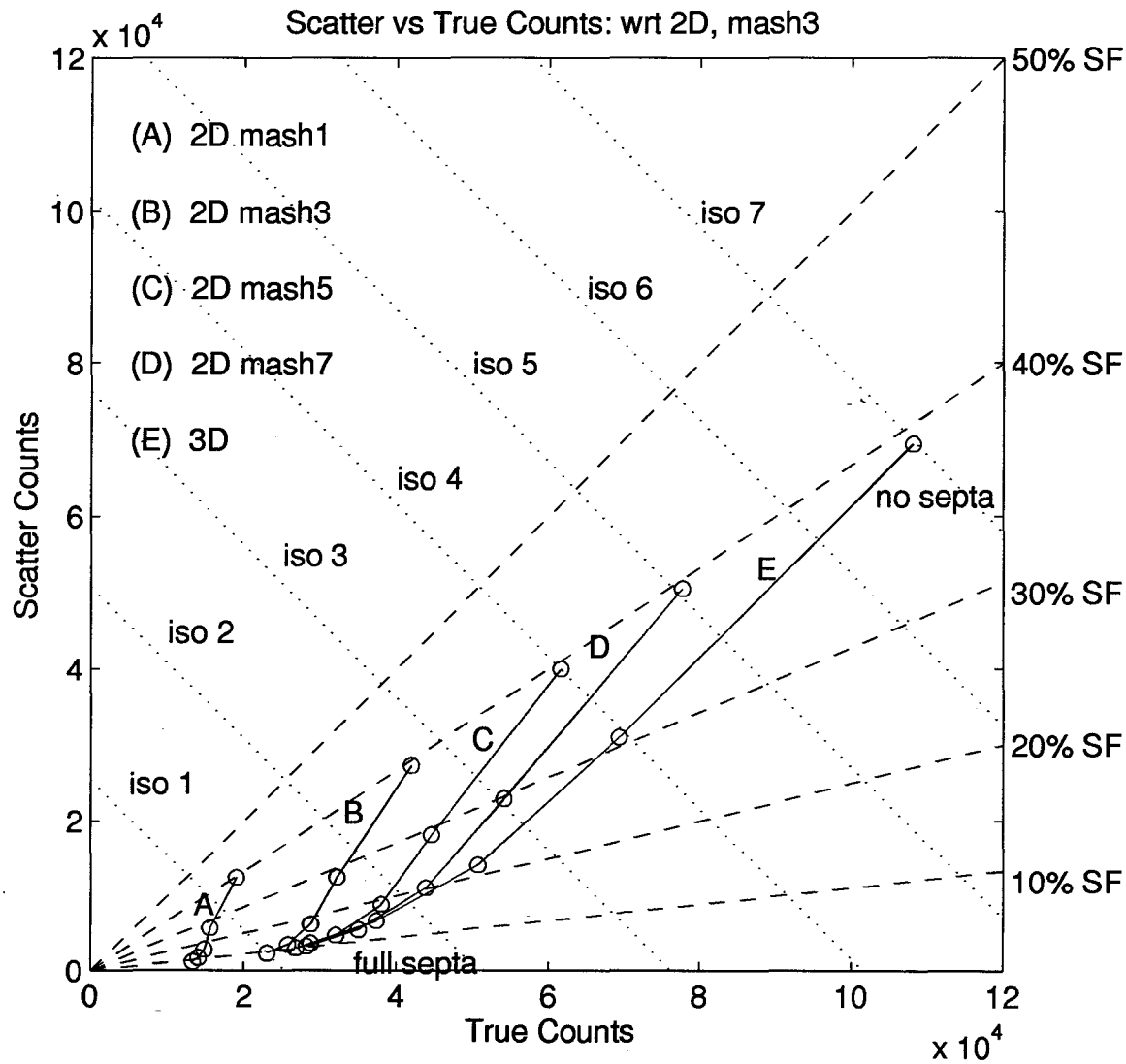

Figure 3.5b Summary of changes in true and scatter counts, overall sensitivity, scatter fraction and variation with mashing for 2D and 3D acquisition, for a simulated uniform phantom and an acquisition window of 380 - 650 keV.

distributed amongst 256 sinograms, as opposed to 31 sinograms in 2D acquisition. The overall count sensitivity increase of 2 (only 1.25 for trues) will not be sufficient to compensate for the large degradation of statistics if 3D reconstruction is used. However, techniques like single and multi-slice rebinning, in which the 3D data is reorganized into a 2D data set, may realize some benefit from increased sensitivity with no increase in scatter (Daube-Witherspoon and Muehllehner 1987, Lewitt and Muehllehner 1991).

When the distribution of the septa length markers (open circles) along each curve are examined, one observes that small (short) septa have more influence than large (long) septa. This effect can readily be observed when one compares the difference in true counts between quarter length and no septa as opposed to full and three-quarter length septa. Figure 3.5c shows a cross sectional view of the tomograph for which lines, connecting a source and the edge of each detector are drawn. These lines may or may not pass through the septa, and indicate the number of detectors "visible" to the source for each septa length. Figure 3.5d plots the number of "visible" detectors for each septa length, for a source at the centre of and the edge of the FOV. The curve is not linear and falls with a behaviour like 1/x as septa length increases. This behaviour explains the sharp increases in sensitivity observed with decreased septa length since there are many more detectors that are in the "line of sight" and hence, a greater number of possible LOR's.

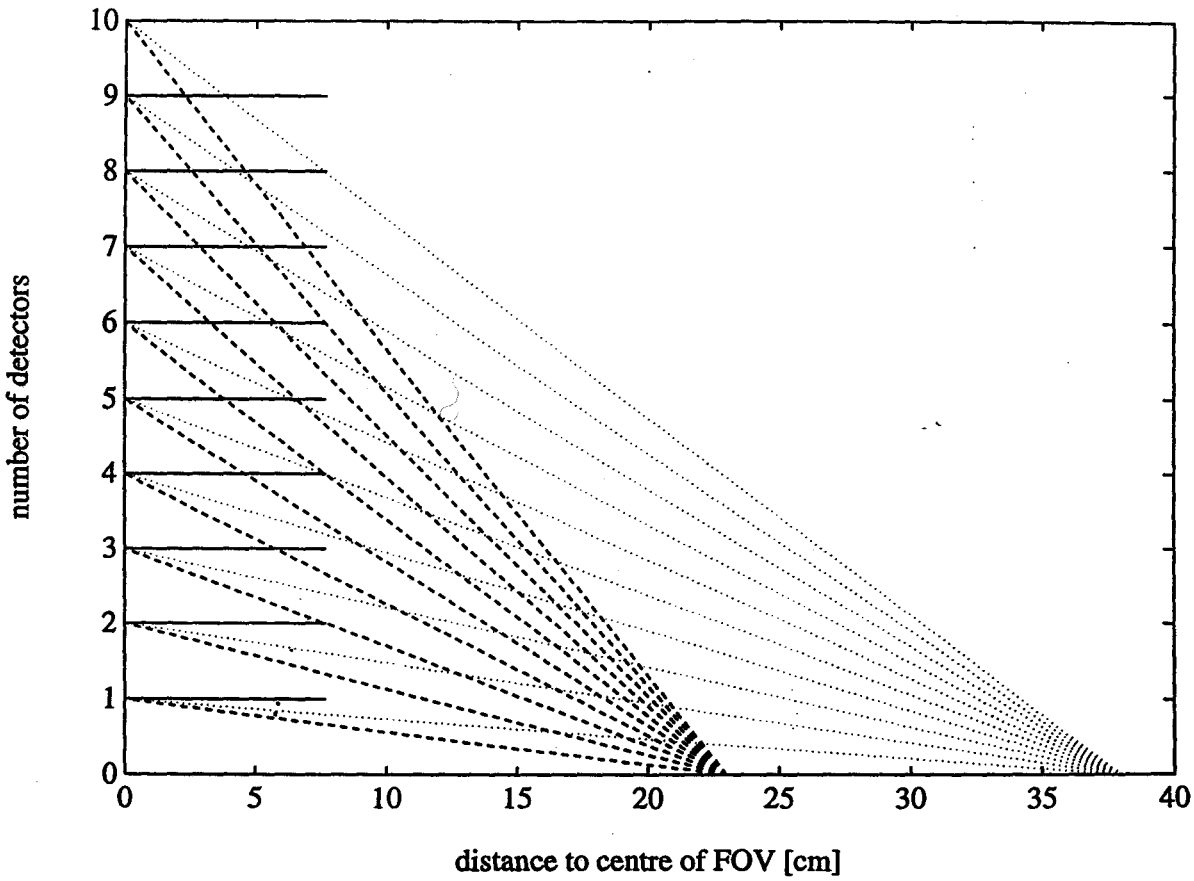

Figure 3.5c Trans-axial view of tomograph showing lines connecting the a source at the centre of the FOV (38 cm) and edge of the FOV (28 cm) to the detectors. The lines indicate the number of "visible" detectors to the source.

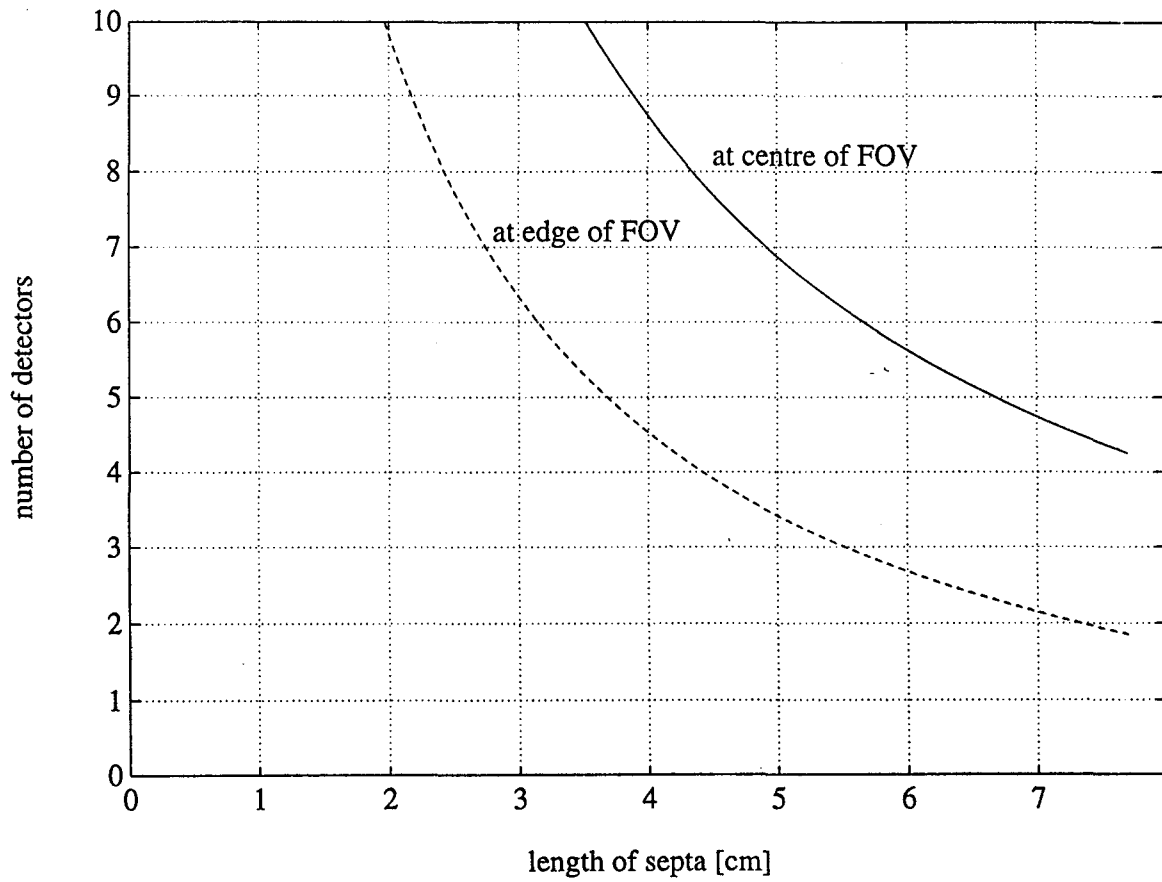

Figure 3.5d Plot of the number of "visible" detectors as a function of septa length. Note the behaviour of the curve for increasing septa length. The number of "visible" detectors falls of quickly for increasing septa length.

Sinogram Profiles

The statistics required for image formation would require simulation of a number of events far exceeding practical time limitations, due to limited computing resources. Although Monte Carlo simulations take too long to generate sufficient data from which images can be reconstructed, sinogram profiles are nonetheless valuable in observing the variation of the true and scattered components along with variation of spatial resolution under different configurations.

Energy spectra yield the distribution of events with respect to energy, whereas the sinogram profiles yield the spatial distribution of these events.

Sinogram profiles for both uniform and line sources are presented in order to observe the effect of septa length on spatial resolution. Since cylindrically symmetric phantoms were simulated, all projection angles in the sinogram can be summed together to improve the statistics. Essentially, the sinogram matrix (r,θ) has been collapsed, removing the θ dimension.

The profiles for the uniform phantom are given in figures 3.6a - 3.6e. The sensitivity changes that were observed, with respect to septa length, in the energy spectra are also apparent in these profiles. The profiles for the centered line source are given in figures 3.7a - 3.7c.

All the profiles have two distinct regions. The scattered component is characterized by a broad tail on top of which the trues component rides.

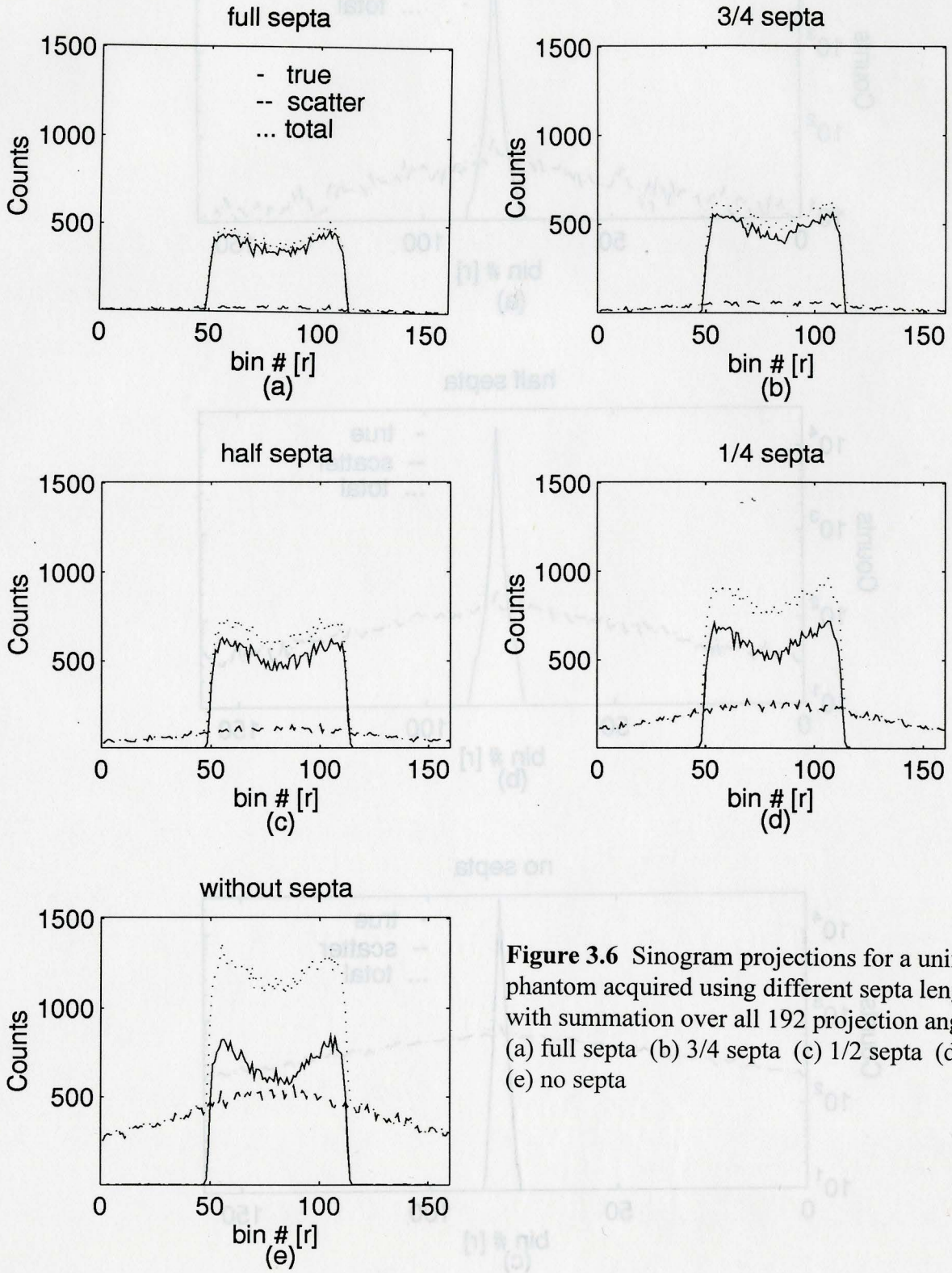

Figure 3.6 Sinogram projections for a uniform phantom acquired using different septa lengths, with summation over all 192 projection angles (a) full septa (b) 3/4 septa (c) 1/2 septa (d) 1/4 septa (e) no septa

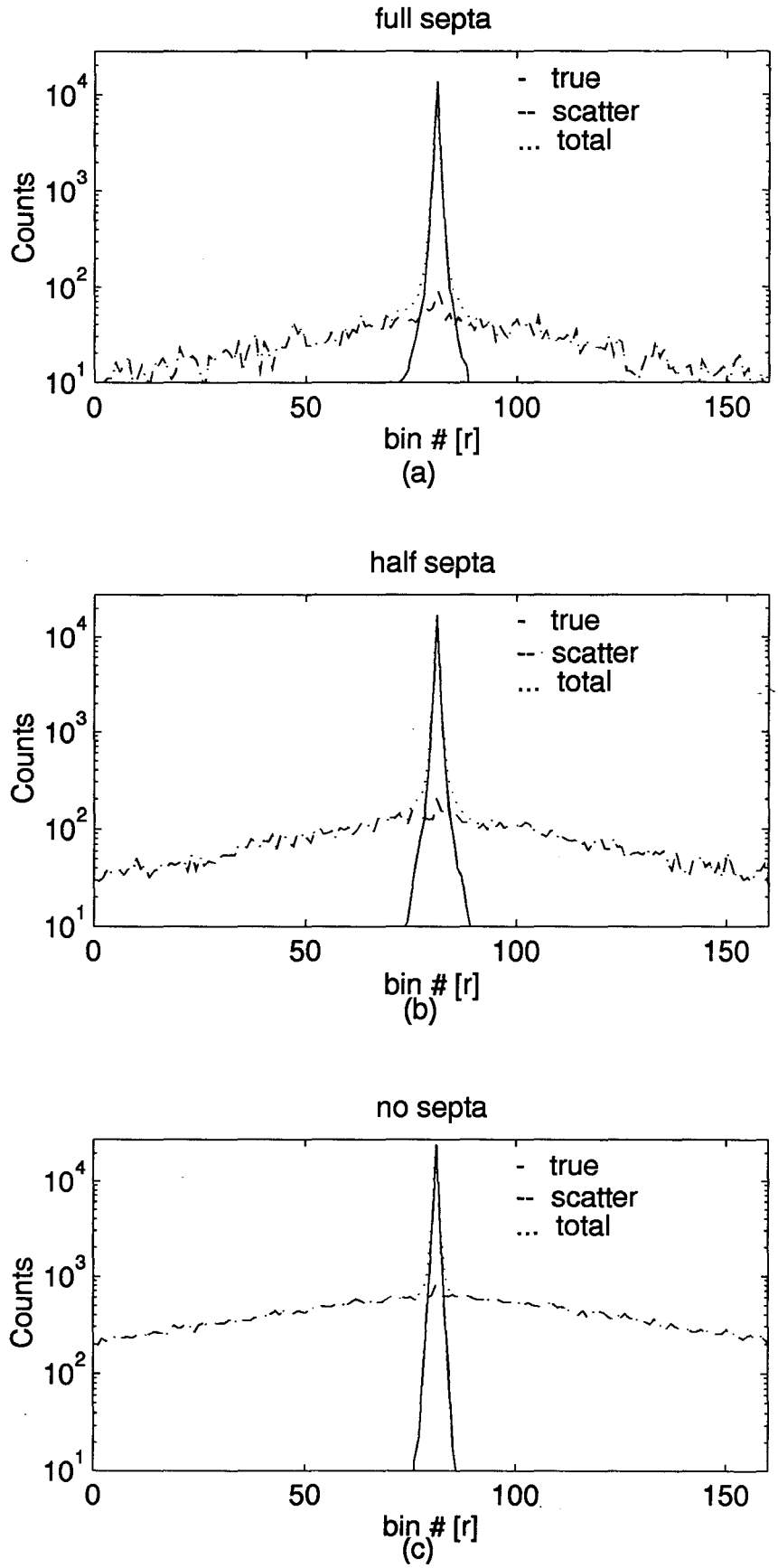

Figure 3.7 Sinogram projections for a line phantom acquired using different septa lengths, with summation over all 192 projection angles (a) full septa (b) 1/2 septa (c) no septa

Experimentally, only the total counts are available and the scatter component must be extrapolated from the broad tail. In addition, a blurring of the edges of the uniform phantom is observed and there is a broadening of the peak of the line source.

Resolution Peak Broadening

Figure 3.8 is derived from the centered line source simulation. The sharp peak is commonly referred to as the resolution peak and is a measure of the tomographs spatial resolution. The figure indicates that though the sensitivity of the tomograph will increase as the septa length decreases, there is no apparent degradation of resolution with a decreased septa length.

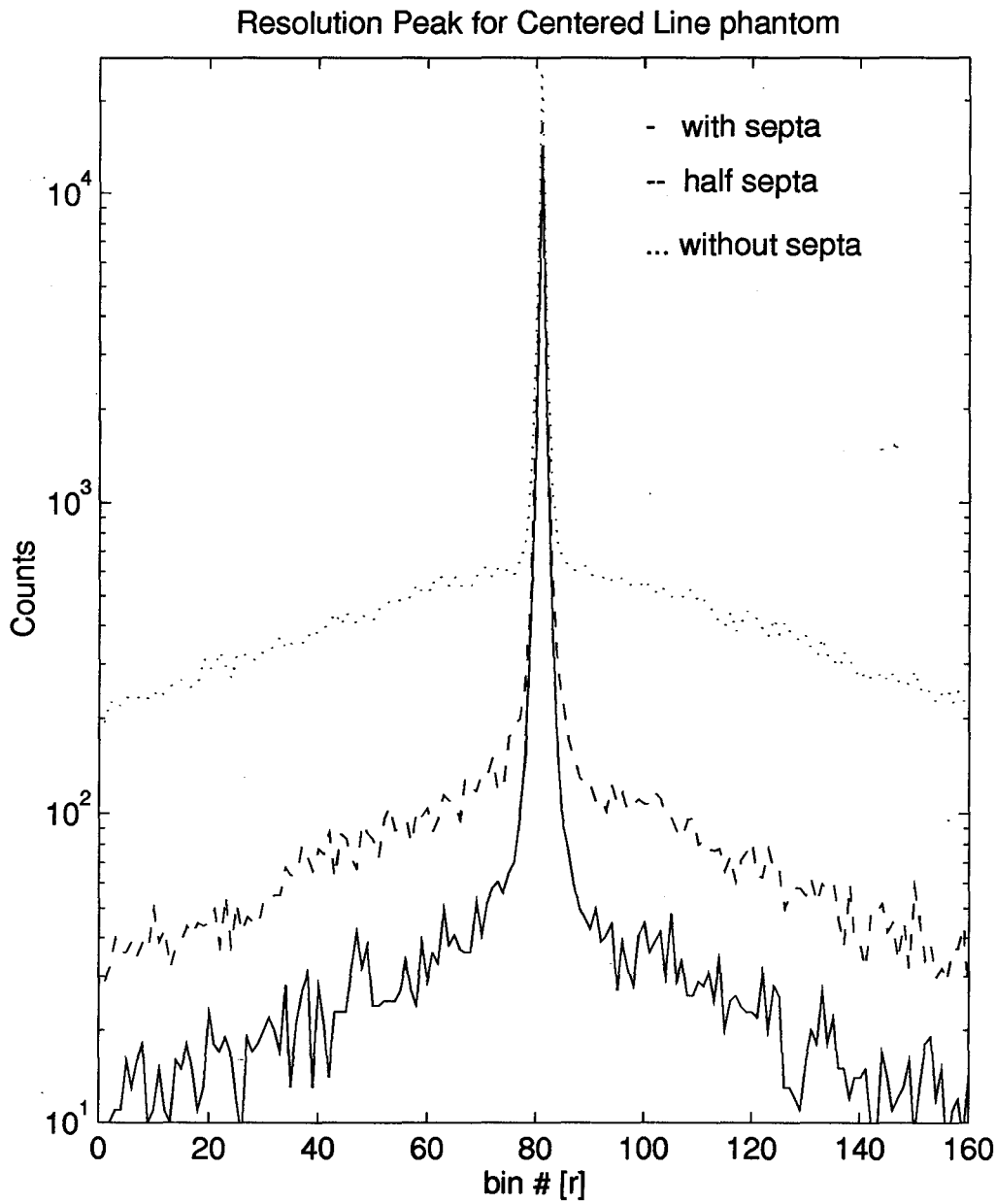

Figure 3.8 Resolution peak broadening measured from the line phantom simulation. The is no apparent degradation of resolution.

Noise Equivalent Count (NEC) Rate Analysis

For any imaging situation, the sensitivity parameters derived from signal to noise (SNR) considerations should be made with respect to the reconstructed image SNR. In this regard, sensitivity parameters can be derived from Noise Equivalent Count (NEC) Rate curves (Strother *et al* 1990). NEC Rate analysis has been shown to demonstrate the useful dynamic range of a PET system (Stother *et al* 1990, Bailey *et al* 1991). The NEC is defined as:

$$NEC = \frac{T^2}{T+S+2R} = \frac{T}{1+S/T+2R/T} \tag{3.2}$$

where T is the true coincident rate, S the scattered rate and R is the randoms count. The NEC incorporates the effect of noise and can be regarded as the "reduced" trues rate. In practice, a delayed window subtraction technique is often used to remove randoms. The factor of 2 in the denominator accounts for the use of the delayed window subtraction technique since randoms are counted both in the acquisition and delayed window, thereby increasing the noise in the measurement. The NEC takes into account all noise sources i.e. scatter and random coincidences.

In order to estimate the true, scatter and randoms rates at different activity concentrations from a time independent simulation it is necessary to assume that the

true and scattered count rates can be estimated by scoring these counts within a specific time interval or acquisition period. The activity (rate) is then simply the total number of counts (which remains constant for any given simulation) divided by the acquisition time (which is a variable).

The randoms rate is estimated from the total singles count rates in the detector rings and is given in Chapter I, by equation 1.18. However, in practice, not all the detectors in the ring are in coincidence with each other and those that are in coincidence are specified by a particular fan angle. In order to account for a specific FOV (fan angle), equation 1.18 must be modified as follows (Lupton and Keller 1983):

$$R = \frac{N_1 N_2 \tau_c \theta}{\pi \rho^2} \tag{3.3}$$

where N_1 and N_2 are the single event rates in the individual detector rings, τ_c is the timing coincidence window, θ the fan angle and ρ is the packing fraction of the detectors (which is assumed to be 1).

Hence, if ι is the time index in which all coincidence events are scored, the following rates are observed:

$$\textit{trues rate} = T/\iota$$
$$\textit{scatter rate} = S/\iota$$
$$\textit{randoms rate} = R/\iota^2$$

Using the above conventions, the NEC rate can be easily calculated for every septa configuration where the number of true, scattered and singles are given by the Monte Carlo simulation. If the above definitions are substituted into the formula for the NEC, equation 3.2 takes the following form:

$$NEC = \frac{T}{i(1+S/T) + 2R/T} \tag{3.4}$$

Taking the limit as $\iota \rightarrow 0$, i.e. the activity concentration tends towards infinity, the NEC rate approaches an asymptotic limit given by:

$$NEC_{LIM} = \frac{T^2}{2R} \tag{3.5}$$

Rate Curves

Figure 3.9a - 3.9d shows rate curves for a uniform and line phantom (each 20 cm in length) with septa fully extended and retracted. In all cases, both the trues and scattered count rates vary linearly with activity and the randoms count rate varies as the square of the activity. This trend is consistent with experimental results and other Monte Carlo simulations (Lupton and Keller 1983, Thompson *et al* 1992).

Experimental results at high activity are significantly skewed due to system dead time effects which generally exhibit a paralyzable behaviour (Thompson and Meyer 1987, Thompson *et al* 1992). The dead time losses are primarily due to the dramatic increase in the singles at high activity. The results reported in this work assume dead time corrected values.

NEC Rate Curves

Using the data from the Monte Carlo simulation, NEC rates were calculated, for the uniform phantom, over the activity range of interest, for each septa configuration. Figures 3.10a and b show the NEC rate plotted against activity for traditional 2D and 3D acquisition. The activity scale of 0 - 200 μCi/cc was chosen to

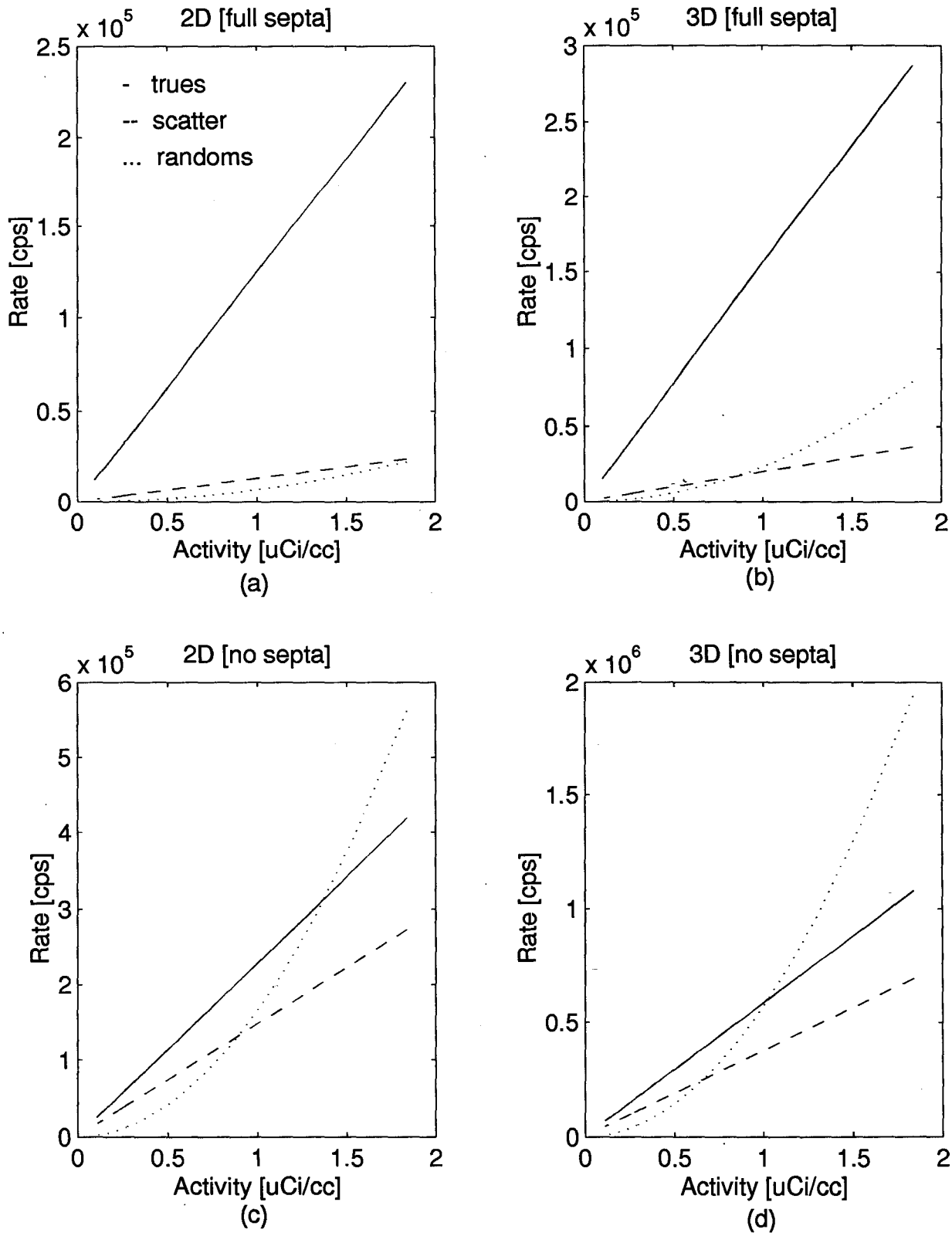

Figure 3.9 Rate curves for true, scattered and random events for a uniform phantom (a) 2D with full septa (b) 3D with full septa (c) 2D without septa (d) 3D without septa.

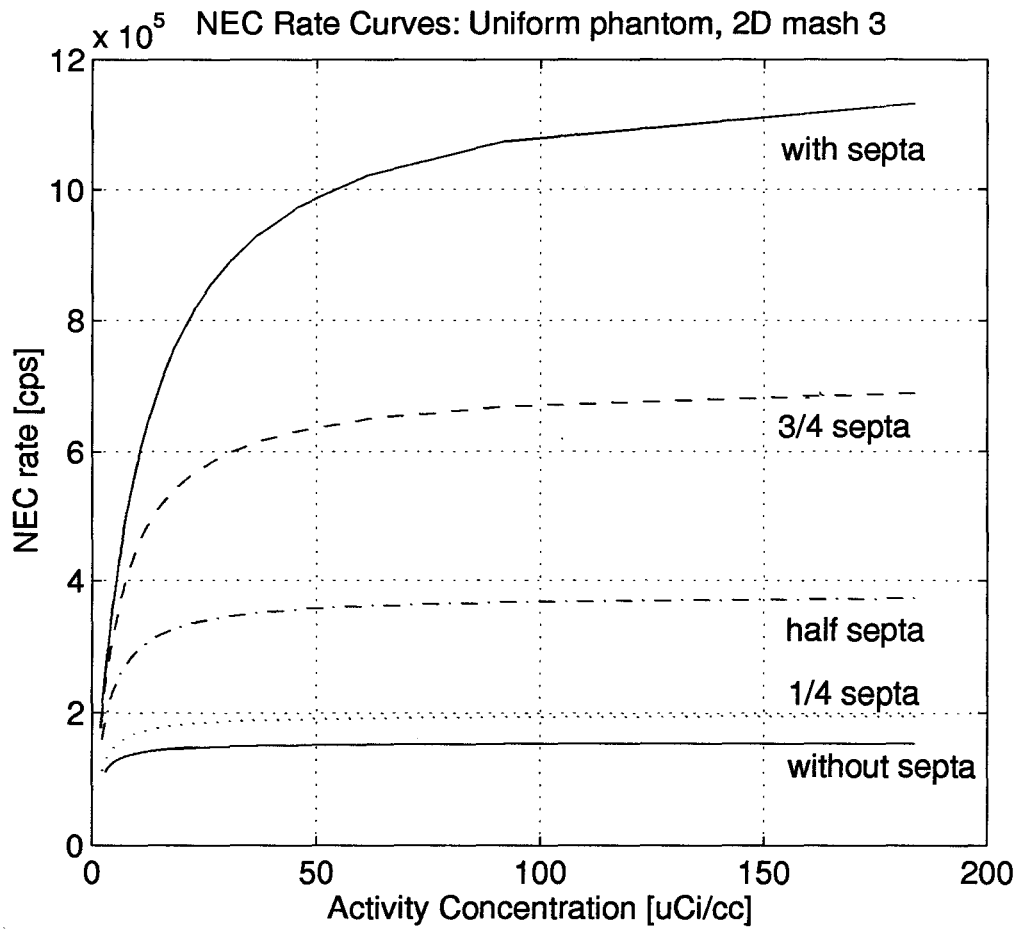

Figure 3.10a NEC rate for uniform phantom using traditional 2D, mash 3 acquisition, demonstrating the asymptotic NEC rate behaviour.

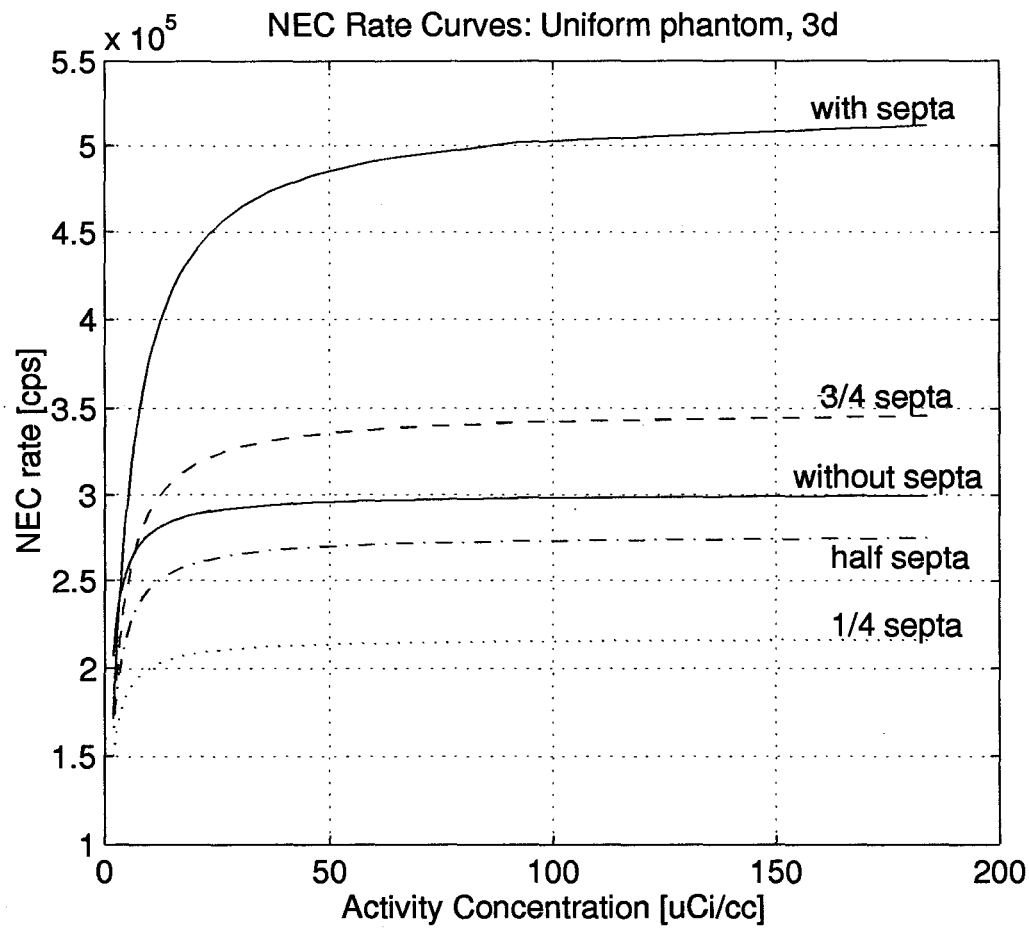

Figure 3.10b NEC rate for uniform phantom using traditional 3D acquisition, demonstrating the asymptotic NEC rate behaviour.

demonstrate the asymptotic behaviour of the NEC rate as predicted by equation 3.5. At very high activity concentrations, the NEC rate plateaus and there is no further gain, hence, the use of high activity concentrations will not result in better images. In addition, dead time effects will dominate in this region, resulting in a paralyzed system. Note, that the NEC_{LIM} rate is diminished by a factor of 3 between the normal 2D acquisition with full septa and 3D acquisition without septa.

However, the clinical range of interest for imaging is an activity concentration less than 2 μCi/cc. Figures 3.10c and d show the behaviour of the NEC rate in this region.

It is of interest to compare the NEC rate for 2D and 3D acquisition, with different septa configurations and with different mashing orders. Hence, a series of graphs were constructed that compared 2D NEC rates (with a specified mashing order), with 3D NEC rates for a particular septa length. The activity range of interest is 0 - 2 μCi/cc. All the graphs can be found in Appendix B. Plots of particular interest have been included in this section.

Figure 3.11 compares 3D [no septa] and 2D [mash 3]. It is obvious that below 2 μCi/cc, that 3D acquisition is always better than 2D acquisition, at any septa length. Despite the increase of random coincidences when operating in 3D mode, the gain in sensitivity will result in a better NEC rate i.e. a better SNR. Hence, it would be advantageous to acquire in 3D and then use single or multi-slice rebinning before reconstruction of the images (for tomographic imaging). In addition, below 1 μCi/cc,

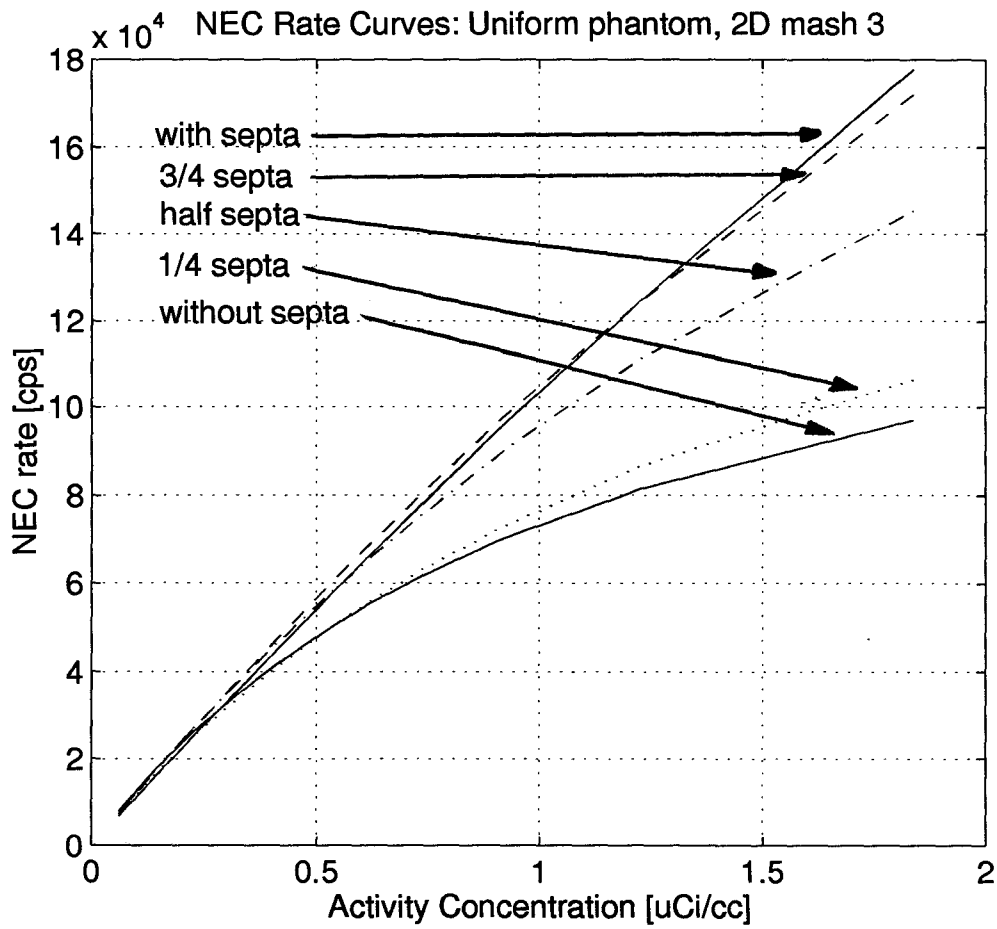

Figure 3.10c NEC rate for uniform phantom using traditional 2D, mash 3 acquisition, for a clinical activity range of 0 - 2 μCi/cc. Acquisition with full septa yields the highest NEC rate.

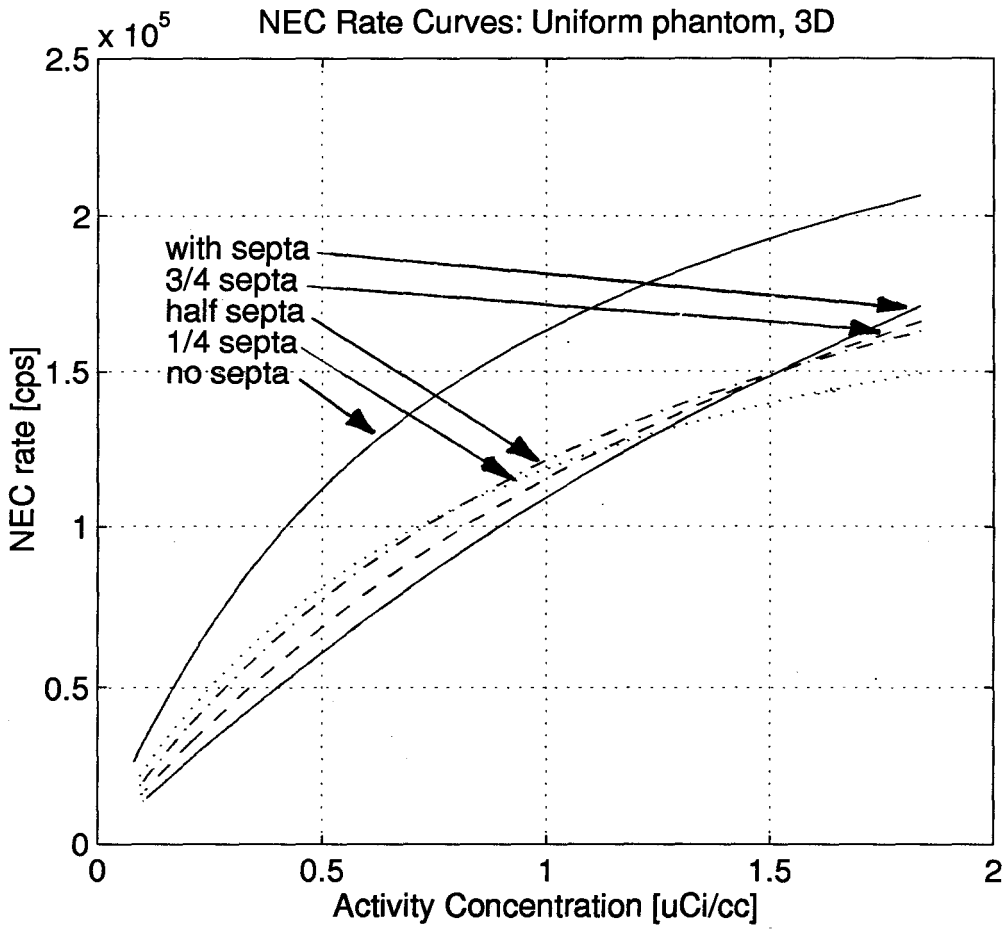

Figure 3.10d NEC rate for uniform phantom using traditional 3D acquisition, for a clinical activity range of 0 - 2 μCi/cc. Acquisition without septa yields the highest NEC rate.

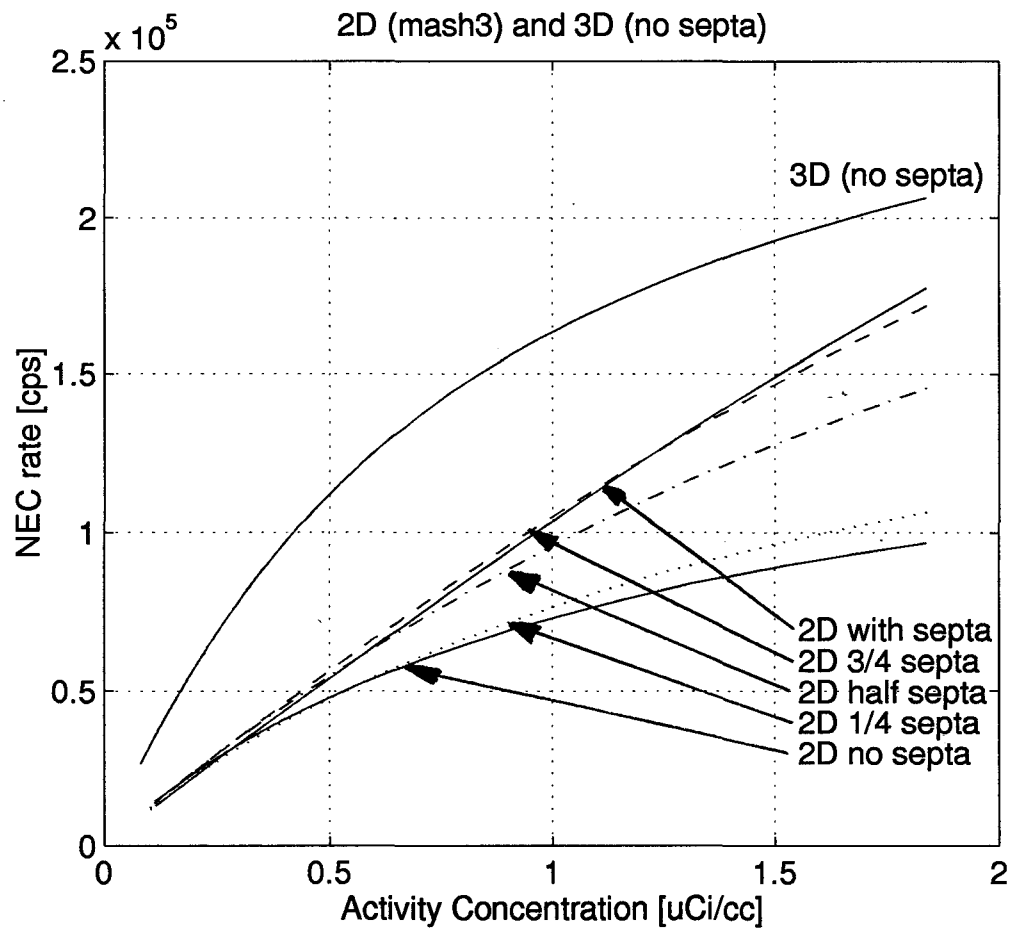

Figure 3.11 NEC rate comparison between 2D and 3D acquisition, for uniform phantom and a clinical activity range of 0 - 2 μCi/cc. 3D acquisition without septa always yields the highest NEC rate.

acquiring in 2D with septa is always better than or equivalent to any other septa configuration. As the mashing order of the 2D acquisition increases, a better NEC rate performance results, however, 3D [no septa] always outperforms any 2D acquisition (see Appendix B).

It is also possible to acquire in 3D with other septa configurations, however this results in a degraded performance with respect to 3D [no septa]. Table 4 summarizes the results of the graphs in Appendix B. The NEC rate is given for a number of activity concentrations for the various septa and mashing combinations.

TABLE 4

NEC Rate for Septa and Mashing Combinations

NEC Rate [x10^5 cps]

	Activity [uCi/cc]	0.25	0.5	0.75	1.0	1.25	1.5	1.75	2.0
FULL SEPTA									
	2D M1	0.1619	0.3170	0.4657	0.6084	0.7454	0.8770	1.0037	1.1256
	M3	0.2773	0.5420	0.7951	1.0371	1.2689	1.4911	1.7043	1.9090
	M5	0.3189	0.6207	0.9069	1.1785	1.4367	1.6825	1.9167	2.1401
	M7	**0.3323**	**0.6440**	**0.9370**	**1.2130**	**1.4734**	**1.7194**	**1.9522**	**2.1729**
	3D	0.3249	0.6118	0.8669	1.0953	1.3010	1.4871	1.6564	1.8110
3/4 SEPTA									
	2D M1	0.1625	0.3122	0.4506	0.5790	0.6983	0.8096	0.9136	1.0110
	M3	0.2955	0.5674	0.8184	1.0510	1.2670	1.4681	1.6559	1.8315
	M5	0.3617	0.6917	0.9940	1.2718	1.5281	1.7652	1.9853	2.1901
	M7	**0.3903**	**0.7427**	**1.0625**	**1.3540**	**1.6208**	**1.8660**	**2.0920**	**2.3011**
	3D	0.3836	0.6913	0.9438	1.1545	1.3331	1.4865	1.6195	1.7360
1/2 SEPTA									
	2D M1	0.1552	0.2870	0.4002	0.4987	0.5850	0.6614	0.7293	0.7903
	M3	0.2962	0.5494	0.7684	0.9597	1.1282	1.2778	1.4115	1.5317
	M5	0.3847	0.7117	0.9931	1.2377	1.4524	1.6423	1.8115	1.9632
	M7	0.4352	**0.8025**	**1.1167**	**1.3884**	**1.6258**	**1.8349**	**2.0206**	**2.1865**
	3D	**0.4508**	0.7754	1.0204	1.2119	1.3656	1.4917	1.5971	1.6865
1/4 SEPTA									
	2D M1	0.1310	0.2278	0.3020	0.3610	0.4088	0.4484	0.4817	0.5102
	M3	0.2715	0.4773	0.6386	0.7685	0.8754	0.9648	1.0407	1.1060
	M5	0.3718	0.6542	0.8759	1.0546	1.2017	1.3249	1.4296	1.5197
	M7	0.4464	0.7852	**1.0512**	**1.2655**	**1.4419**	**1.5896**	**1.7151**	**1.8230**
	3D	**0.5011**	**0.8143**	1.0285	1.1843	1.3027	1.3958	1.4708	1.5326
NO SEPTA									
	2D M1	0.1239	0.2059	0.2641	0.3076	0.3414	0.3683	0.3903	0.4086
	M3	0.2833	0.4799	0.6243	0.7349	0.8223	0.8931	0.9517	1.0009
	M5	0.4201	0.7162	0.9362	1.1060	1.2411	1.3510	1.4424	1.5194
	M7	0.5315	0.9089	1.1908	1.4094	1.5838	1.7262	1.8447	1.9448
	3D	**0.6898**	**1.1224**	**1.4192**	**1.6353**	**1.7998**	**1.9292**	**2.0335**	**2.1196**

The bold entries in Table 4 indicate the highest NEC rate for the septa and mashing combinations, at each activity listed. For example, in an acquisition using full

septa, operating in 2D mode and a mashing order of 7 will yield the highest NEC rate. From the table, it is observed that 2D acquisition with a mashing order of 7 will generally yield the highest NEC rate, for each septa configuration. However, this may not be the best overall configuration. The bold and underlined entries in Table 4 indicate the highest NEC rate for each activity, regardless of septa and mashing order. It is obvious that for clinical activity concentrations of less than 2 μCi/cc, that operating in 3D mode, without septa, will yield the best overall NEC rate performance.

There is one *caveat*. Though the best NEC rate performance is for an acquisition in 3D, without septa, and the overall sensitivity increase is by a factor of 7 (4.5 for trues), there is an accompanying increase of SF, from 10% to 40%. Hence, in order to realize the best NEC performance, one must be able to adequately correct for scatter, as well as for randoms. The use of the delayed window subtraction method for the correction of randoms has proven to be adequate, however, as mentioned previously, no preferred scatter correction method exists. DEWSC is a common technique, however, experimentally determined parameters are derived using simple phantoms, and cannot be applied in general. For neuro-imaging, in particular, DEWSC is sufficient. Hence, in this case, operating in traditional 3D mode will yield the best performance. Once acquired, the data can be reorganized into 2D projection data sets before image reconstruction or full 3D reconstruction can be used.

CONCLUSIONS

The optimization of septa length for both tomographic (2D) and volume (3D) acquisition must be made with respect to both count rate sensitivity and NEC rate performance. These figures of merit will indicate the trade off between the counting and imaging performance of the system, respectively.

The Monte Carlo technique has been used to study the performance of the ECAT 953/31 PET Scanner in the Department of Nuclear Medicine at McMaster University Medical Centre.

The choice of a specific septa length must be made with respect to the imaging conditions used. This directly implies that the activity concentration, distribution, half-life and hence, the acquisition time required will determine the optimum septa length. For example, in neuro-imaging, the scatter medium is fairly uniform and hence, adequate scatter correction is possible. However, cardiac imaging presents a large and highly heterogeneous absorption and scattering medium and attenuation and scatter correction techniques must be improved and validated.. To optimize the imaging performance of the system and improve our ability to determine changing spatial and temporal activity distributions. acquiring in 3D mode, without septa, will yield the best overall sensitivity and NEC rate performance

Future Work

In this work, the effect of septa shadowing with respect to septa length has been studied for 2D and 3D acquisition. The septa have been varied uniformly throughout the axis of the tomograph.

Originally, the geometry definition in the Monte Carlo code could be changed to vary the septa length uniformly across the tomographs axis and allow for a number of source distributions. The geometry definitions have been modified so that individual septa can be varied to any desired length so that the effect of varied septa length can be investigated in future studies, in both tomographic and PVI systems. A study of a variable length configuration can now be undertaken, within this framework, in order to determine if an increased efficiency and performance of the individual scan planes can be realized. In addition, the use of septa in PVI has previously been ignored. Septa, may also be beneficial in optimizing the NEC performance of the tomograph by increasing its sensitivity to true coincidences by removing a portion of the randoms and scatter.

APPENDIX A

Running the Monte Carlo Package

A full simulation is performed in three stages. The first stage involves the geometry and material definition. The second stage involves the generation of the data and the final stage requires the analysis of this data. Each stage has a particular software program that must be executed.

The *Geant* Monte Carlo package has its own unique "programming" or macro language known as KUMAC, and therefore requires the proper utility programs and environment. A FORTRAN program is used as a "driver" program for the KUMAC routines.

Geometry and Material Definition

Using the KUMAC protocol, the individual components of the system e.g. crystals, blocks, gantry etc. are defined. The driver program that is executed in order to assemble the components and generate the geometry file is called GCPI953.F. The geometry file generated is named CTI953.GEO. This file will be called by the *Geant* Monte Carlo code during the simulation.

Generating Monte Carlo Data

Once the geometry file is compiled, data can be generated using the GCPBS_953.F program. In addition to the geometry file, a user input file is also required. This file contains user specific data e.g. number of events, stratification angle. This file is called the GCPBS_INP.DAT file. Given these two data files, Monte Carlo data is generated by tracking the photons through the geometry and material using the *Geant* code. An output data file containing the energy of the photons through each step, and their interaction history is generated. This file is called by the analysis programs to extract the relevant data.

Analysis Program

The analysis code, DUAL_WINDOW2.F, requires only the output data file from the Monte Carlo code. In this program, the acquisition is simulated by using energy windows, coincidence logic, identification of LOR's etc.. and the output files contain data regarding energy spectra, sinograms and scatter fraction calculations. The files are in ASCII format and can then be post-processed.

The ASCII data files are then used in conjunction with MATLAB™ to construct the graphs and figures found in this work.

Functional Description of *Geant* routines and Driver Programs

I. Definitions and Initializations

UGINIT

- initializes GEANT.
- defines USER particular materials and description (such as aluminum, lead, air, BGO, vacum, water etc.)

UGEOM

- define USER geometry setup.
- define USER tracking media paramters.

GUKINE

- generate kinematics for primary track.

  pick random seed for first event in phantoms:

  point source or (x,y)
  needle source or (x,y)
  uniform disk
  brain phantom
  transmission source

II. Tracking and History of Each Event

GUTREV

- routine to control the tracking of one event

GUSTEP

- routine called at the end of each tracking step i.e. has track reached a volume boundry, has track stopped?

GUOUT

- USER routine called at the end of each event

  determines block and crystal multiplicities
  read all detectors
  read Compton switch

UGLAST

- termination routine

DUMPB

- routine to write results to the output, "DUMP" file.

III. Analysis of Data

- sinogram construction and line spread function.
- detector number for LOR package.
- check hardware block table.
- energy spectra.
- 256 axial LOR's.
- *2D coicidence detection.*
- *match detector numbers.*
- *3D coincidence detection.*
- *create detector and block energy spectra for trues and scatter.*
- *scatter analysis.*
- *singles for a slice, for 3D and for different mashings.*

The routines modified especially for this work, and for future studies, are the italicized entries under section III. The program is now able to accurately perform 3D coicidence detection and separate the components contributing to the scatter fraction. In addition, given the singles counts for each slice or LOR, the randoms rate for 2D, with different mashing orders, and 3D can be performed. This will allow the calaculation of NEC rates for numerous configurations of the scanner. The output data is stored in sinogram format allowing easy post-processing and graphical display.

APPENDIX B

Effects of varying septa length on NEC for 2D acquisition (mash 1,3, 5, 7) and 3D acquisition.

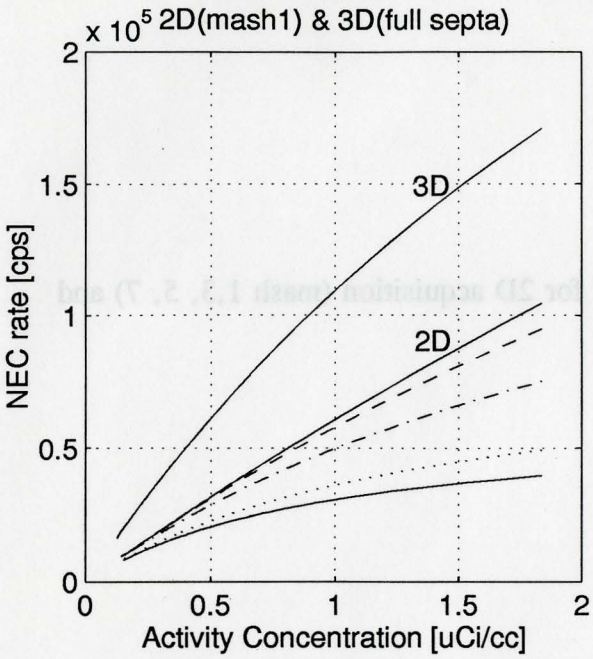
x 10^5 2D(mash1) & 3D(full septa)
NEC rate [cps]
Activity Concentration [uCi/cc]
3D
2D
0
0.5
1
1.5
2

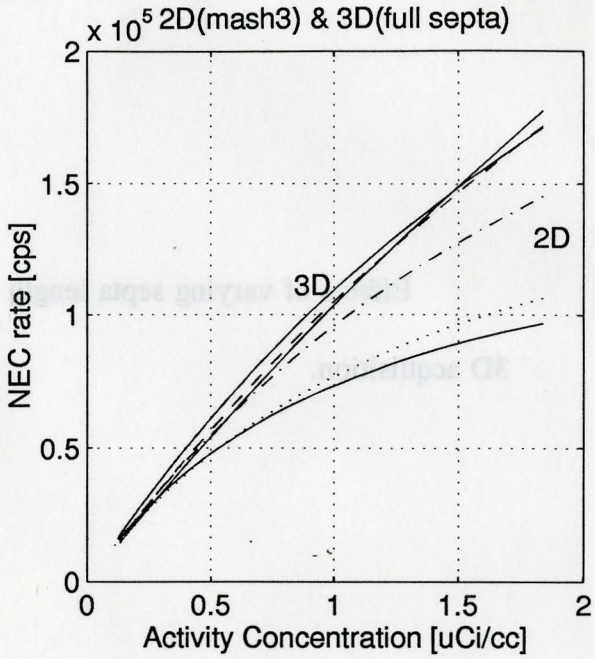
x 10^5 2D(mash3) & 3D(full septa)
NEC rate [cps]
Activity Concentration [uCi/cc]
3D
2D
0
0.5
1
1.5
2

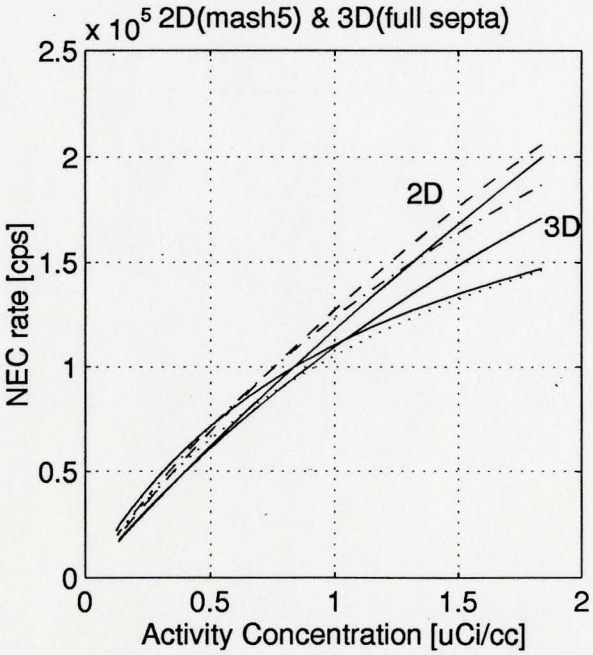
x 10^5 2D(mash5) & 3D(full septa)
NEC rate [cps]
Activity Concentration [uCi/cc]
2D
3D
0
0.5
1
1.5
2
2.5

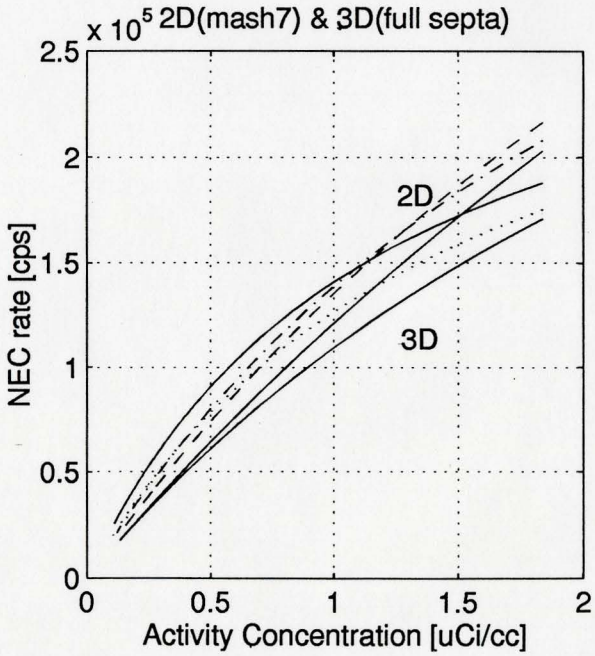
x 10^5 2D(mash7) & 3D(full septa)
NEC rate [cps]
Activity Concentration [uCi/cc]
2D
3D
0
0.5
1
1.5
2
2.5

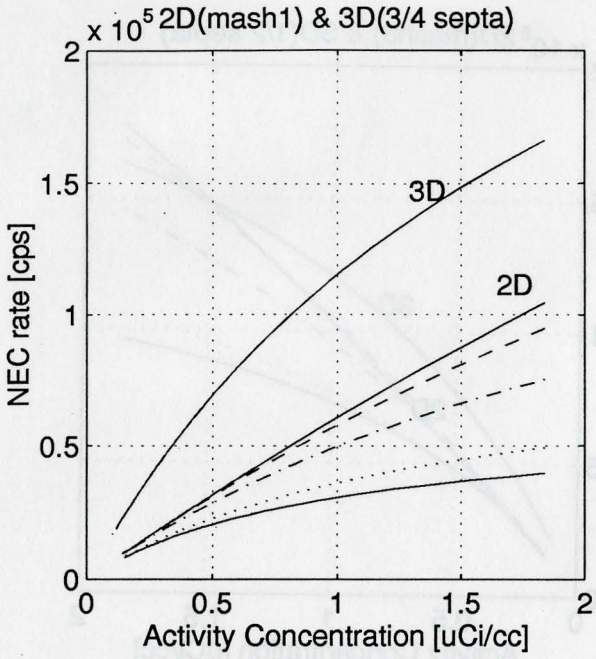
x 10^5 2D(mash1) & 3D(3/4 septa)
NEC rate [cps]
Activity Concentration [uCi/cc]
3D
2D
0
0.5
1
1.5
2

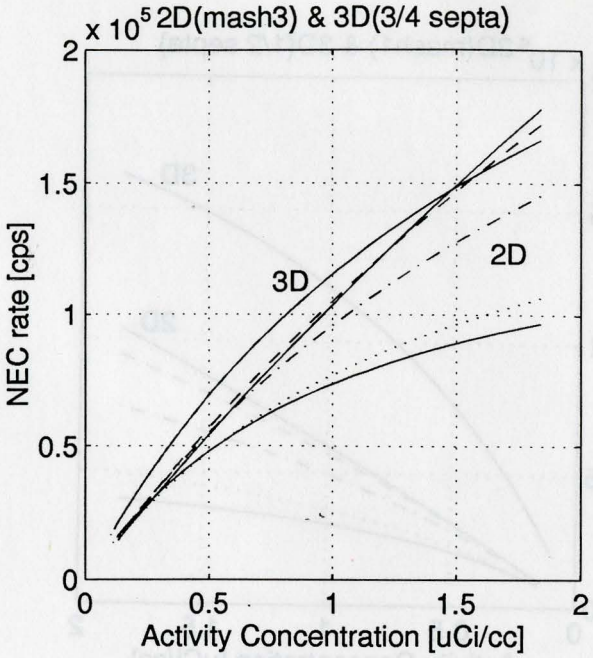
x 10^5 2D(mash3) & 3D(3/4 septa)
NEC rate [cps]
Activity Concentration [uCi/cc]
3D
2D
0
0.5
1
1.5
2

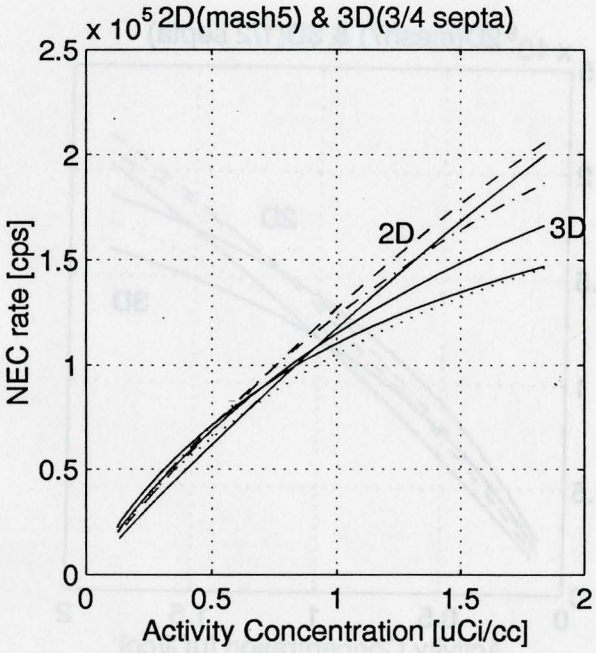
x 10^5 2D(mash5) & 3D(3/4 septa)
NEC rate [cps]
Activity Concentration [uCi/cc]
2D
3D
0
0.5
1
1.5
2
2.5

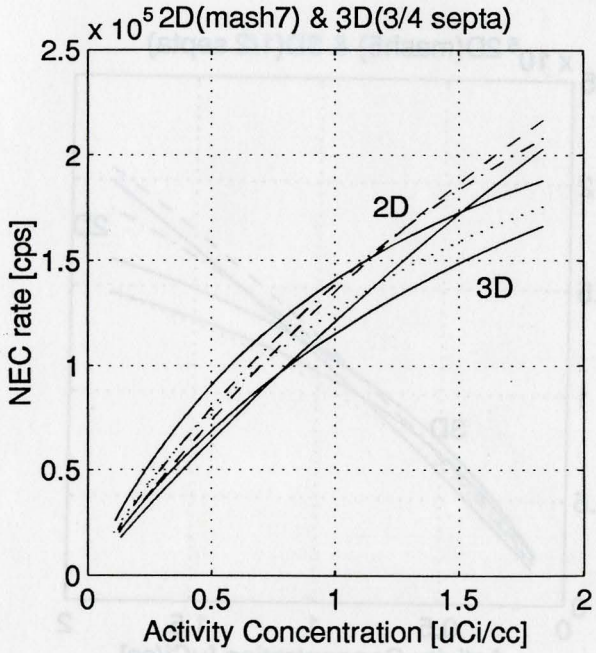
x 10^5 2D(mash7) & 3D(3/4 septa)
NEC rate [cps]
Activity Concentration [uCi/cc]
2D
3D
0
0.5
1
1.5
2
2.5

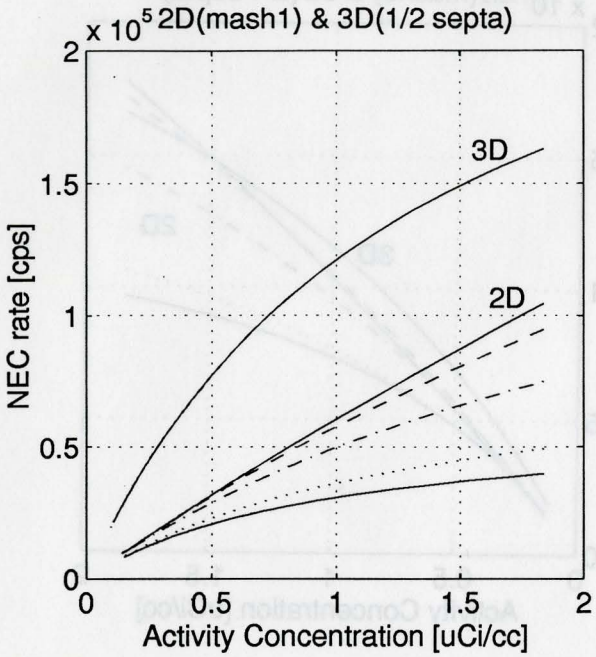
x 10^5 2D(mash1) & 3D(1/2 septa)
NEC rate [cps]
Activity Concentration [uCi/cc]
3D
2D
0
0.5
1
1.5
2

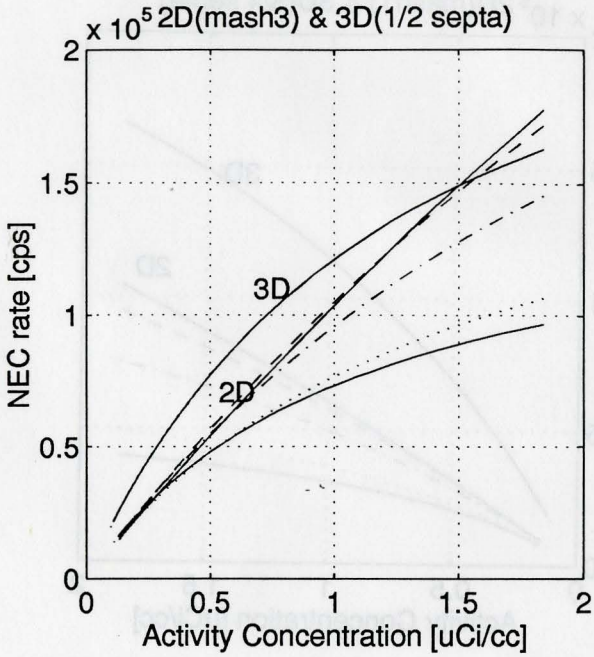
x 10^5 2D(mash3) & 3D(1/2 septa)
NEC rate [cps]
Activity Concentration [uCi/cc]
3D
2D
0
0.5
1
1.5
2

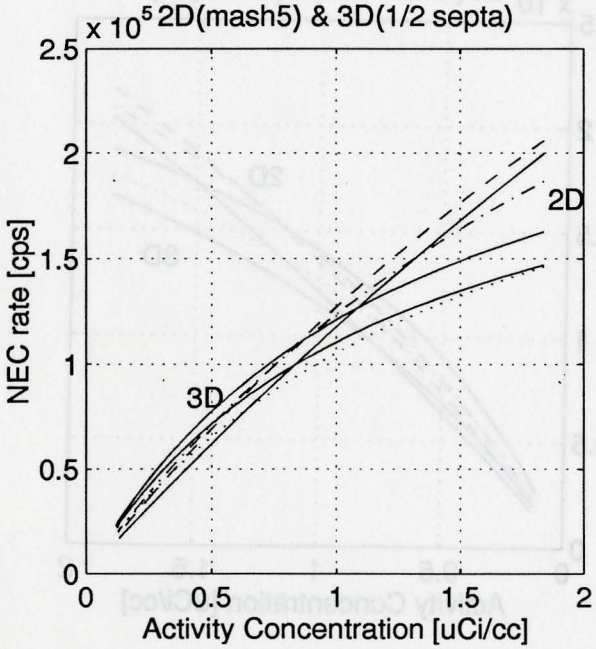
x 10^5 2D(mash5) & 3D(1/2 septa)
NEC rate [cps]
Activity Concentration [uCi/cc]
2D
3D
0
0.5
1
1.5
2
2.5

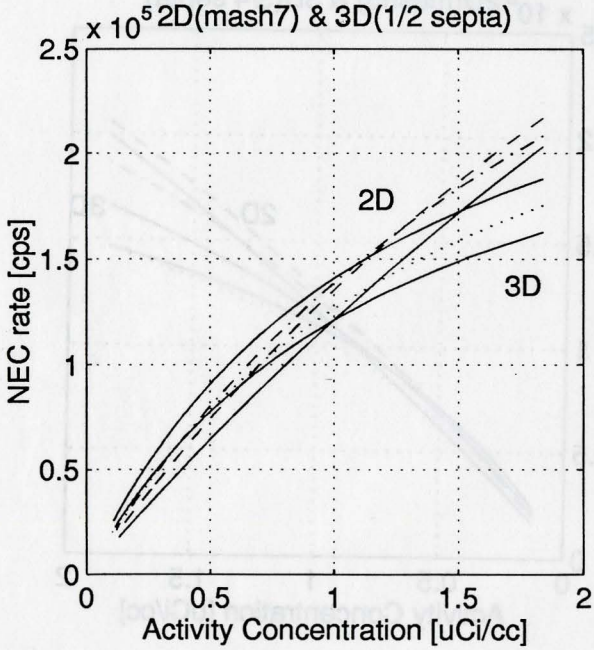
x 10^5 2D(mash7) & 3D(1/2 septa)
NEC rate [cps]
Activity Concentration [uCi/cc]
2D
3D
0
0.5
1
1.5
2
2.5

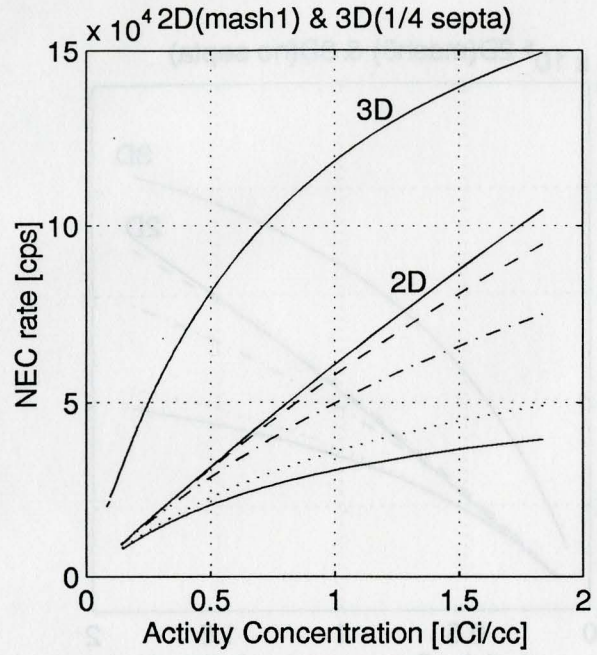
x 10^4 2D(mash1) & 3D(1/4 septa)
NEC rate [cps]
Activity Concentration [uCi/cc]
3D
2D
0
5
10
15
0.5
1
1.5
2

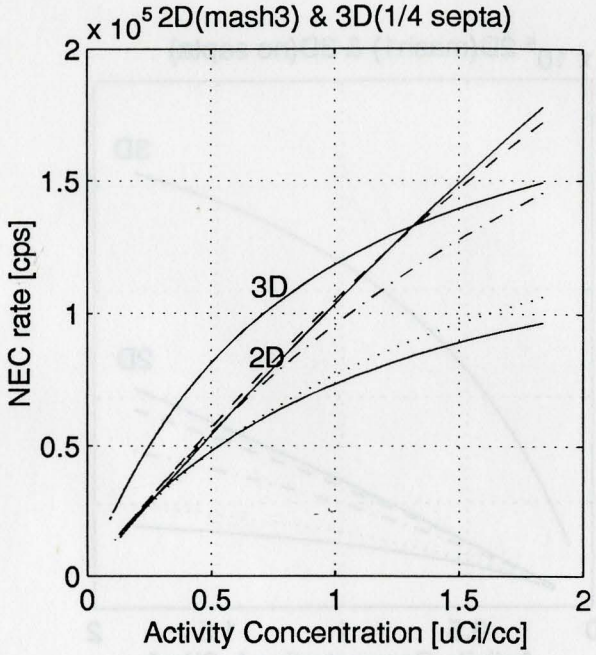
x 10^5 2D(mash3) & 3D(1/4 septa)
NEC rate [cps]
Activity Concentration [uCi/cc]
3D
2D
0
0.5
1
1.5
2

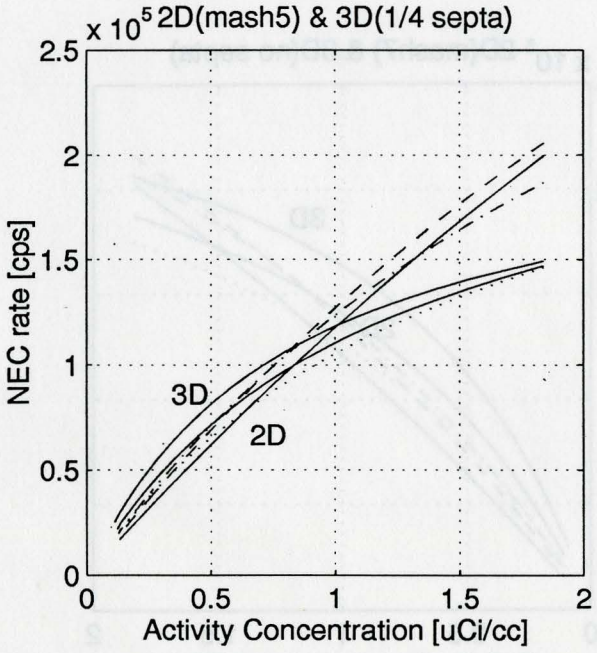
x 10^5 2D(mash5) & 3D(1/4 septa)
NEC rate [cps]
Activity Concentration [uCi/cc]
3D
2D
0
0.5
1
1.5
2
2.5

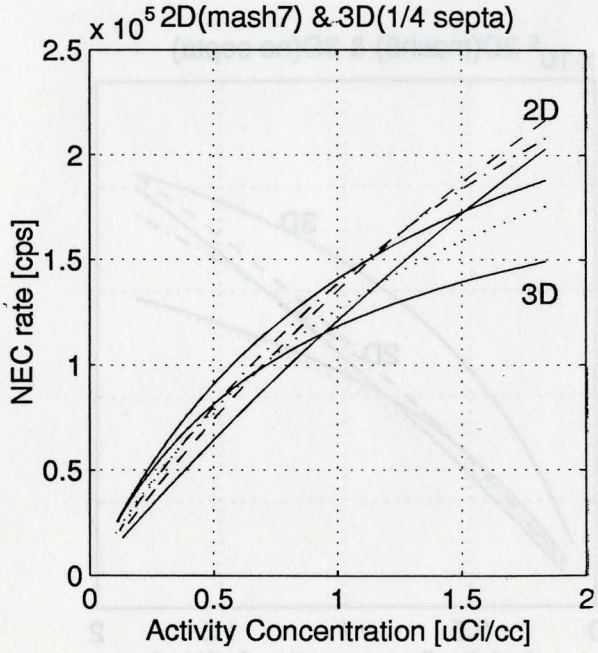
x 10^5 2D(mash7) & 3D(1/4 septa)
NEC rate [cps]
Activity Concentration [uCi/cc]
2D
3D
0
0.5
1
1.5
2
2.5

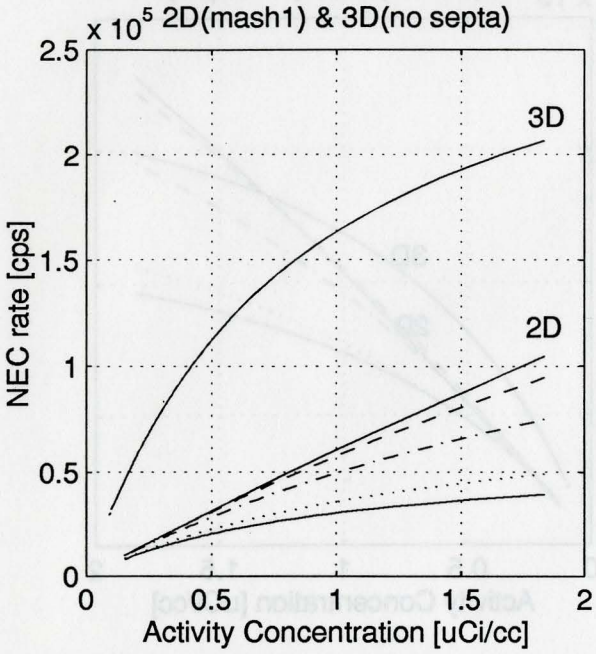
x 10^5 2D(mash1) & 3D(no septa)
NEC rate [cps]
Activity Concentration [uCi/cc]
3D
2D
0
0.5
1
1.5
2
2.5

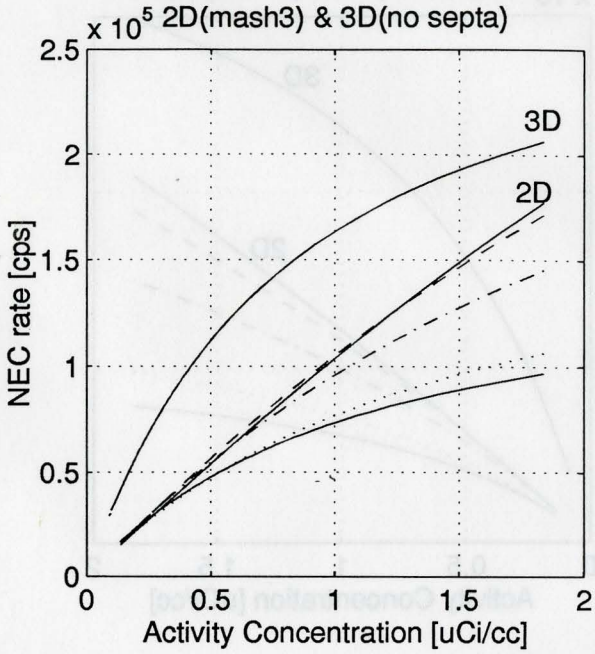
x 10^5 2D(mash3) & 3D(no septa)
NEC rate [cps]
Activity Concentration [uCi/cc]
3D
2D
0
0.5
1
1.5
2
2.5

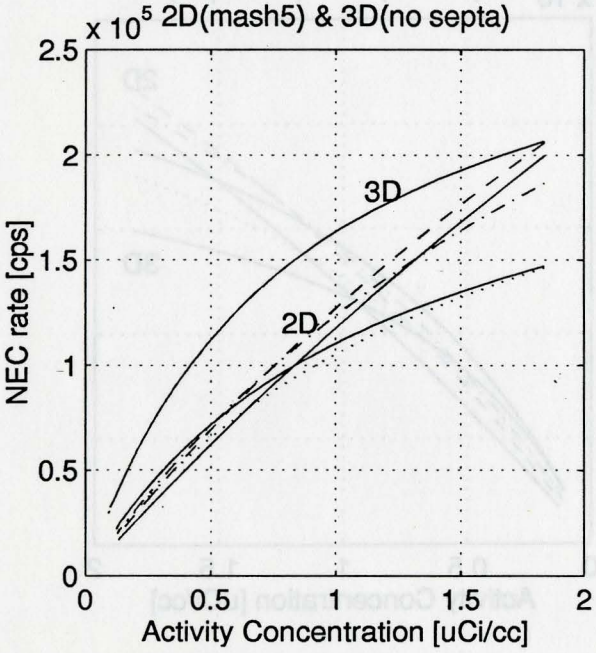
x 10^5 2D(mash5) & 3D(no septa)
NEC rate [cps]
Activity Concentration [uCi/cc]
3D
2D
0
0.5
1
1.5
2
2.5

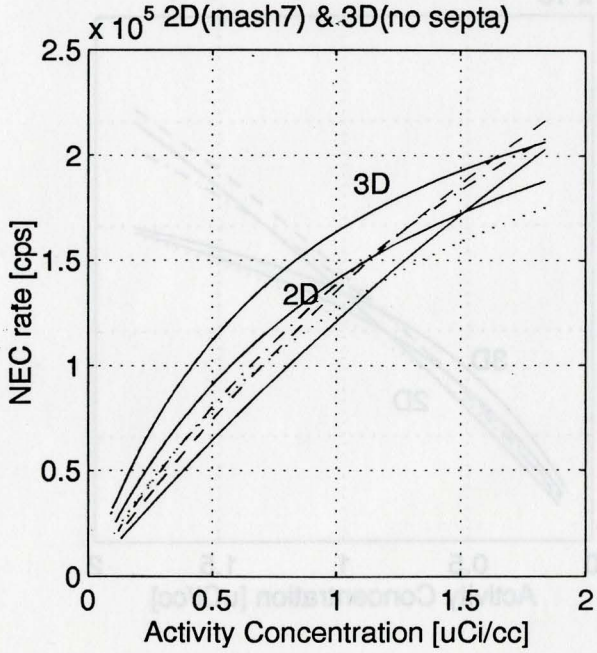
x 10^5 2D(mash7) & 3D(no septa)
NEC rate [cps]
Activity Concentration [uCi/cc]
3D
2D
0
0.5
1
1.5
2
2.5

REFERENCES

Andreo P (1991) Monte Carlo Techniques in Medical Radiation Physics. *Phys Med Biol* **36**: 861-920.

Bailey DL, Jones T, Spinks TJ, Gilardi MC, Townsend DW (1991) Noise Equivalent Count Measurements in a Neuro-PET Scanner with Retractable Septa. *IEEE Trans Nucl Sci* **10**: 256-260.

Barney JS, Harrop R, Dykstra CJ (1993) Source Distribution Dependent Scatter Correction for PVI. *IEEE Trans Nucl Sci* **40**: 1001-1007.

Barrett HH (1984) The Radon Transform and Its Application. In: *Progress in Optics XXI*. Amsterdam: Northholand Publishing.

Bendriem B, Trebossen R, Frouin V, Syrota A (1994) A PET Scatter Correction Using Simultaneous Acquisitions with Low and High Energy Thresholds. *IEEE Trans Med Imag* preprint 1-5.

Bergstrom M, Eriksson L, Bohm C, Blomqvist G, Litton J (1983) Correction for Scattered Radiation in a Ring Detector Positron Camera by Integral Transformation of the Projections. *J Compt Assist Tomogr* **7**: 42-50.

Bevington and Robinson (1992) *Data Reduction and Error Analysis for the Physical Sciences*. New York: McGraw-Hill.

Bowen C (1994) *Analytic 3D Scatter Correction in Positron Tomography Using the Klein-Nishina Equation*. McMaster University: M.Sc. Thesis.

Brooks RA, DiChiro G (1976) Principles of Computer Assisted Tomography (CAT) in Radiographic and Radioisotope Imaging. *Phys Med Biol* **21**: 689-732.

Brownell GL, Sweet WH (1953) Localization of Brain Tumors with Positron Emitters. *Nucleonics* **11**: 40-45

Casey ME (1992) *An Analysis of Counting Losses in Positron Emission Tomography*. University of Tennessee: Ph.D. Thesis.

Cherry S, Meikle SR, Hoffman EJ (1993) Correction and Characterization of Scattered Events in 3D PET Using Scanners with Retractable Septa. *J Nucl Med* **34**: 671-678.

Cormack AM (1980) Early Two-Dimensional Reconstruction and Recent Topics Stemming from It. *Science* **209:** 1482-1486.

Daube-Witherspoon ME, Muehllehner G (1987) Treatment of Axial Data in 3 Dimensional PET. *J Nucl Med* **28:** 1717-1724.

deKemp R (1992) *Attenuation Correction in Positron Emission Tomography using Single Photon Transmission Measurement.* McMaster University: M.Sc. Thesis.

Evans RD (1985) *The Atomic Nucleus.* Tampa: Krieger.

Geant User's Guide (1992). Geneva, Switzerland: CERN Laboratory.

Grootoonk S, Spinks T, Kennedy A, Bloofield P, Sashin D, Jones T (1993) The Practical Implementation and Accuracy of a Dual-Window Scatter Correction in a Neuro-PET Scanner with Septa Retracted. *ECAT Tech User's Meeting:* 31.

Herman GT (1979) *Image Reconstruction from Projections.* New York: Springer-Verlag.

Hornich H (1986) A Tribute to Johann Radon. *IEEE Trans nucl Sci* **MI-5:** 169-176.

Hounsfield GN (1973) Computerized transverse axial scanning (tomography): Part I. Description of system. *Brit J Rad* **46:** 1016-1022.

Johns HE, Cunningham JR (1983) *The Physics of Radiology.* Chicago: Thomas.

Jaszczak RJ, Greer KL, Floyd CE, Harris CC, Coleman RE (1984) Improved SPECT Quantification Using Compensation for Scattered Photons. *J Nucl Med* **25**: 893-900.

Knoll GF (1989) *Radiation Detection and Measurement.* New York: John Wiley & Sons.

Knuth DE (1969) Random Numbers *The Art of Computer Programming Vol 2. Seminumerical Algorithms* 2nd ed. Reading: Addison-Wesley

Krane KS (1988) *Introductory Nuclear Physics.* New York: John Wiley & sons.

Lecomte R (1992) Analytical Study of Performance in a 3-D PET Scanner. *Phys Med Biol* **37**: 623-634.

Leenders K, Gibbs JM, Frackowiak RSJ, Lammertsma AA, Jones T (1984) Positron Emission Tomography of the Brain: New Possibilites For The Investigation Of Human Cerebral Pathophysiology. In: *Movement Disorders*. Amsterdam. Rodopi.

Lewitt RM, Muehllehner G, Karp JS (1991) Image Reconstruction for PET by Multislice Rebinning and Axial Filtering. *Conference Record 1991. IEEE Trans Nucl Sci Symp and Med Imag Conf. Santa Fe, NM. IEEE Cat. No. CH#100S5* **3:** 2054-2059.

Lupton LR, Keller NA (1983) Performance Study of Single Slice Positron Emission Tomography Scanners by Monte Carlo Techniques. *IEEE Trans Med Imag* **2**: 54-168.

McKee BTA, Gurvey AT, Harvey PJ, Howse DC (1992) A Deconvolution Scatter Correction for a 3D PET System. *IEEE Trans Med Imag* **11**: 560-569.

Michel C, Bol A, Spinks T, Townsed D, Bailey D, Grootoonk S, Jones T (1991) Assessment of Response Function in Two PET Scanners with and without Interplane Septa. *IEEE Trans Med Imag* **10**: 240-248.

Morin RL (1988) *Monte Carlo Simulation in the Radiological Sciences.* Roca Boran: CRC Press.

Peebles PZ (1993) *Probability, Random Variables and Random Signal Processes 3rd ed.* New York: McGraw-Hill.

Shao L, Karp JS (1991) Cross-Plane Scattering Correction - Point Source Deconvolution in PET. *IEEE Trans Med Imag* **10**: 234-239.

Sorenson JA, Phelps ME (1980) *Physics in Nuclear Medicine.* Philadelphia: W.B. Saunders Company.

Stewart AT, Roellig LO (1967) *Positron Annihilation.* New York: Academic Press.

Strother SC, Casey ME, Hoffman EJ (1990) Measuring PET Scanner Sensitivity: Relating Countrates to Image Signal-to-Noise using Noise Equivalent Count. *IEEE Trans Nucl Sci* **37**: 783-788.

Sweet WH (1951) Uses of nuclear disintegrations in the diagnosis and treatment of brain tumors. *New Eng J Med* **245**: 875-878.

Thompson CJ (1993) The Problem of Scatter Correction in Positron Volume Imaging. *IEEE Trans Med Imag* **12**: 124-132.

Thompson CJ, Meyer E (1987) The Effect of Live Time on Components of a Positron Tomograph and Image Quantification. *IEEE Trans Nucl Sci* **34**: 337-343.

Thompson CJ, Moreno-Cantu J, Picard Y (1992) PETSIM: Monte Carlo Simulation of all Sensitivity and Resolution Parameters of Cylindrical Positron Imaging Systems. *Phys Med Biol* **37**: 731-749.

Tomitani T (1987) An Edge Detection Algorithm for Attenuation Correction in Emission CT. *IEEE Trans Nucl Sci* **34**: 309-315.

Townsend D, Defrise M (1993) Image Reconstruction Methods in Positron Tomography. *Academic Training Program of CERN 1992-1993* **CERN 93-02**.

Webb (1988) *The Physics of Medical Imaging*. Philadelphia: Hilger.

Yu SK, Nahmias C (1995) Single-photon transmission measurements in positron tomography using ^{137}Cs. *Phys Med Biol* **40**: 1255-1266.